Identifying dynamical boundaries and phase space transport using Lagrangian coherent Structures

Phanindra Tallapragada

Dissertation submitted to the Faculty of the
Virginia Polytechnic Institute and State University
in partial fulfillment of the requirements for the degree of

Doctor of Philosophy

in

Engineering Mechanics

Shane D. Ross, Chair
David G. Schmale
Mark Stremler
Mark Paul
Scott Hendricks

August 24, 2010
Blacksburg, Virginia

Identifying dynamical boundaries and phase space transport using Lagrangian coherent structures

Phanindra Tallapragada

Abstract

In many problems in dynamical systems one is interested in the identification of sets which have qualitatively different fates. The finite-time Lyapunov exponent (FTLE) method is a general and equation-free method that identifies codimension-one sets which have a locally high rate of stretching around which maximal exponential expansion of line elements occurs. These codimension-one sets thus act as transport barriers. This geometric framework of transport barriers is used to study various problems in phase space transport, specifically problems of separation in flows that can vary in scale from the micro to the geophysical.

The first problem which we study is of the nontrivial motion of inertial particles in a two-dimensional fluid flow. We use the method of FTLE to identify transport barriers that produce segregation of inertial particles by size. The second problem we study is the long range advective transport of plant pathogen spores in the atmosphere. We compute the FTLE field for isobaric atmospheric flow and identify atmospheric transport barriers (ATBs). We find that rapid temporal changes in the spore concentrations at a sampling point occur due to the passage of these ATBs across the sampling point.

We also investigate the theory behind the computation of the FTLE and devise a new method to compute the FTLE which does not rely on the tangent linearization. We do this using the 925 matrix of a probability density function. This method of computing the geometric quantities of stretching and FTLE also heuristically bridge the gap between the geometric and probabilistic methods of studying phase space transport. We show this with two examples.

Acknowledgments

I owe my deepest gratitude to my advisor Dr. Shane Ross, whose seminar on the Three-body problem in my first semester of graduate school led to my interest in dynamical systems. His constant encouragement to explore new ideas and commitment to research have been an inspiration for me. His patience with my errors have been crucial to my intellectual development. I would like to take this opportunity to thank him for all his support during my four years at Virginia Tech.

I would also like to thank Dr. David Schmale for giving me the opportunity to work on the interesting problem of punctuated changes in the atmosphere caused by the movement of transport barriers. His enthusiasm to combine dynamical systems with the spread of crop diseases is a motivation for me to explore new problems that are seemingly unrelated to dynamical systems. I would like to thank Dr. Mark Paul for providing me the opportunity to work on the problem of transport barriers Rayleigh-Bénard convection. His enthusiasm and encouragement both in and out of the class have helped me to explore many of the theoretical concepts used in this thesis. I would like to thank Dr. Mark Stremler for introducing me to the various interesting possibilities of cellular flows in my second semester. His collaborative work on the problem of transport in the lid-driven cavity flow has helped me to formulate some of the concepts used in this thesis. I would like to thank Dr. Scott Hendricks for his suggestions and questions that helped me to polish the thesis. I also wish to thank him for the guidance he gave me when I was a teaching assistant for him. I would like to thank Dr. Sunghwan Jung for being on the committee for the final exam and offering useful suggestions.

Contents

List of Figures

x

List of Tables

Chapter 1

Introduction

Nonlinear dynamical systems are ubiquitous in science, engineering and economics. But most of the relevant nonlinear ordinary differential equations (ODEs) do not possess exact analytical solutions. With the advent of computers, this problem has been partially overcome. Today one can easily numerically generate (approximate) solutions for many of the prototypical nonlinear ODEs using simple numerical integration packages such as those found in Matlab. However, despite the ease with which numerical solutions of nonlinear ODEs can be produced, one still faces tremendous difficulty in drawing general conclusions about the nature of solutions. This is especially true for aperiodic systems and high dimensional systems. One aspect of a system that we are particularly interested in is phase space transport. Understanding the structures that govern phase space transport has important general applications and specifically in mixing and separation problems in fluid flows that vary in scale from the micro to the geophysical, interplanetary transport and instability of mechanical systems, to name a few. The primary focus of this thesis is to identify special solutions and or sets in phase space that will provide an understanding of the (phase space) structure of the system.

One way of identifying underlying structure is to study the (local) expansion and contraction in phase space. This approach has a general appeal because it can be applied to

time-dependent systems while the method of invariant manifolds of fixed points is limited to time-independent systems. We apply the method of finite-time Lyapunov exponents (FTLE) and Lagrangian coherent structures (LCS), which is a systematic tool to identify codimension one hyperbolic sets that provide a framework of transport barriers that partition the phase space. In chapters 3 and 4 we review of the theory of FTLE and LCS and outline our new method of the partial FTLE, which we demonstrate with two examples, a forced damped pendulum and Rayleigh-Bénard convection. In chapter 5 we apply the method of partial FTLE and LCS to create a framework for separating neutrally buoyant particles in a two dimensional Stokes flow. This problem also acts as a test bed for the general problem of identifying transport barriers that are related to interesting physical phenomena. In chapters 6 - 8 we apply the method of LCS to the much more challenging problem of identifying atmospheric transport barriers (ATBs). Our motivation to study ATBs is to explain the rapid temporal changes, hereafter referred to as punctuated changes, in the concentration of atmospheric *Fusarium* spores. *Fusarium* is one of the most important genera of fungi on the planet. Some species of *Fusarium* are important pathogens of plants and animals. We show that punctuated changes in the spore concentrations are to a high degree of probability caused due to the movement of atmospheric LCS.

The method of FTLE and LCS which relies on local expansion and contraction in phase space can identify repelling and attracting codimension one sets, but it does not necessarily partition the phase space into sets between which transport is minimum. In the last decade there has been substantial interest and work in applying probabilistic methods drawn from ergodic theory that can identify the so-called almost-invariant sets. As opposed to the method of FTLE and LCS, the almost-invariant set (AIS) approach does not rely on long time computations of trajectories. However the AIS approach is limited to time independent or periodic systems. The relationship between the two approaches has not been well understood so far for general time-dependent systems. Chapter 9 reviews the theory of almost invariant sets. We then take two examples of two dimensional time-periodic flows, the double-gyre flow and the lid driven wide cavity flow, to compute and compare the

almost invariant sets with the transport barriers identified by LCS. Based on these examples we make a connection between the geometric and probabilistic approaches by identifying stretching with the second moment of a probability density function. Using this we devise a new method to compute the FTLE that does not rely on a linearized flow, which is a drawback with the standard method of computing FTLE. We then apply this method to the atmospheric flow to identify coherent sets, the time-dependent analogues of AIS.

Our specific contributions to the literature are

- We give a definition of the partial FTLE, its relation to the FTLE, its uses and limitations, in chapter 4.

- We apply the method of partial FTLE and LCS to identify transport barriers in phase space that cause the segregation of neutrally buoyant particles in a two-dimensional fluid flow, in chapter 5.

- We compute the FTLE for isobaric flows in the lower atmosphere and identified the ATBs in chapter 8. We use these transport barriers to identify a statistically significant sensitivity of the punctuated changes in the concentration of *Fusarium* to the movement of ATBs.

- We devise a new set-based definition for the FTLE and applied it to find transport barriers and coherent sets in the atmospheric flow, in chapter 9. Through numerical examples we showed that this approach is also a bridge between the geometric and probabilistic methods for phase space transport in chapter 9.

Chapter 2

Review of theory

This chapter provides a review of the mathematical concepts, in varying rigor, that have been used throughout the thesis. While serving the purpose of providing a review, as well as consistent definitions and notations, this chapter will also serve to connect the concept of transport barriers with the large body of scientific and mathematical literature on hyperbolic systems and Lyapunov exponents. This background information will help to clearly set the stage for the computational methods of finding transport barriers in flows, that we have used in this thesis.

The first section of this chapter reviews hyperbolic systems from a geometrical point of view of expansion and contraction in the tangent space and proceeds to give the definition and properties of Lyapunov exponents, following the work of Pesin and others [51], [18] and [81]. This forms the theoretical backbone for the computation of finite-time Lyapunov exponents and Lagrangian coherent structures that act as transport barriers. An alternative point of view that has emerged in recent years uses probabilistic methods from ergodic theory that find almost invariant sets, an optimal collection of sets that do not mix significantly, with other sets. One of the aims of the thesis is to relate the two methods at least in the case of simple flows. The second section therefore reviews the theory of Markov operators and the method of almost invariant sets.

While the background theory is self contained, certain liberties were taken in reviewing the mathematics. Where possible we have avoided excessive rigor and proofs often without explicitly stating so since we deal with physically intuitive systems. For a rigorous treatment of the background mathematical theories, the reader is referred to the references provided throughout the chapter.

2.1   Geometric approach to dynamical systems

The basic objects of study in (finite-dimensional) dynamical systems are the set of smooth flow maps $\phi_{t_0}^t$ on a differentiable manifold M

$$\phi_{t_0}^t : M \mapsto M \tag{2.1}$$

and the associated vector field defined by ordinary differential equations

$$\dot{\mathbf{x}} = \mathbf{f}(\mathbf{x}, t) \tag{2.2}$$

where $\mathbf{x} \in M$ and $\mathbf{f} : M \times \mathbb{R} \mapsto M$ is a smooth function. $\phi_{t_0}^t$ takes a point on M at time t_0 and maps it to another point on M at time time t. The explicit dependence on t_0 is necessary for time dependent systems. We will suppress this explicit dependence on initial time t_0 and final time t in the notation to avoid clutter, and instead use just ϕ. We will use the notation $\phi_{t_0}^t$ when necessary to highlight any specific properties for time dependent systems. The vector field f generated by ϕ is related to it by

$$\mathbf{f}(\mathbf{x}, s) = \frac{d}{dt}(\phi_{t_0}^t(\mathbf{x}))|_s \tag{2.3}$$

Linearization. Every smooth flow (2.1) induces a natural linear map between the cor-

responding tangent spaces defined by

$$d\phi : T_{\mathbf{x}}M \mapsto T_{\phi(\mathbf{x})}M \tag{2.4}$$

where $T_{\mathbf{x}}M$ is the tangent space at $\mathbf{x} \in M$ and t_0 is some initial time. The associated linearization of the vector field is

$$\delta\dot{\mathbf{x}} = \mathbf{A}\delta\mathbf{x} \tag{2.5}$$

where $\mathbf{A} = \frac{D\mathbf{f}(\mathbf{x},\mathbf{t})}{D\mathbf{x}}$. The linearization of the vector field (2.5) describes how a small perturbation $\delta\mathbf{x}(t_0)$ at time t_0 about a reference trajectory that passes through $\mathbf{x}$ at time t_0 evolves. Let $\Phi(\mathbf{x}, t_0, t)$ be the fundamental solution matrix of the tangent linearization (2.5). Using equations (2.3) and (2.4), we get

$$d\phi_{t_0}^t(\mathbf{x}) = \Phi(\mathbf{x}, t_0, t) \tag{2.6}$$

Solutions of the linearization of the vector field and the linearization of the flow map ϕ are both equivalent. One of the main aims of this thesis is to identify the special sets of trajectories about which perturbations experience the strongest growth. Such sets would then have the property of repelling (some) trajectories in their neighborhood. Similarly the repelling sets for time reversed flow will be attracting sets in the forward time flow. This idea can be defined more precisely by the concept of hyperbolicity.

Definition 2.1.1. *The flow map ϕ is said to be hyperbolic if the tangent space at every $\mathbf{x} \in M$ admits an invariant splitting $T_{\mathbf{x}}M = E_{\mathbf{x}}^s \oplus E_{\mathbf{x}}^u$ such that for vectors $\mathbf{v}_s \in E_{\mathbf{x}}^s$ and $\mathbf{v}_u \in E_{\mathbf{x}}^u$ there exist constants μ_s and μ_u such that $\left\| d\phi_{t_0}^t(\mathbf{v}_s) \right\| \leq C\mu_s^{(t-t_0)} \left\| \mathbf{v}_s \right\|$ and $\left\| d\phi_{t_0}^{-t+t_0}(\mathbf{v}_u) \right\| \leq C\mu_s^{(t_0-t)} \left\| \mathbf{v}_u \right\|$. The stable $E_{\mathbf{x}}^s$ and unstable $E_{\mathbf{x}}^u$ subspaces are invariant under the action of the flow, i.e., $d\phi_{t_0}^t(E_{\mathbf{x}}^s) \mapsto E_{\phi_{t_0}^t(\mathbf{x})}^s$ and $d\phi_{t_0}^t(E_{\mathbf{x}}^u) \mapsto E_{\phi_{t_0}^t(\mathbf{x})}^u$.*

The definition essentially says any arbitrary perturbation around a reference trajectory is a linear combination of exponentially growing and exponentially contracting perturbations. From the practical viewpoint of computations, the growth of a perturbation around

a reference trajectory can be quantified using the eigenvalues of the matrix $\mathbf{A}$ in equation (2.5). While hyperbolic systems have been extensively studied a modification of the above definition can allow us to study systems which are only partially hyperbolic [51], by allowing the existence of a center subspace $E_{\mathbf{x}}^c$. Vectors $\mathbf{v}_c \in E_{\mathbf{x}}^c$ do not grow or contract at an exponential rate. In this case the tangent space has an invariant splitting of the form $T_{\mathbf{x}} M = E_{\mathbf{x}}^s \oplus E_{\mathbf{x}}^u \oplus E_{\mathbf{x}}^c$, where $\oplus$ stands for the direct product.

2.2   Lyapunov exponents

Definition 2.2.1. *The linear propagator $L(\mathbf{x}, t_1, t_2)$ is defined as the linear transformation that takes solutions of the linearized vector field (2.5) at time t_1 to solutions at time t_2.*

$$L(\mathbf{x}, t_1, t_2) = \mathbf{\Phi}(\mathbf{x}, t_1, t_2)\mathbf{\Phi}^{-1}(\mathbf{x}, t_0, t_1) \tag{2.7}$$

with $\mathbf{\Phi}(\mathbf{x}, t_0, t_0) = I_n$, the identity matrix. Therefore

$$L(\mathbf{x}, t_0, t) = \mathbf{\Phi}(\mathbf{x}, t_0, t) \tag{2.8}$$

Definition 2.2.2. *The maximal Lyapunov exponent generated by L is defined as*

$$\sigma_1(\mathbf{x}) \overset{\limsup}{=}_{t \to \infty} \frac{1}{t} \log \|\mathbf{\Phi}(\mathbf{x}, t_0, t)\| \tag{2.9}$$

The quantity $\sigma_1(\mathbf{x})$ measures the maximum growth of a perturbation about a reference trajectory averaged over time, $t \to \infty$. The maximal Lyapunov vector, defined to be along the direction of asymptotic maximal stretching, is invariant under the flow. Hence if $\xi_1(\mathbf{x}, t_0)$ is the maximal Lyapunov vector at time t_0 then the linear propagator maps it to $\xi_1(\phi(\mathbf{x}, t_0, t), t)$ the Lyapunov vectors at t [51], [81], [24].

$$\xi_1(\phi(x, t_0, t), t) = L(\mathbf{x}, t_0, t)\xi_1(\mathbf{x}, t_0) \tag{2.10}$$

If the Lyapunov vector is determined at one time instant, then the linear propagator determines it for all time. This important property of the linear propagator has to be satisfied when the Lyapunov exponent is determined numerically. For almost all time t almost every vector in $S_1 = T_{\mathbf{x}}M$ grows asymptotically at a rate σ_1. The only vectors that do not grow at a rate σ_1 are those that are linearly independent of ξ_1. These vectors form a subspace $S_2 \subset S_1$. Continuing thus one can form a filtration of subspaces at each point $\mathbf{x} \in M$

$$S_n \subset S_{n-1} \subset ... \subset S_2 \subset S_1 = T_{\mathbf{x}}M = \mathbb{R}^n \qquad (2.11)$$

with $S_k \backslash S_{k+1} = \xi_k(\mathbf{x})$. Let the first n_1 Lyapunov exponents be positive, the next n_2 Lyapunov exponents be zero and the next n_3 Lyapunov exponents be negative, with $n_1 + n_2 + n_3 = n$. Then the stable subspace of linearized flow is $E_x^s = \bigcup_{k=1}^{k=n_1} \xi_k(\mathbf{x})$, the center subspace is $E_x^c = \bigcup_{k=n_1+1}^{k=n_1+n_2} \xi_k(\mathbf{x})$ and the unstable subspace is $E_x^u = \bigcup_{k=n_1+n_2+1}^{k=n} \xi_k(\mathbf{x})$ and these subspace are invariant by the property of the linear propagator and Lyapunov vectors (2.10). This makes the Lyapunov exponents an ideal tool to identify exponentially expanding and contracting subsets in phase space. However to apply this tool to time dependent systems, such as atmospheric flows, where the flow is not even known very well even for a few days into the future, one needs the finite-time Lyapunov exponent, which is reviewed in chapter 3.

2.3 Probabilistic approach to dynamical systems

One associates a statistical approach with systems containing a very large number of elements and uncertainties. However since the pioneering work of Ulam and Neumann[77] it has been understood that even one dimensional deterministic systems can generate densities of states that are amenable to a probabilistic treatment. In chapter 9 we will present some results on the relationship between probabilistic and geometric approaches with simple examples. Our motivation for this line of investigation is also to overcome the limitation of linearization imposed by equation (2.4). This section reviews Markov operators which play a central role

in the probabilistic approach and some preliminary definitions of measure spaces.

2.3.1 Markov operators

A detailed treatment of measure spaces, Lebesgue integration and L^p spaces is available in the textbooks by Royden [55] and Rudin [56]. We review only the pertinent theorems here without defining all the mathematical machinery and refer the reader to these books for further details. The basic mathematical object in the probabilistic approach is a measure space denoted by the triplet $(X, \mathcal{B}, \mu)$ where X is a set and $\mathcal{B}$ is the σ-algebra of measurable sets on X and μ is a measure. We are interested in the case where X is finite, μ is the Lebesgue measure and $\mathcal{B}$ is the σ-algebra of Lebesgue measurable sets.

Definition 2.3.1. *A function $f : X \mapsto \mathbb{R}$ is said to be measurable if the set $\{x : f(x) \leq \alpha\} \in \mathcal{B}$ for each α.*

Definition 2.3.2. *A measurable function f on X is said to belong to $L^p = L^p(X)$ space is $\int |f|^p \, d\mu < \infty$. Putting $p = 1$, L^1 space is the space of Lebesgue integrable functions.*

L^p spaces are linear, i.e. if $f_1, f_2 \in L^p$ then $\alpha_1 f_1 + \alpha_2 f_2 \in L^p$ for some constant α_1 and α_2.

Definition 2.3.3. *Let $(X, \mathcal{B}, \mu)$ be a measure space. A linear operator $P : L^1 \mapsto L^1$ is called a Markov operator if it satisfies the following properties :*

- *$Pf > 0$ for $f > 0$ and $f \in L^1$.*

- *$\|Pf\| = \|f\|$, where the norm is the L^1 norm.*

Properties 2.3.1. *For $f \in L^1$, we will write $f = f^+ - f^-$ where $f^+(x) = \max\{f(x), 0\}$ and $f^-(x) = \max\{-f(x), 0\}$ then*

- *$(Pf)^+ \leq Pf^+$*

- $(Pf)^- \leq Pf^-$

- $\|Pf\| \leq \|f\|$

The last property is the property of contraction, i.e., $\|P^n f\| = \|P(P^{n-1}f)\| \leq \|P^{n-1}f\|$.

Definition 2.3.4. *A function $f \in L^1$ is said to be a fixed point of the Markov operator P if $Pf = f$.*

Definition 2.3.5. *A measure ν is said to absolutely continuous with respect to the measure μ, if $\nu(B) = 0$ whenever $\mu(B) = 0$, for $B \in \mathcal{B}$. We write $\nu << \mu$.*

Theorem 2.3.1. *[**Radon-Nikodym**] Let $\nu << \mu$. Then there exists a function $f \in L^1$ such that for every $B \in \mathcal{B}$, $\nu(B) = \int_B f d\mu$. Further every $f \in L^1$ generates a measure $\nu << \mu$ in this manner. Moreover f is unique, [55].*

The Radon-Nikodym theorem is valid only for σ-finite algebras. A σ-algebra $\mathcal{B}$ is called σ-finite if there exist sets X_n such that $X = \bigcup_k^\infty X_k$ with each $\mu(X_k) < \infty$. Since all the problems we consider in this thesis are flows in $\mathbb{R}^n$ with the standard Borel σ-algebra, the requirement of σ-finiteness is taken care of. Henceforth we assume σ- finiteness without stating so.

An intuitive example of absolutely continuous measures and the Radon-Nikodym theorem is that of the mass and volume of a body. Mass and volume are measures of a physical body. Assuming there are no point masses, mass is absolutely continuous with respect to volume. If density (mass/volume) is finite, then the density function is Lebesgue integrable and the mass can be obtained from the volume and density using the Radon-Nikodym theorem. This example can be a useful physical analogy for the specific systems that we consider later.

2.3.2   Perron-Frobenius operator

Now going back to flows on manifolds, we can extend the definition of ϕ the flow map to $\phi : \mathcal{B} \mapsto \mathcal{B}$ such that $\phi(B) = \{\phi(x) : x \in B\}$ with $B \in \mathcal{B}$ and $X = M$.

Definition 2.3.6. *A measurable function or transformation ϕ on $(X, \mathcal{B}, \mu)$ is non singular if $\mu(\phi^{-1}(B)) = 0$ whenever $\mu(B) = 0$ for $B \in \mathcal{B}$*

The definition for non-singular transformation allows the shrinking of phase volumes, but not the shrinking of phase volumes to zero. Now let $f \in L^1$ and $f \geq 0$ and $\phi : M \mapsto M$ be a non singular transformation. Using the Radon-Nikodym theorem we define a measure ν

$$\nu(B) = \int_{\phi^{-1}(B)} f d\mu \tag{2.12}$$

If $\mu(B) = 0$ then $\mu(\phi^{-1}(B)) = 0$ and the Lebesgue integral of f over a set of zero measure is zero, i.e., $\nu(B) = 0$. This makes $\nu << \mu$. Therefore by the Radon-Nikodym theorem there exists a function denoted by $Pf \in L^1$ such that

$$\int_B Pf d\mu = \nu(B) = \int_{\phi^{-1}(B)} f d\mu \tag{2.13}$$

The same result can be obtained for any (not necessarily non-negative) function $f \in L^1$, by writing $f = f^+ - f^-$, where f^+ and f^- are both non negative. The Raydon-Nikodym theorem ensures the uniqueness of P. It can be easily verified that P is a Markov operator.

Definition 2.3.7. *Let $(X, \mathcal{B}, \mu)$ be a measure space. If $\phi : X \mapsto X$ is a nonsingular transformation the unique operator $P : L^1 \mapsto L^1$ defined in equation 2.13 is called the Perron-Frobenius operator for the flow ϕ, [38].*

Continuing with the analogy of the mass, density and volume of a physical body, the Perron-Frobenius operator describes the evolution of the density f or how the mass spreads. While this is a useful analogy, we have to note that the density that we will use later is a

probability density function. Up to now we have reviewed the mathematical machinery of Lyapunov exponents and the Perron-Frobenius operator. These will be revisited in chapter 3 and chapter 9 to define finite-time Lyapunov exponents, Lagrangian coherent structures and almost invariant sets respectively.

Chapter 3

Finite-time Lyapunov exponents

While Lyapunov exponents are very useful to study the sensitivity of trajectories, they have one major drawback; they are an asymptotic quantity requiring information of the flow for a very long time and in theory for all time. In many natural flows such as atmospheric flows, the flow is not known very well even for a few days into the future. Therefore one needs a modified version of the Lyapunov exponent that can quantify exponential stretching and contraction for finite-time scales. An intuitive and perhaps obvious definition of a finite-time Lyapunov exponent (FTLE) would replace the time $t \to \infty$ in (2.9) with a finite-time T. Despite the obvious nature of this definition, the definition and properties of FTLE and their role in determining transport barriers have been understood only in the last decade in the works of Wiggins, Haller, Marsden and Lekien [35], [30], [65] and [41].

The abstract definition of Lyapunov exponents for flows does not specify the norm to be used. However any norm that is used to compute the Lyapunov exponent has to satisfy the properties of the linear propagator, namely equation (2.10). The works of [81] and [35] showed that the norm obtained from the singular value decomposition (SVD) of $\mathbf{\Phi}(x; t_0; t)$ is particularly well suited for the computation of the finite-time version of the Lyapunov exponents. Haller, Marsden and Lekien used the spectral values of $\mathbf{\Phi}(x; t_0; t)$ obtained from its SVD, but approached it from a more geometrically intuitive approach of finding the

principal stretches. We review this approach to defining the FTLE and its properties.

3.1 Definition and properties of FTLE

For simplicity we consider a flow $\phi_{t_0}^t$ on $\mathbb{R}^n$. Consider a reference trajectory passing through the point $\mathbf{x}$ and a perturbed trajectory passing through the point $\mathbf{x} + \delta\mathbf{x}$ at time t_0. The flow $\phi_{t_0}^t$ maps these points to $\phi_{t_0}^t(\mathbf{x})$ and $\phi_{t_0}^t(\mathbf{x} + \delta\mathbf{x})$ at time t and the perturbation grows to $\delta\mathbf{x}(t_0 + t)$.

Expanding $\phi_{t_0}^t(\mathbf{x} + \delta\mathbf{x})$ in a Taylor series about the point $\mathbf{x}$ we get

$$\delta\mathbf{x}(t_0 + t) = \phi_{t_0}^t(\mathbf{x}) - \phi_{t_0}^t(\mathbf{x} + \delta\mathbf{x}) = \frac{d\phi_{t_0}^t}{d\mathbf{x}}\delta\mathbf{x}(t_0) + O(\left\|\delta\mathbf{x}^2(t_0)\right\|) \tag{3.1}$$

The norm or magnitude of $\delta\mathbf{x}(t_0 + t)$ can be found using the standard inner product on $\mathbb{R}^n$.

$$\left\|\delta\mathbf{x}(t)\right\| = \sqrt{\left\langle \frac{d\phi_{t_0}^t}{d\mathbf{x}}\delta\mathbf{x}(t_0), \frac{d\phi_{t_0}^t}{d\mathbf{x}}\delta\mathbf{x}(t_0) \right\rangle} = \sqrt{\left\langle \delta\mathbf{x}(t_0), \left(\frac{d\phi_{t_0}^t}{d\mathbf{x}}\right)^* \frac{d\phi_{t_0}^t}{d\mathbf{x}}\delta\mathbf{x}(t_0) \right\rangle} \tag{3.2}$$

where $*$ denotes the transpose. This frames the problem of finding the FTLE in terms of the Cauchy-Green deformation tensor, defined by

$$\mathbf{C} = \left(\frac{d\phi_{t_0}^t}{d\mathbf{x}}\right)^* \left(\frac{d\phi_{t_0}^t}{d\mathbf{x}}\right) \tag{3.3}$$

The maximum growth of a perturbation is therefore given by the maximum principal stretch, i.e., by the maximum eigenvalue of $\mathbf{C}$.

$$max\left\|\delta\mathbf{x}(t)\right\| = \sqrt{\lambda_{max}(C)}\left\|\delta\mathbf{x}(t_0)\right\|\xi_1(\mathbf{x}, t_0) \tag{3.4}$$

where $\xi_1(\mathbf{x}, t_0)$ is the eigenvector of C associated with λ_{max}. The growth in the perturbation depends on the initial point $\mathbf{x}$, initial time t_0 and the evolution or integration time $T = t - t_0$.

Definition 3.1.1. *The maximum FTLE is defined as*

$$\sigma(\mathbf{x}, t_0, T) = \frac{1}{T} \log\left(\sqrt{\lambda_{max}(\mathbf{C})}\right) \tag{3.5}$$

One can define the entire spectrum of FTLE $\sigma_1 > \sigma_2 > ... > \sigma_n$. The corresponding eigenvectors $[\xi_1\xi_2...\xi_n]$ form an orthonormal basis for the tangent space at $\mathbf{x}(t_0)$. Any initial perturbation $\delta\mathbf{x}(t_0)$ is a linear combination of these eigenvectors

$$\delta\mathbf{x}(t_0) = \delta\mathbf{x}_1(t_0)\xi_1 + ... + \delta\mathbf{x}_n(t_0)\xi_n \tag{3.6}$$

and the evolution of the perturbation can be described by the FTLE spectrum

$$\delta\mathbf{x}(t) = \delta\mathbf{x}_1(t_0)e^{\sigma_1 T}\xi_1(\phi(\mathbf{x}, t)) + ... + \delta\mathbf{x}_n(t_0)e^{\sigma_n T}\xi_n(\phi(\mathbf{x}, t)) \tag{3.7}$$

We have avoided the case of multiplicity of eigenvalues of $\mathbf{C}$ in the definition of FTLE. In this case the definitions remain essentially the same, but see [51] for further details.

The FTLE and the finite-time Lyapunov vectors computed from the SVD of $\mathbf{\Phi}$ are invariant for the finite-time T. Figure 3.1 explains the invariance of expanding and contracting subspaces. These are the local $E_{\mathbf{x}}^u$ and $E_{\mathbf{x}}^s$ in the tangent space $T_x M$ for an arbitrary trajectory. A standard examination of the SVD of $\mathbf{\Phi}$ will make this clear.

$$\mathbf{\Phi}(\mathbf{x}, t_0, t) = \mathbf{U}(\mathbf{x}, t_0, t)\mathbf{\Sigma}\mathbf{V}^*(\mathbf{x}, t_0, t) \tag{3.8}$$

$\mathbf{U}(\mathbf{x}, t_0, t)$ and $\mathbf{V}(\mathbf{x}, t_0, t)$ are the left and right singular vectors of $\mathbf{\Phi}$ respectively and $\mathbf{\Sigma}$ is the diagonal matrix of the singular values.

$$\mathbf{C} = \mathbf{\Phi}(\mathbf{x}, t_0, t)^*\mathbf{\Phi}(\mathbf{x}, t_0, t) = \mathbf{V}(\mathbf{x}, t_0, t)\mathbf{\Sigma}^2\mathbf{V}^*(\mathbf{x}, t_0, t) \tag{3.9}$$

Let $s \in [t_0, t]$ then,

$$\mathbf{U}(\mathbf{x}, t_0, s) = \mathbf{L}(\mathbf{x}, t_0, s)\mathbf{V}(\mathbf{x}, t_0, t) \tag{3.10}$$
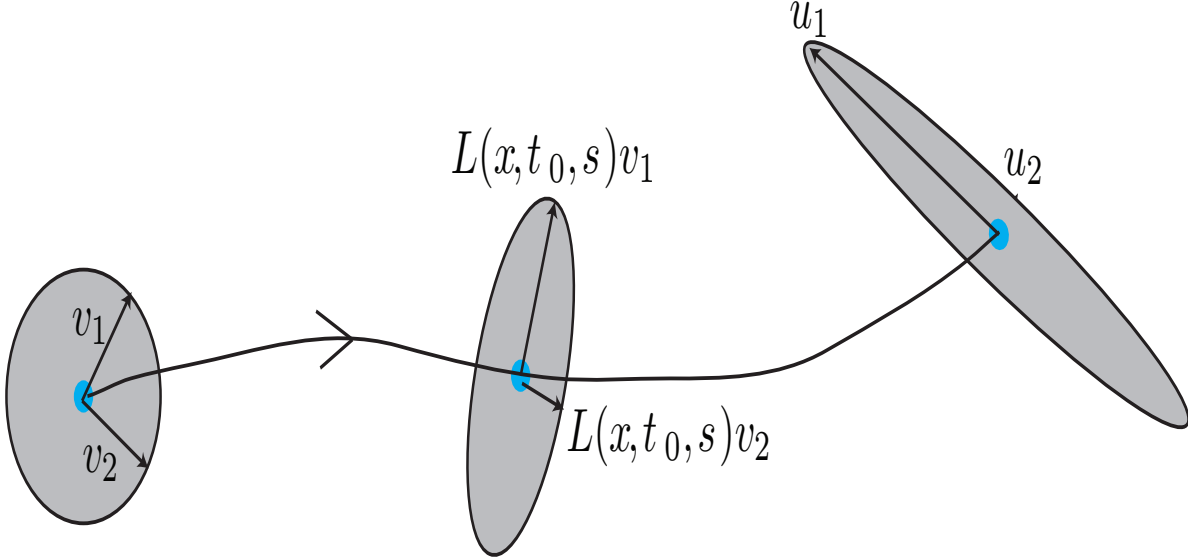
Figure 3.1: The invariance of the singular vectors for the finite-time $T = t - t_0$.

and

$$\mathbf{U}(\mathbf{x}, s, t) = \mathbf{L}(\phi(\mathbf{x}, t_0, s), s, t))\mathbf{V}^*(\mathbf{x}, s, t) \tag{3.11}$$

The claim is that $\mathbf{U}(\mathbf{x}, t_0, s) = \mathbf{V}(\mathbf{x}, t_0, s)$. This is easy to verify by taking the composition of the linear propagators $\mathbf{L}(\mathbf{x}, t_0, t) = \mathbf{L}(\phi(\mathbf{x}(t_0, s), s, t) \circ \mathbf{L}(\mathbf{x}, t_0, s)$ to get

$$\mathbf{U}(\mathbf{x}, t_0, t) = \mathbf{L}(\phi(\mathbf{x}, t_0, s), s, t)\mathbf{L}(t_0, s, \mathbf{x})\mathbf{V}(\mathbf{x}, t_0, t) = \mathbf{L}(\phi(\mathbf{x}, t_0, s))\mathbf{U}(\mathbf{x}, t_0, s) \tag{3.12}$$

But $\mathbf{V}(\mathbf{x}, t_0, s) = \mathbf{L}(\phi(\mathbf{x}, t_0, s))\mathbf{U}(\mathbf{x}, t_0, s)$ which verifies the claim. Therefore the FTLE and the associated singular vectors defined by the SVD of $\mathbf{\Phi}$ have the properties of Lyapunov exponents defined in chapter 2; maximum expansion and invariance under the action of the flow for a finite time $T = t - t_0$.

3.2 Computation of FTLE

3.2.1 Finite difference method

In general the FTLE is dependent on the initial position $\mathbf{x}$, initial time t_0 and T. Therefore to understand stretching and contraction of trajectories, one would have to compute a FTLE field, which in practice can only be computed at a finite number of points in the domain. The deformation tensor $\mathbf{\Phi}$ can be computed using finite differences. The value of the FTLE at nodal points in the finite difference grid then represents the stretching of a neighborhood which is the size of a cell. The size of the grid can be chosen depending on the scales of interest in the flow. A schematic figure illustrating the finite difference method in two dimensions is shown in figure 3.2.
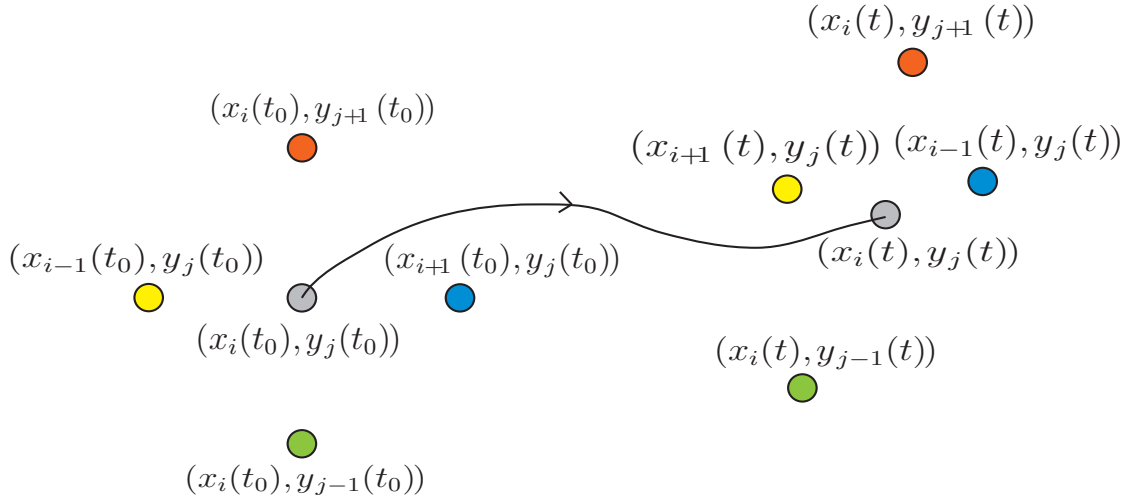
Figure 3.2: Finite difference method : A reference point (in black) and four neighboring particles are integrated for a finite time T.

In finite difference notation the gradient of the flow map is :

$$\frac{d\phi}{d\mathbf{x}} = \begin{pmatrix} \frac{x_{i+1,j}(t_0+t)-x_{i-1,j}(t_0+t)}{x_{i+1,j}(t_0)-x_{i-1,j}(t_0)} & \frac{x_{i,j+1}(t_0+t)-x_{i,j-1}(t_0+t)}{y_{i+1,j}(t_0)-y_{i-1,j}(t_0)} \\ \frac{y_{i+1,j}(t_0+t)-y_{i-1,j}(t_0+t)}{x_{i,j+1}(t_0)-x_{i,j-1}(t_0)} & \frac{y_{i,j+1}(t_0+t)-y_{i,j-1}(t_0+t)}{y_{i,j+1}(t_0)-y_{i,j-1}(t_0)} \end{pmatrix} \tag{3.13}$$

3.2.2 An example - double gyre flow

We illustrate the method with the example of a time dependent double gyre flow [41], a two dimensional time dependent flow, frequently encountered in large scale ocean flow and analytical models of Rayleigh-Bénard convection cells. It is defined by the stream function $\psi(x, y, t) = A \sin(\pi f(x, t)) \sin(\pi y)$, with $f(x, t) = a(t)x^2 + b(t)x$, $a(t) = \epsilon \sin(\omega t)$ and $b(t) = 1 - 2\epsilon \sin(\omega t)$ over the domain $[0, 2] \times [0, 1]$. The velocity field is given by

$$u = -\pi A \sin(\pi f(x)) \cos(\pi y) \tag{3.14}$$

$$v = \pi A \cos(\pi f(x)) \sin(\pi y) \frac{df}{dx} \tag{3.15}$$

The flow is a periodic array of cells in which the streamlines are concentric circles. We chose a representative set of parameter values; $A = 0.1$, $\omega = 0.2\pi$ and $\epsilon = 0.25$. The centers of the cells oscillate with a frequency ω on the horizontal axis. The FTLE field for this flow is shown in figure 3.3(a). When the FTLE field is viewed as a surface the regions of high FTLE become topographic ridges as shown in figure 3.3(b)

(a) FTLE field   (b) FTLE field as a surface
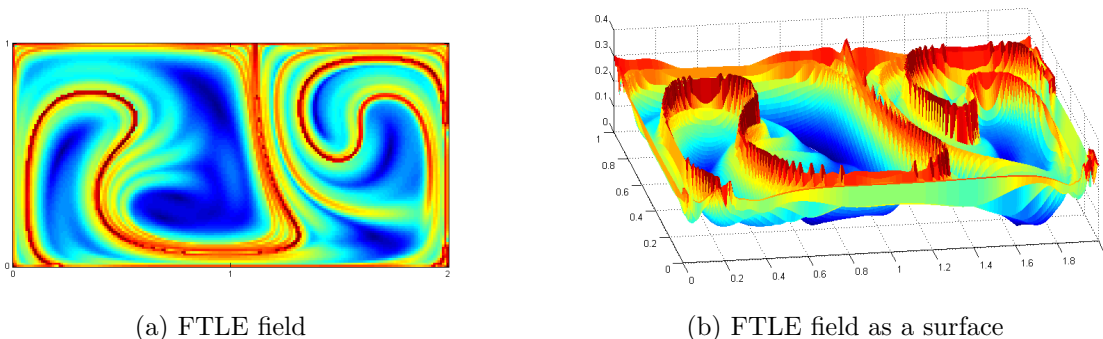
Figure 3.3: FTLE field for the double-gyre flow for an integration time of $T = 10$.

The ridge can be extracted easily in this example by setting a threshold on the FTLE value. Loosely speaking, a ridge is the set of points whose FTLE value is locally high. The ridges in the FTLE field are shown in red in figure 3.4. A more precise definition of a ridge is given in the next section.
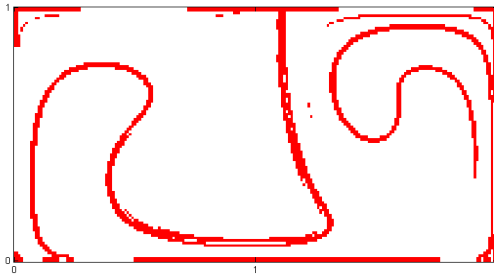
Figure 3.4: Ridges in FTLE field for the double-gyre flow shown in figure 3.3.

3.3 Lagrangian coherent structures

3.3.1 Definition of LCS

The leading FTLE gives the time averaged rate of stretching in a neighborhood around a reference trajectory. It is intuitively clear that regions of the phase space separated by locally high values of FTLE will stretch and separate. The sets with high FTLE act as repelling barriers in the flow. This intuitive idea of barriers is formalized by the concept of Lagrangian coherent structures (LCS) due to Lekien, Shadden and Marsden [65] [41].

Definition 3.3.1. *LCS are codimension one ridges in the scalar FTLE field $\sigma(\mathbf{x}, t_0, t)$.*

Ridges can be defined precisely by appealing to differential geometric quantities as in [20].

Definition 3.3.2. *Let $\sigma(\mathbf{x})$ be the FTLE scalar field defined over the domain, a smooth n dimensional manifold M. Let λ_i, $1 \leq i \leq n$ the eigenvalues of $\nabla^2 \sigma$ ordered such that $\lambda_i \leq \lambda_j$ for $1 \leq i \leq j \leq n$. Let $\mathbf{v}_i$ be the corresponding eigenvectors (column vectors). Let $\mathbf{V} = [\mathbf{v}_1, \mathbf{v}_2, ..., \mathbf{v}_{n-1}]$. A point $\mathbf{x}$ lies on a ridge or is said to be a ridge point if $V \nabla \sigma = 0$ and $\lambda_{n-1} \leq 0$.*

The above definition is not easy to work with for $n \geq 3$. In two dimensions, ridges have an intuitive analogy to topographic ridges. Applying this analogy to a two dimensional FTLE

(a)$\kappa_1 = 0$, $\kappa_2 < 0$ (b)$\kappa_1 < 0$, $\kappa_2 < 0$ (c)$\kappa_1 > 0$, $\kappa_2 < 0$
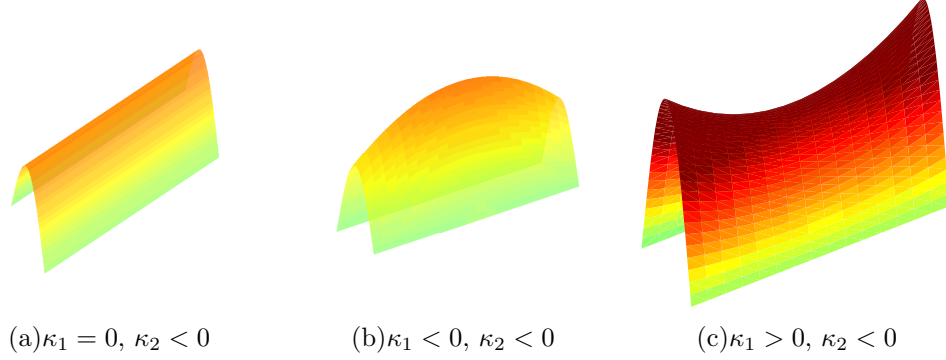
Figure 3.5: The three types of ridges and the corresponding conditions on the principal curvatures. For all three cases $\sigma(x,y) > 0$

field, we reformulate the definition of a ridge in a modified form. Let $\kappa_1(x,y) \geq \kappa_2(x,y)$ be the eigenvalues of the Hessian of the FTLE field, $\nabla^2\sigma$. These eigenvalues are the principal curvatures of the two dimensional surface σ. A point (x,y) lies on a ridge, or is a ridge point, if $\kappa_2(x,y) < 0$ and $\sigma(x,y) > 0$. Three types of ridges which satisfy these criteria are shown in figure 3.5.

The definitions and the computational procedure reviewed so far are for repelling LCS. The same definitions and computational procedure can be used with a small modification to find attracting LCS. By finding the FTLE in backward time, from t_0 to t with $t < t_0$, one can find repelling LCS in backward time which act as attracting LCS in forward time.

3.3.2   Flux across the LCS

The flux across a ridge in the FTLE field is negligible. An expression for the actual flux across a ridge has been derived in [65] and [41]. The main results are reviewed here.

Definition 3.3.3. *For all t let $l(\mathbf{x}, t)$ be a function defined by the following conditions :*

- *$l(\mathbf{x}, t) = \|\mathbf{x} - \mathbf{x}_q\|$ where $\mathbf{x}_q$ is a point on the LCS closest to $\mathbf{x}$.*

- *$l(\mathbf{x}, t) \langle \mathbf{x} - \mathbf{x}_q, \mathbf{n}(\mathbf{x}_q, t) \rangle \leq 0$ where $\mathbf{n}(\mathbf{x}_q, t)$ is the unit vector normal to the ridge at $\mathbf{x}_q$*

and $\langle,\rangle$ is the inner product on M.

The function $l(\mathbf{x}, t)$ gives the signed distance of a point to the LCS. Points on either side of the LCS have opposite signs of $l(\mathbf{x}, t)$. More precisely the above two properties of the LCS hold in a neighborhood of the LCS. By definition the LCS are zero level sets of $l(\mathbf{x}, t)$.

$$\frac{dl(\mathbf{x}, t)}{dt} = \frac{\partial l}{\partial \mathbf{x}} \cdot \frac{\partial \mathbf{x}}{\partial t} - \frac{\partial l}{\partial \mathbf{x}_q} \cdot \frac{\partial \mathbf{x}_q}{\partial t} \tag{3.16}$$

$$\frac{\partial l}{\partial \mathbf{x}} = \nabla l = \frac{\mathbf{x} - \mathbf{x}_q}{\|\mathbf{x} - \mathbf{x}_q\|} = \mathbf{n}(\mathbf{x}_q, t) \tag{3.17}$$

$$\frac{dl}{dt} = \nabla l. \left(\frac{d\mathbf{x}}{dt} - \frac{d\mathbf{x}_q}{dt} \right) \tag{3.18}$$

The flux across LCS, γ is given by

$$\gamma = \int_{LCS} \left(\frac{dl}{dt} \right)_{l=0} ds \tag{3.19}$$

where the integration is along the LCS.

Along the LCS

$$\left(\frac{dl}{dt} \right)_{l=0} = \frac{\langle \mathbf{t}, \nabla \sigma \rangle}{\langle \mathbf{n}, \nabla^2 \sigma \mathbf{n} \rangle} \left\langle \mathbf{t}, \frac{\partial l}{\partial t} - \mathbf{A}\mathbf{n} \right\rangle + O\left(\frac{1}{t - t_0} \right) \tag{3.20}$$

where $\mathbf{A}$ is the Jacobian of the flow vector field. The first term on the right approaches zero for well defined ridges. This result shows that LCS are minimum flux barriers and in most applications the flux across LCS approaches zero.

A subtle point has to be made clear here. If $\mathbf{x}_q$ is a point on a FTLE ridge, then points in a small neighborhood on either side of it do not cut through the points on the ridge during the finite time $t - t_0$. The intuitive interpretation of the results in [65] and [41] estimate the

relative velocity of a moving LCS and the underlying flow field. If this relative velocity is zero then the LCS is a material surface and hence an invariant manifold.

3.3.3 An example to show the limitation of LCS

Repelling (attracting) LCS have been interpreted as the time dependent analogues of stable (unstable) manifolds. However one has to be careful with such an interpretation. We give a simple example to illustrate what could go wrong.

Example Consider a flow on $\mathbb{R}^2 = (x, y)$ given by

$$\begin{pmatrix} \dot{x} \\ \dot{y} \end{pmatrix} = \begin{pmatrix} -1 & 0 \\ 0 & 1 \end{pmatrix} \begin{pmatrix} x \\ y \end{pmatrix} \tag{3.21}$$

The above flow is hyperbolic since its tangent space admits an invariant splitting into stable and unstable subspaces. The solution of the above equation $x(t) = x(t_0)e^{-(t-t_0)}$ and $y(t) = y(t_0)e^{t-t_0}$. If $(x_1(t_0), y_1(t_0))$ and $(x_1(t_0) + \delta x(t_0), y_1(t_0) + \delta y(t_0))$ are two close by initial conditions then the growth of the perturbation is $\delta x(t) = \delta x(t_0)e^{-(t-t_0)}$ and $\delta y(t) = \delta y(t_0)e^{t-t_0}$. This stretching is independent of the initial conditions, all sets in the phase space have the same rate of stretching and contraction. The Lyapunov exponents (and the FTLEs) are 1 and -1 respectively for all initial conditions. There are no ridges in the FTLE field and hence no LCS. In the example of the linear system, stable and unstable manifolds of the fixed point exist but there is no repelling nor attracting LCS. This is true for all linear time independent systems. A Nonuniform rate of expansion of sets in the domain M is a necessary condition for the existence of ridges in the FTLE field, i.e., the existence of LCS.

Chapter 4

Partial FTLE and partial LCS with examples

Lagrangian coherent structures are an excellent way to visualize flow patterns and minimal flux barriers in flows. However many problems in which the theory of LCS is sought to be applied tend to be high dimensional systems. LCS cannot be easily visualized if the flow is in more than three dimensions, though one can visualize it in slices as for example in the planar elliptic restricted three body problem, [26]. Even for three dimensional flows performing sensitivity computations over a three dimensional grid of points can be computationally expensive. Moreover only a lower dimensional subset of the full domain could be of interest or the flow in some of the dimensions could be slowly evolving. For example in atmospheric and ocean flows reviewed in chapter 7, the vertical component of the fluid is at least an order of a magnitude less than the horizontal component of the velocity. For such cases it is useful to restrict LCS computations over a subspace of the domain. We refer to a sensitivity field restricted to a subspace of the domain, as a partial LCS denoted by LCS_p. The question is whether LCS_p are slices of the codimension-one LCS, i.e., are they the intersection of the LCS with a subset of a subspace of the domain? In this section it is shown that the general answer is negative. We also present results on the partial LCS of two examples.

4.1   Partial finite-time Lyapunov exponents

First it is observed that the asymptotic Lyapunov exponents have the desired partial LCS property. Let $\xi(\mathbf{x}, t_0) \in T_x M$ be an arbitrary vector. $\xi(\mathbf{x}, t_0)$ can be expressed as a linear combination of Lyapunov (basis) unit vectors $\xi_j(\mathbf{x}, t_0)$.

$$\xi(\mathbf{x}, t_0) = \sum_{j=1}^{n} k_j \xi_j(\mathbf{x}, t_0) \tag{4.1}$$

or in vector notation

$$\xi(\mathbf{x}, t_0) = \begin{pmatrix} k_1 \xi_1(\mathbf{x}, t_0) \\ . \\ . \\ . \\ k_n \xi_n(\mathbf{x}, t_0) \end{pmatrix} \tag{4.2}$$

Let $\Phi((x), t_0)$ be the the fundamental solution matrix for the linearized flow. As stated in the previous section, the induced linear flow over the tangent space equation (2.4), maps the Lyapunov vectors at time t_0 to Lyapunov vectors at time t.

$$\begin{aligned} \xi(\phi(\mathbf{x}, t)) &= \Phi(\mathbf{x}, t_0)\xi(\mathbf{x}, t_0) = \Phi(\mathbf{x}, t_0)[k_1\xi_1(\mathbf{x}, t_0), ..., k_n\xi_n(\mathbf{x}, t_0)]^* \tag{4.3} \\ &= [k_1\xi_1(\phi(\mathbf{x}), t)e^{\sigma_1(t-t_0)}, ..., \xi_n(\phi(\mathbf{x}), t)e^{\sigma_n(t-t_0)}]^* \tag{4.4} \end{aligned}$$

Using the notation of the filtration of sets in (2.11) $\xi_1 \in S_1$ and $S_2 = \text{span}\{\xi_2, ..., \xi_n\}$. Since S_2 is spanned by only $n-1$ vectors it follows that S_2 is a set of zero measure. So almost every vector in $T_{\mathbf{x}M}$ and in particular $\xi(\mathbf{x}, t_0)$ grows at an asymptotic rate of e^{σ_1}. In the asymptotic limit the 'partial' Lyapunov exponents have the exact value of the Lyapunov exponents at every $\mathbf{x} \in M$.

$$\limsup_{t \to \infty} \frac{1}{(t - t_0)} \log \left(\frac{\|\xi(\phi(\mathbf{x}, t_0), t)\|}{\|\xi(\mathbf{x}, t_0)\|} \right) = \sigma_1 \tag{4.5}$$

because $\lim_{t\to\infty} \frac{1}{(t-t_0)} \log k_1 = 0$, for $k_1 \neq 0$. This is true for any vector except those chosen from the subspace $S_1 \backslash S_2$, which has zero measure. Therefore once could choose perturbations in any subspace as long as $k_1 \neq 0$. This property is implicitly used in the literature on computing Lyapunov exponents. For example the method of finding Lyapunov exponents by Swinney et. al [80] measures the growth of an arbitrary perturbation and averages it for a long enough time to find the Lyapunov exponent.

In equation (4.5) the asymptotic nature of the Lyapunov exponent plays a critical role. In the case of the case of finite-time Lyapunov exponents, the relation between partial LCS and the true LCS depends on the time scale $T = t - t_0$. The SVD of $\Phi(\mathbf{x}, t_0, t)$ or $\frac{d\phi(\mathbf{x},t_0,t)}{d\mathbf{x}}$ gives n singular vectors $\mathbf{U}$ and $\mathbf{V}$ that form an orthogonal basis for $T_{\phi(\mathbf{x},t_0,t)}$ and $T_{\mathbf{x}}M$ respectively. Every vector $\xi(\mathbf{x}, t_0) \in T_{\mathbf{x}}M = \mathbb{R}^n$ can be expressed as a linear combination of the column vectors of $\mathbf{V}$.

$$\xi(\mathbf{x}, t_0) = \sum_{j=1}^{n} k_j \mathbf{v}_j(\mathbf{x}, t_0, t) = [\mathbf{v}_1(\mathbf{x}, t_0, t), ..., \mathbf{v}_2(\mathbf{x}, t_0, t)]\mathbf{K} \tag{4.6}$$

$\mathbf{K}$ being a diagonal matrix with $\mathbf{K}_{jj} = k_j$. Now without loss of generality it can be assumed that the diagonal matrix Σ is arranged such that $\Sigma_{11}^2 \geq \Sigma_{22}^2 \geq ... \geq \Sigma_{nn}^2$ making $\mathbf{v}_1$ the singular vector, correspond to the maximum eigenvalue of Σ^2. Again applying the induced linear map Φ over the tangent space and using the SVD of Φ

$$\Phi(\mathbf{x},, t_0)\xi(\mathbf{x}, t_0) = \mathbf{U}\Sigma\mathbf{V}^*\mathbf{V}(\mathbf{x}, t_0)\mathbf{K} = \mathbf{U}\Sigma\mathbf{K} \tag{4.7}$$

The growth in magnitude of the arbitrary vector in time $T = t - t_0$ is

$$\|\xi(\phi(\mathbf{x}, t_0, t))\| = \sqrt{\langle \xi(\phi(\mathbf{x}, t_0, t)), \xi(\phi(\mathbf{x}, t_0, t)) \rangle} = \sqrt{(\mathbf{U}\Sigma\mathbf{K})^*\mathbf{U}\Sigma\mathbf{K}} = \sqrt{\mathbf{K}\Sigma^2\mathbf{K}} \tag{4.8}$$

On a finite-time scale $T = t - t_0$ the maximum Lyapunov exponent will not be the same

as the partial exponents because of the scalars k_j. The partial FTLE spectrum is given by

$$(\sigma_j)_p = \frac{1}{T} \ln \sqrt{\Sigma_{jj}^2 \mathbf{K}_{jj}^2} \tag{4.9}$$

Even the direction of maximum growth is dependent on the values of $\mathbf{K}_{jj}$ and T. So in general the partial FTLE is only a measure of sensitivity to perturbations in specific directions and the ridges in the partial FTLE field are not slices of the true LCS. However in some special cases the ridges in the partial FTLE field are suggestive of the true LCS. Two such cases are considered here.

- *Dissipative systems* : Dissipative systems with a global attractor are a special case where the partial LCS can be relatively computationally inexpensive and have the property of dynamical barriers. An example of such a system is presented in chapter 5 in detail. Here we provide a brief description of the method of partial LCS in a two dimensional dissipative flow.

  Consider a two dimensional dissipative flow $\phi : \mathbb{R}^2 \mapsto \mathbb{R}^2$. Now suppose that $y = 0$, i.e., the x axis is the global attractor. The gradient of the flow map (and the induced linear map over the tangent space) in finite difference notation is given by

$$\frac{d\phi}{d\mathbf{x}} = \begin{pmatrix} \phi_{x,x} & \phi_{x,y} \\ \phi_{y,x} & \phi_{y,y} \end{pmatrix} = \begin{pmatrix} \frac{x_{i+1,j}(t_0+t)-x_{i-1,j}(t_0+t)}{x_{i+1,j}(t_0)-x_{i-1,j}(t_0)} & \frac{x_{i,j+1}(t_0+t)-x_{i,j-1}(t_0+t)}{y_{i,j+1}(t_0)-y_{i,j-1}(t_0)} \\ \frac{y_{i+1,j}(t_0+t)-y_{i-1,j}(t_0+t)}{x_{i+1,j}(t_0)-x_{i-1,j}(t_0)} & \frac{y_{i,j+1}(t_0+t)-y_{i,j-1}(t_0+t)}{y_{i,j+1}(t_0)-y_{i,j-1}(t_0)} \end{pmatrix} \tag{4.10}$$

  Since $y = 0$ is the attractor, the second row converges to zero. Setting the second row and second column of $\frac{d\phi}{d\mathbf{x}}$ to zero

$$\frac{d\phi}{d\mathbf{x}} \frac{d\phi^*}{d\mathbf{x}} = \begin{pmatrix} \phi_{x,x}^2 + \phi_{x,y}^2 & 0 \\ 0 & 0 \end{pmatrix} \tag{4.11}$$

  The maximum Lyapunov exponent is completely determined by the just the first term. A similar result is used to compute the partial LCS for the motion of inertial particles

in a fluid, in chapter 5.

- *Flows with 'layers'* : An example is atmospheric flow. The movement of air at a height of $100m$ above the ground has a layered profile. The wind velocity tangential to the ground is at least an order of magnitude more than the vertical velocity for pressure levels. Moreover the flow has vertical rigidity, i.e., that is the air at closely spaced heights moves with almost the same horizontal velocity. Meteorological data too shows only a small variation in the tangential velocities for variations in vertical height. Therefore transport barriers can be studied using a partial LCS in the horizontal direction only.

In the following sections two examples of partial LCS are shown.

4.2   Partial FTLE for a perturbed pendulum

First we take a simple example of a periodically forced pendulum with dissipation. Though this example does not have a global attractor nor is it a 'layered' flow, it provides a good starting point to study the partial FTLE since we can easily compute the true LCS for verification. Consider the vector field on $\mathbb{R}^2$

$$\dot{x} \;=\; y \tag{4.12}$$

$$\dot{y} \;=\; -\sin{(x)} - \epsilon y \sin{(\omega t)} \tag{4.13}$$

In the absence of the term $\epsilon y \sin{(\omega t)}$ which introduces both periodic forcing and dissipation, the system reduces to the simple pendulum with two saddle type fixed points at $(0, \pm\pi)$ and a center type fixed point at $(0,0)$, with the vector field being periodic with period 2π. The heteroclinic trajectories connecting the saddles at $(0, \pm\pi)$ form a separatrix in the phase space. In this case the heteroclinic trajectories are also the LCS due to the high exponential separation of the periodic trajectories from the non periodic trajectories around this trajectory. The addition of a small forcing and dissipation (small ϵ) breaks down the

heteroclinic trajectory and leads to a heteroclinic tangle in a small neighborhood of the original heteroclinic trajectory, [79], formed by the transversal intersection of the stable and unstable manifolds of saddle points. The stretching in phase space is high in a neighborhood of the heteroclinic tangle [79] and [78]. We choose $\omega = 1$ and $\epsilon = 0.1$ and use the ODE45 integrator in Matlab for the simulation, with a grid size of 0.1 on the domain $[-4, 4] \times [-4, 4]$. The FTLE field is shown in figure 4.1 for various initial times. The regions of high FTLE shown in red are the LCS.

The gradient of the the flow map ϕ for this flow is the same as in equation (4.10). The variation of the final position in the x subspace with respect to variations of initial positions in only x is given by $\phi_{x,x}$. Similarly $\phi_{x,y}$ is the variation of the final position in the x subspace with respect to variations of initial positions in the y subspace only, $\phi_{y,x}$ is the variation of the final position in the y subspace due to variation in the x subspace only and $\phi_{y,y}$ is the variation in of the final position in the y subspace due to initial variation in the x subspace only. The corresponding partial FTLEs denoted by σ_{xx}, σ_{xy}, σ_{yx} and σ_{yy} are given by

$$
\begin{aligned}
\sigma_{xx} &= \frac{1}{T} \log \sqrt{\phi_{x,x}^2} \\
\sigma_{xy} &= \frac{1}{T} \log \sqrt{\phi_{x,y}^2} \\
\sigma_{yx} &= \frac{1}{T} \log \sqrt{\phi_{y,x}^2} \\
\sigma_{yy} &= \frac{1}{T} \log \sqrt{\phi_{y,y}^2}.
\end{aligned}
\tag{4.14}
$$

More precisely the $\sigma_{xx} = \frac{1}{T} \log \sqrt{\lambda_{max}(\phi_{x,x}^* \phi_{x,x})}$. But we have omitted this because the sub matrices $\phi_{x,x}$, $\phi_{x,y}$, $\phi_{y,x}$ and $\phi_{y,y}$ are single numbers and so partial FTLE formulae in eq 4.14 are still correct.

The partial FTLEs are plotted in figure 4.2 - 4.5 at various instants of time.

(a)$t = 0$

(b)$t = 0.5\pi$

(c)$t = \pi$

(c)$t = 2\pi$
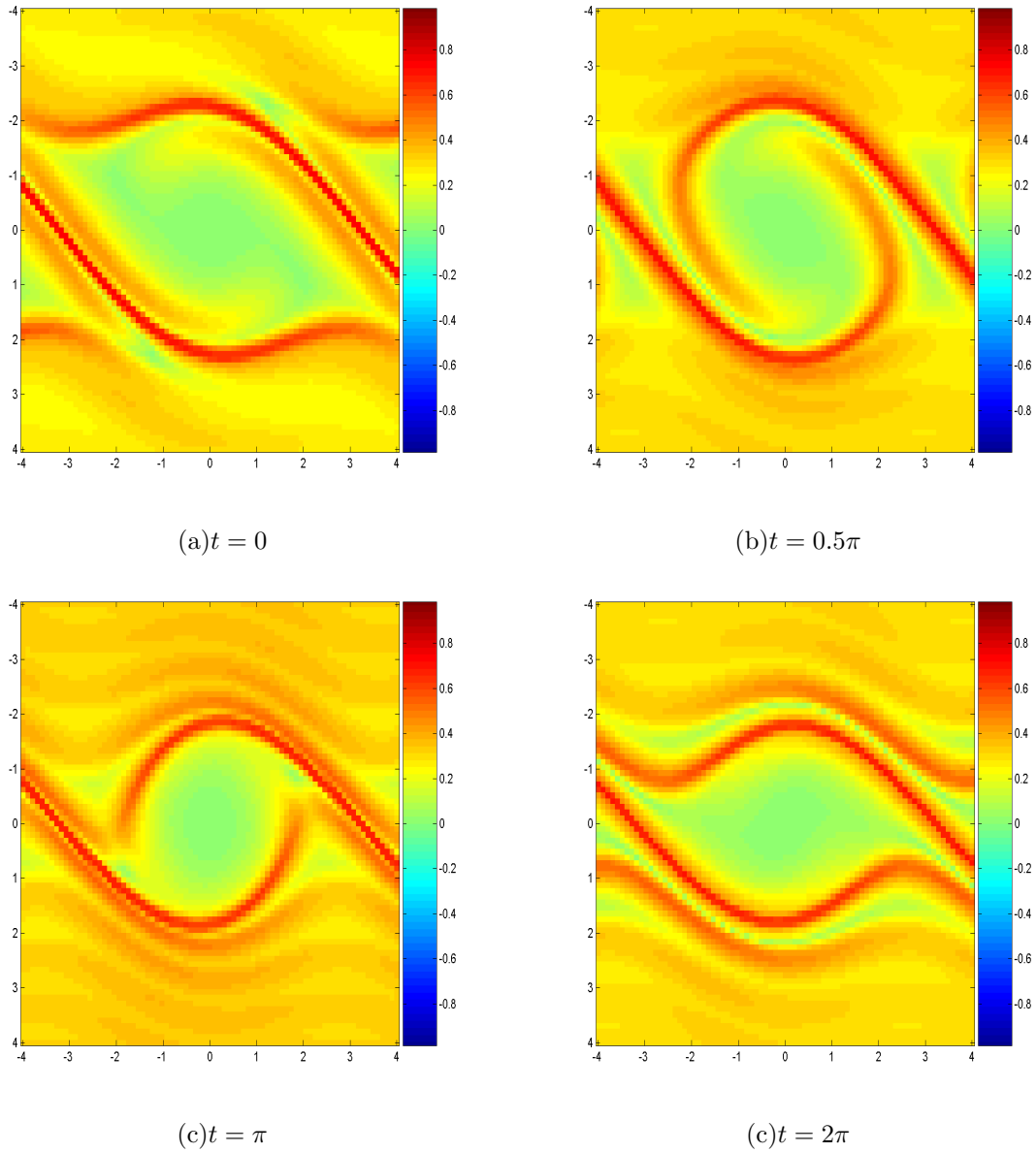
Figure 4.1: FTLE field for different initial times. $\epsilon = 0.1$, $\omega = 1$ and integration time, $T = 1$.

On comparing the partial FTLEs with true FTLE field, the actual values of the partial FTLEs do not match with value of the true FTLE. This is obviously true because the maximum rate of expansion need not be in either the x or the y direction. However what we are interested in is the ridge structure of the FTLE field, i.e., the location of ridges in the FTLE field and the partial FTLE fields. Comparing the locations of the ridges in the partial

(a)$t_0 = 0$

(b)$t_0 = 0.5\pi$

(c)$t_0 = \pi$

(c)$t_0 = 2\pi$
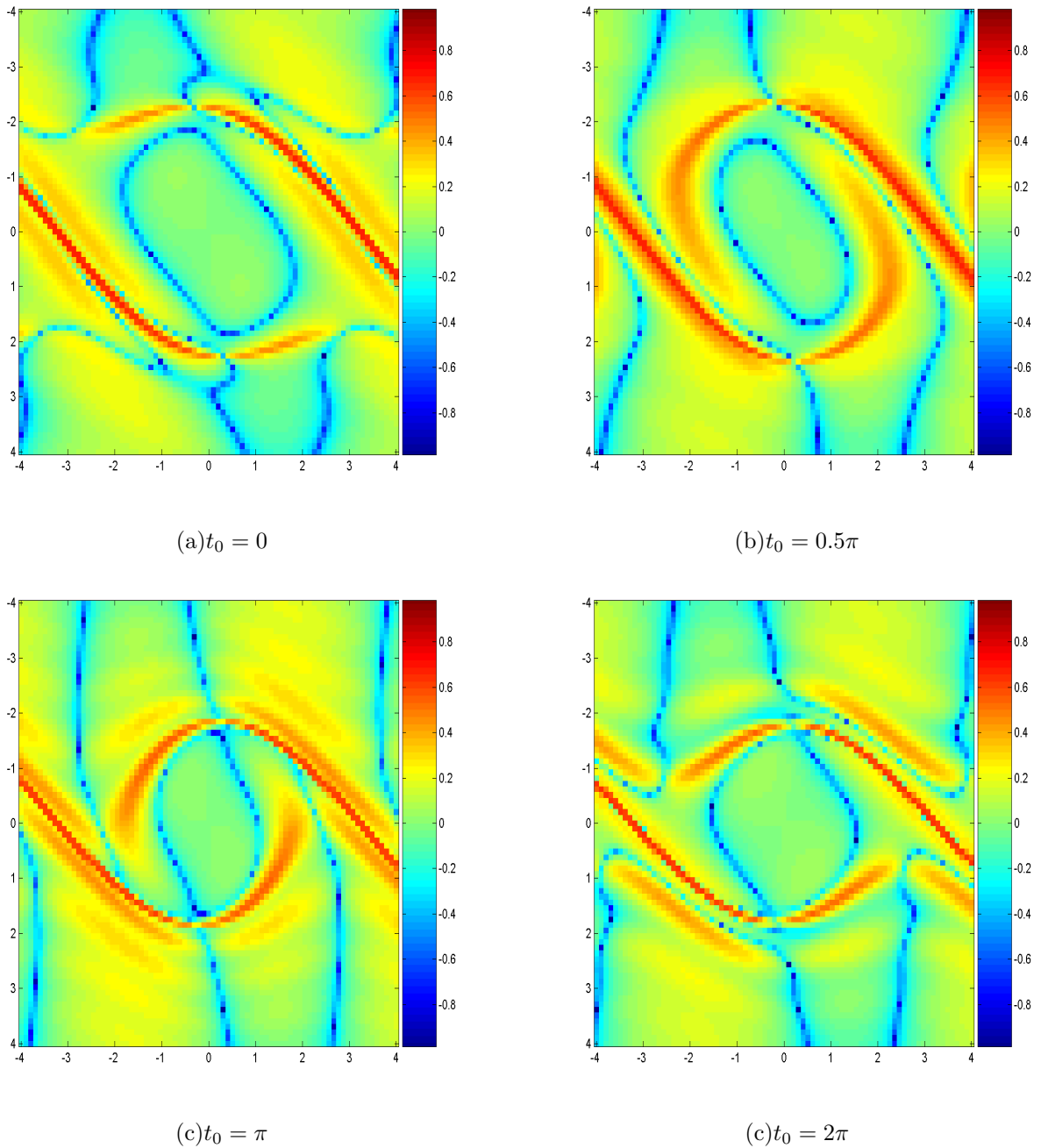
Figure 4.2: Partial FTLE σ_{xx} field for different initial times. $\epsilon = 0.1$, $\omega = 1$ and integration time, $T = 1$.

FTLE fields it can be seen that all the four partial FTLE identify the main transport barrier very effectively. In particular the partial FTLE $\sigma_{x,y}$ in figure 4.3 has a ridge structure that is

(a)$t_0 = 0$

(b)$t_0 = 0.5\pi$

(c)$t_0 = \pi$

(c)$t_0 = 2\pi$
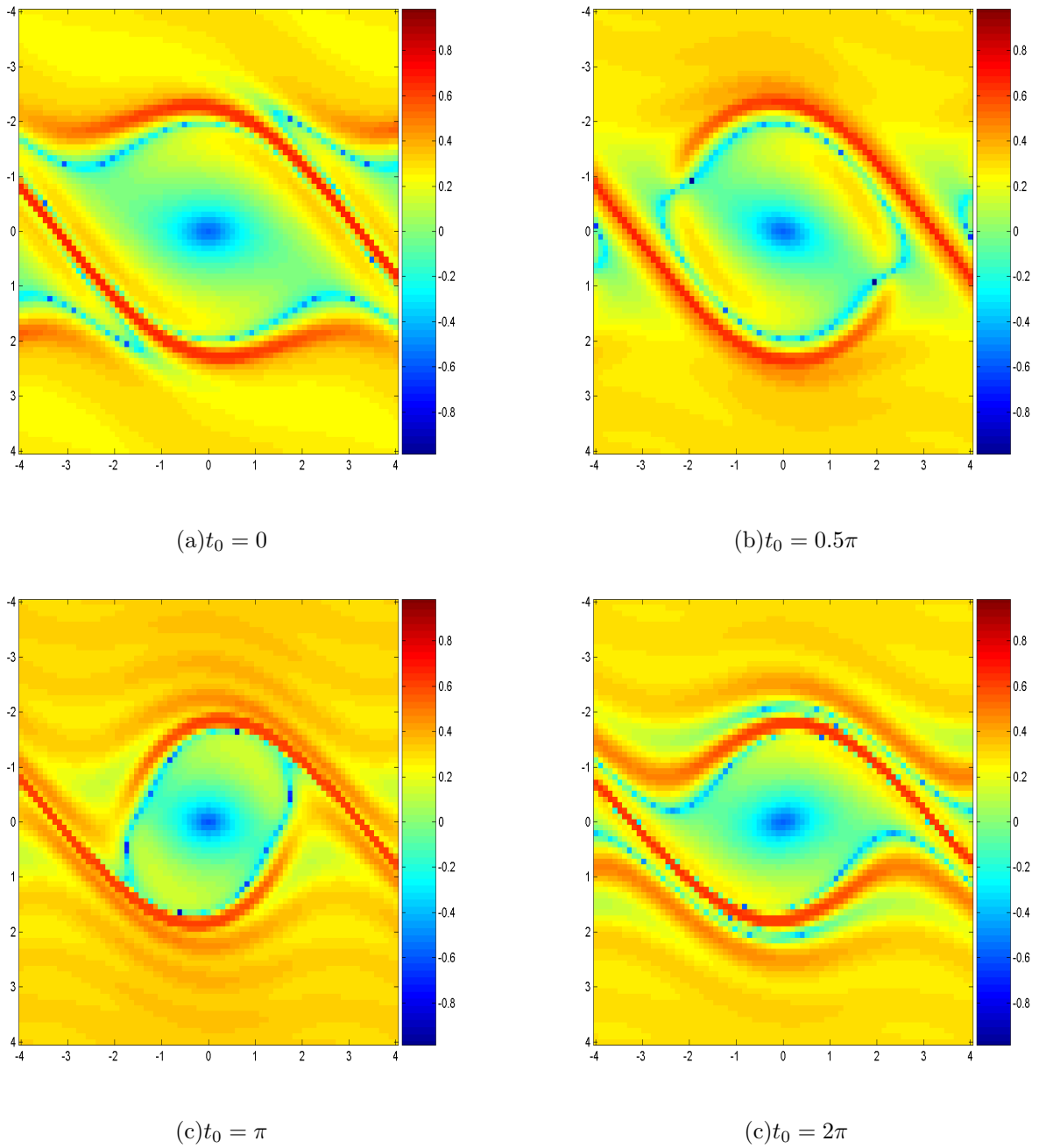
Figure 4.3: Partial FTLE σ_{xy} field for different initial times. $\epsilon = 0.1$, $\omega = 1$ and integration time, $T = 1$.

closest to the actual FTLE field σ in figure 4.1. This can be understood from the unforced and undamped pendulum equation in which the periodic trajectories move in a clockwise
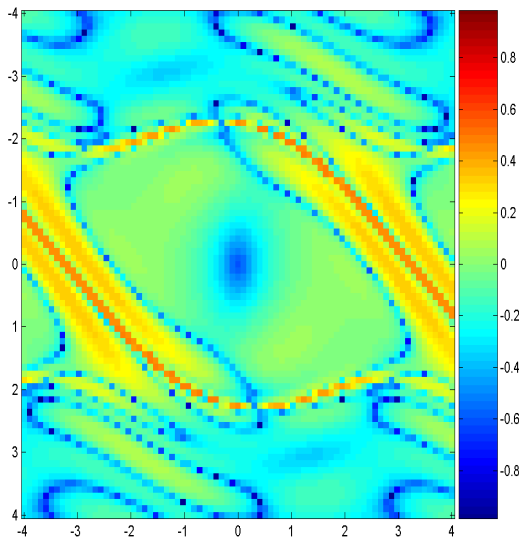
(a)$t_0 = 0$
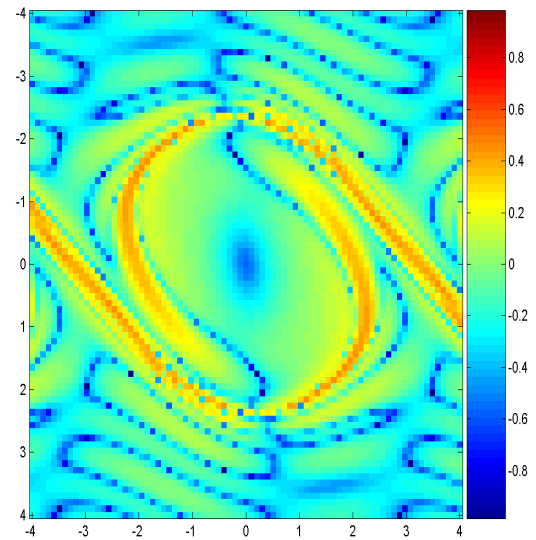
(b)$t_0 = 05\pi$
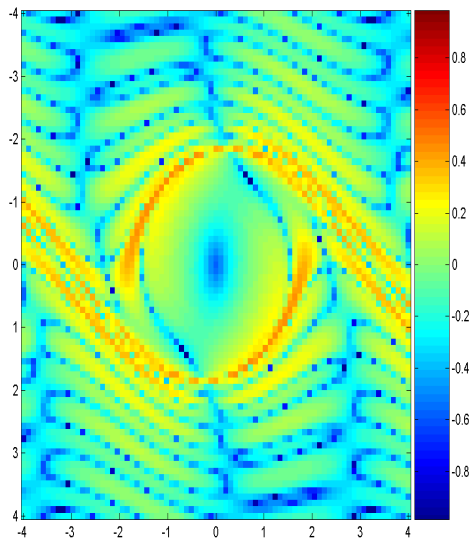
(c)$t_0 = \pi$
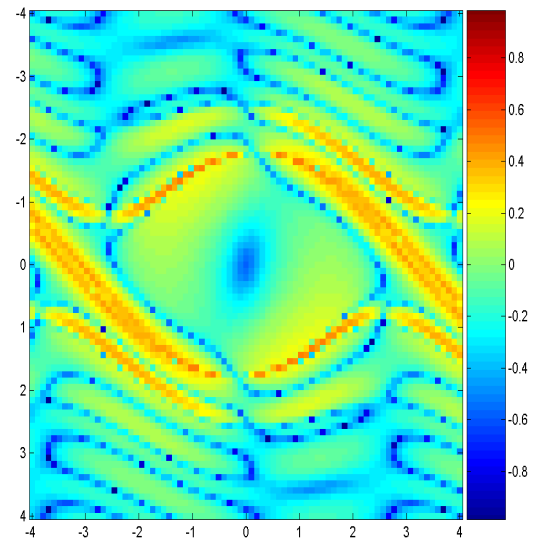
(c)$t_0 = 2\pi$

Figure 4.4: Partial FTLE σ_{yx} field for different initial times. $\epsilon = 0.1$, $\omega = 1$ and integration time, $T = 1$.

direction and the trajectories beyond the heteroclinic trajectories eventually move away to infinity in the x direction. In a neighborhood of the heteroclinic trajectory a small variation

(a)$t_0 = 0$

(b)$t_0 = 0.5\pi$

(c)$t_0 = \pi$

(c)$t_0 = 2\pi$
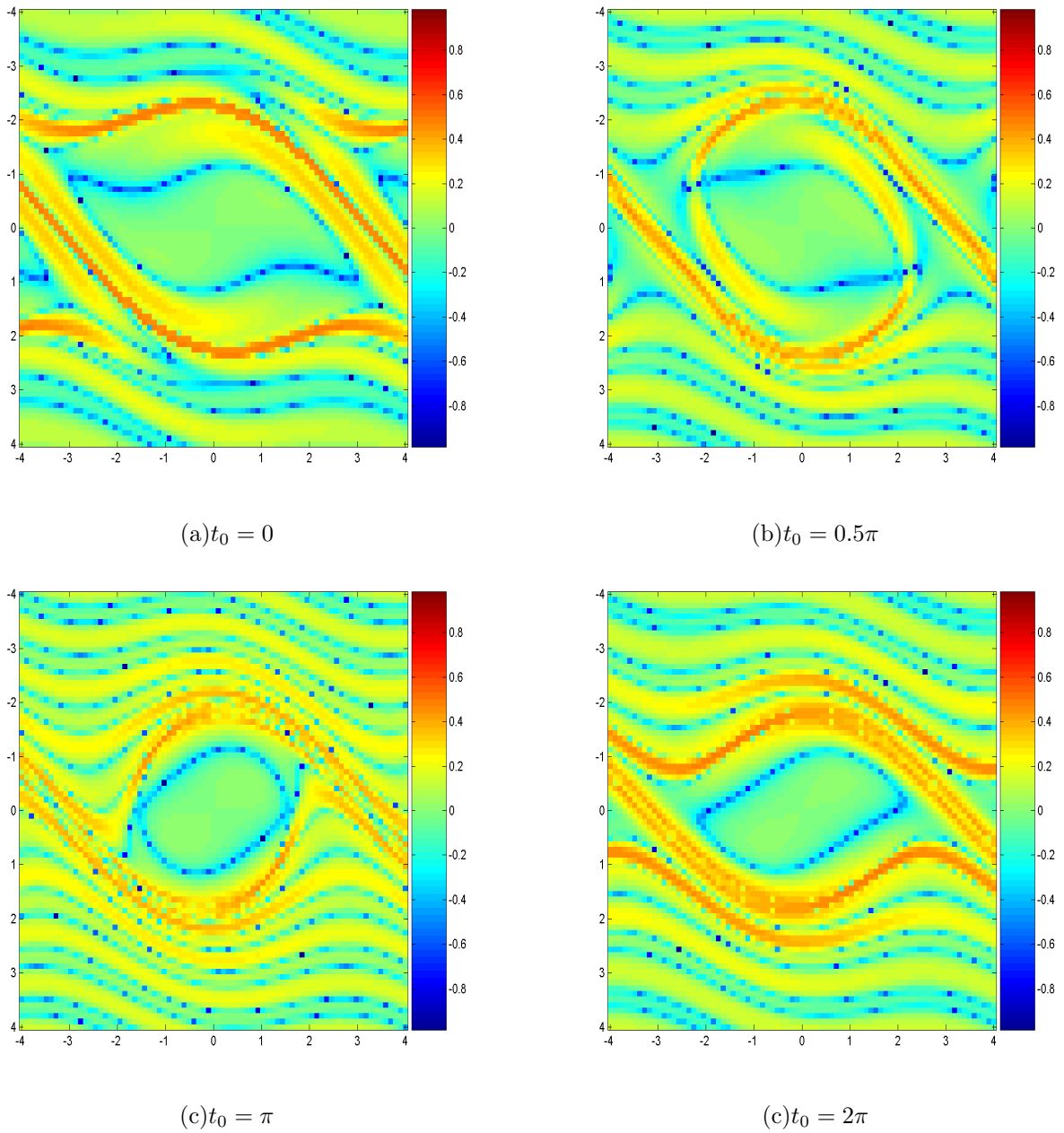
Figure 4.5: Partial FTLE σ_{yy} field for different initial times. $\epsilon = 0.1$, $\omega = 1$ and integration time, $T = 1$.

in the initial y position can either lead to a periodic trajectory or a trajectory that goes to infinity, i.e., a large variation in the final x is produced. In the case of the damped and forced pendulum, the flow does not change significantly enough in terms of the flow map. Hence

$\sigma_{x,y}$ is the closest in structure to σ.

4.3 Partial LCS from data in Rayleigh-Bénard convection

The second example we consider is a three dimensional flow described by velocity data rather than ODEs. The velocity data is from a numerical simulation of spatiotemporal chaos in Rayleigh-Bénard convection (RBC) given by the buoyancy-driven convection of a thin layer of fluid heated uniformly from below. RBC is a canonical pattern-forming system which produces important insights into the dynamics of non-equilibrium systems [48], [49], [3]. The governing equations for Rayleigh-Bénard convection are the well-known Boussinesq equations, a set of nonlinear partial differential equations which yield the fluid velocity, pressure, and temperature as a function of time. It is now possible to solve these equations numerically for convection domains with the precise conditions of experiment using a geometrically flexible and highly efficient, parallel, spectral element method, [49]. In the simulations a no-slip condition is imposed at all the walls and the lateral sidewalls are considered perfectly conducting. The data that we used in our study was generated by Paul and Tiwari [50].

The domain for the problem is a circular container of diameter 12 non dimensional units and height 1 non dimensional unit. The numerically generated data contains the velocities u, v and w at intervals of 1 non dimensional time unit. The velocities are specified on a uniform grid of size 0.1 non dimensional units. For finding the FTLE, we chose an initial grid of points that were spaced at intervals of 0.05 units in the horizontal direction and at intervals of 0.1 units in the vertical direction. We used a Runge-Kutta (RK4) algorithm to integrate the trajectories of the particles starting on this uniform grid. When particles enter the interior of a cell, we interpolated the velocity field from the nodal points of the grid. For this purpose we used a bicubic interpolation in the horizontal direction and cubic interpolation in the vertical direction. The temporal interpolation between the time units

was also cubic. We chose these specific interpolation methods to preserve smoothness of the velocity field. The total integration time was 0.1 time units.

Figure 4.6 shows the FTLE field for time, $t = 0$ at heights ranging from $z = 0.1$ to $z = 0.9$. The velocity at $z = 0$ and $z = 1.0$ is zero because of the no slip boundary condition.

(a)$z = 0.1$

(b)$z = 0.2$

(b)$z = 0.3$

(a)$z = 0.4$

(b)$z = 0.5$

(b)$z = 0.6$

(a)$z = 0.7$

(b)$z = 0.8$

(b)$z = 0.9$
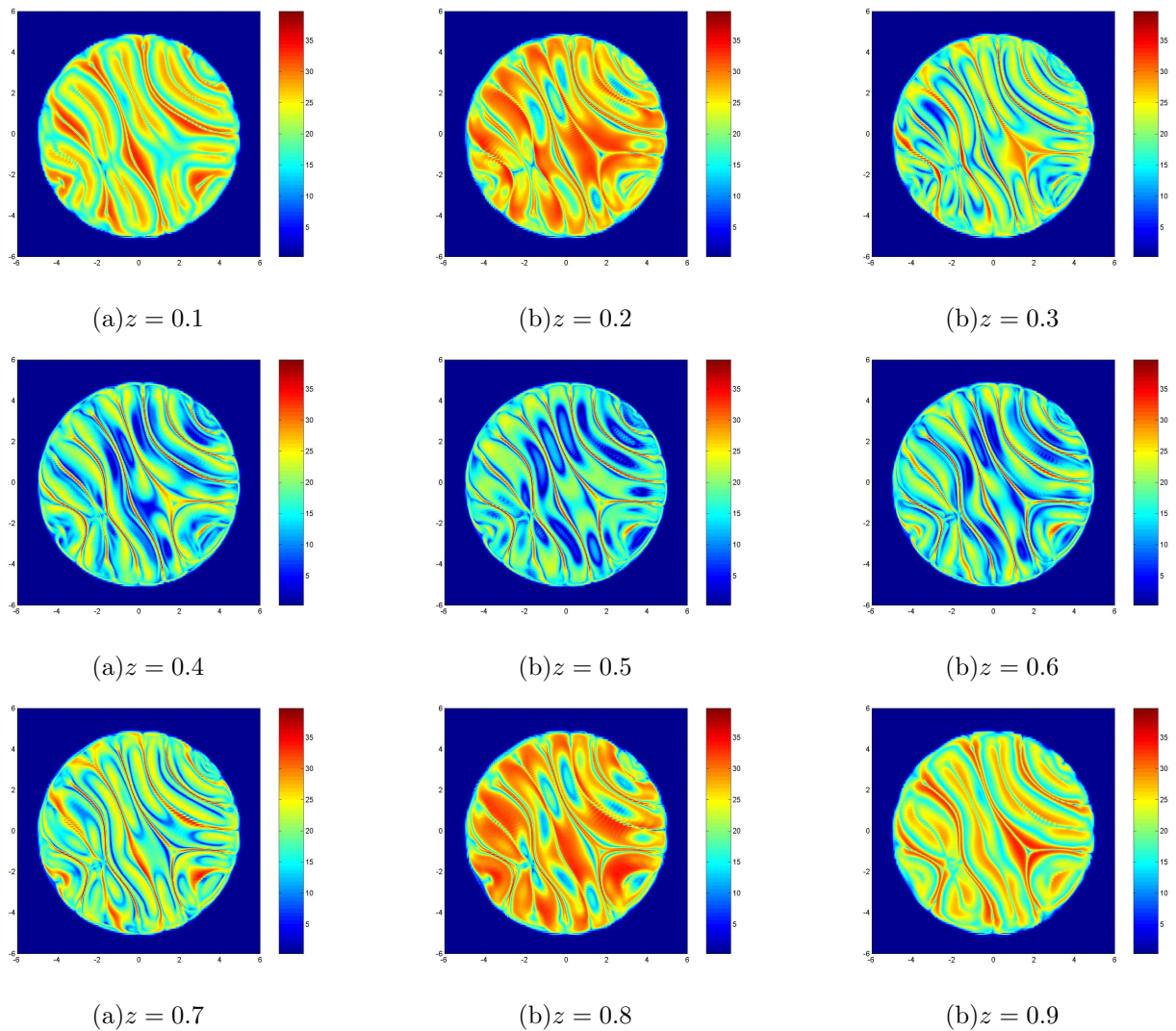
Figure 4.6: FTLE field for initial time, $t = 0$ and integration time, $T = 0.1$ plotted at height varying from 0.1 to 0.9.

Figure 4.7 suggests that transport barriers are primarily barriers to motion in the horizontal plane. We can obtain the same transport barriers by considering a 2×2 submatrix of the
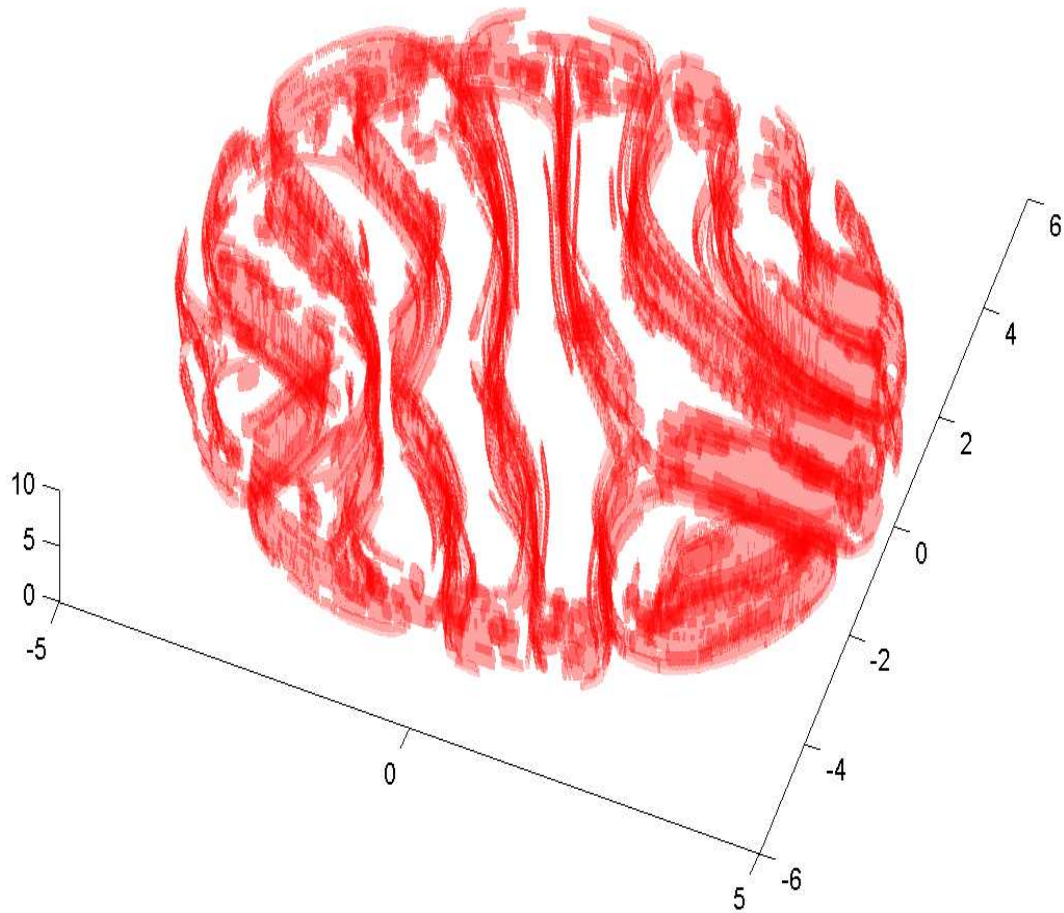
Figure 4.7: Extracted ridges from figure 4.6 form 2-dim surfaces that act as transport barriers. The z-axis is scaled 10 times in the figure.

deformation gradient. The sub-matrix of interest measures the variation in final position in the horizontal plane due to variations in initial position in the horizontal plane. The partial

deformation gradient is

$$\left(\frac{d\phi}{d\mathbf{x}}\right)_{partial} = \begin{pmatrix} \phi_{x,x} & \phi_{x,y} \\ \phi_{y,x} & \phi_{y,y} \end{pmatrix} \tag{4.15}$$

(a)$z = 0.1$ (b)$z = 0.2$ (b)$z = 0.3$

(a)$z = 0.4$ (b)$z = 0.5$ (b)$z = 0.6$

(a)$z = 0.7$ (b)$z = 0.8$ (b)$z = 0.9$
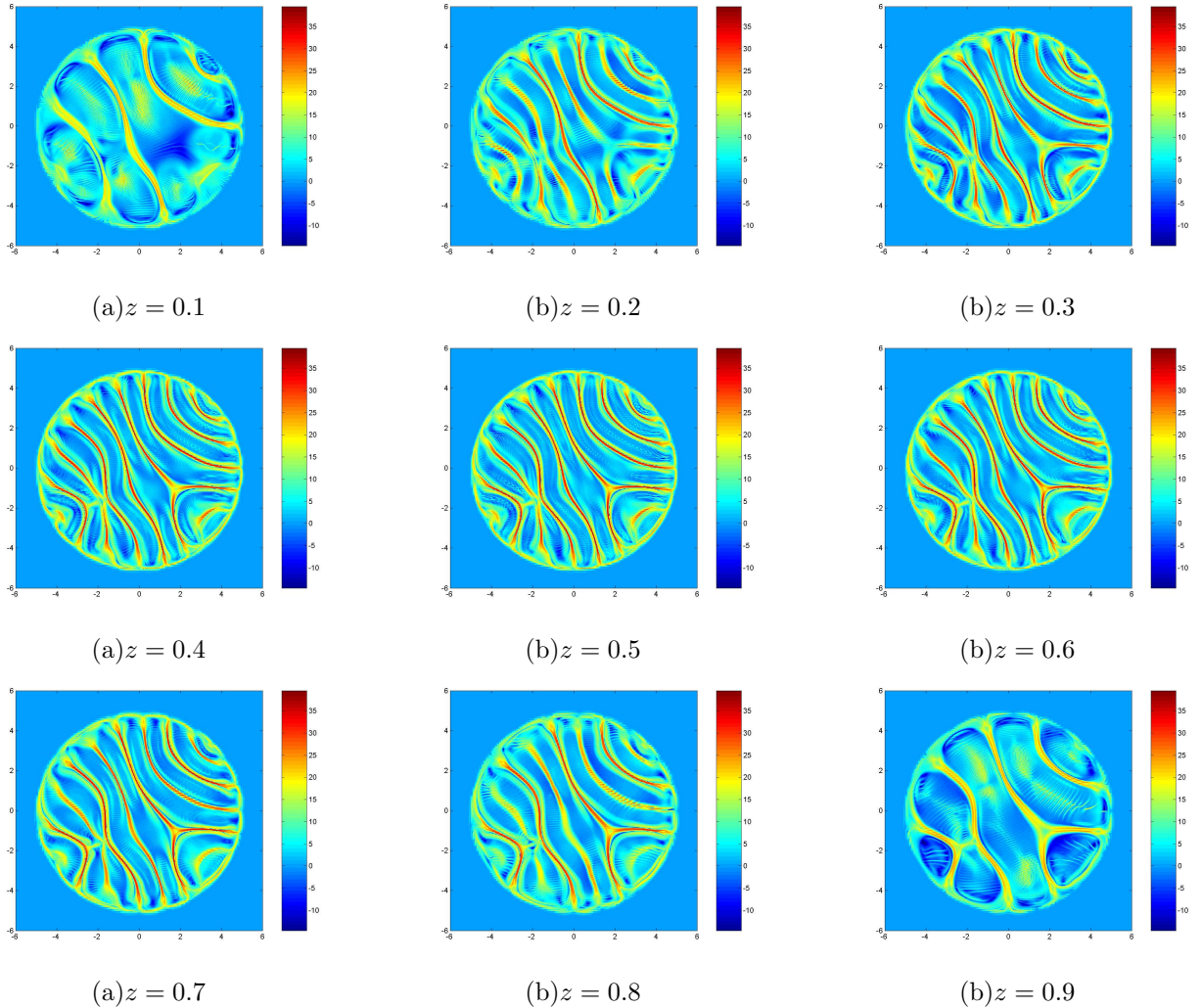
Figure 4.8: Partial FTLE field for initial time, $t = 0$ and integration time, $T = 0.1$ plotted at height varying from 0.1 to 0.9.

Comparing figures 4.8 and 4.6 suggests that the ridges in the partial FTLE field identify the transport barriers.

Chapter 5

Application of partial LCS to segregation of neutrally buoyant inertial particles in a fluid

5.1 Introduction

It is a commonly observed phenomenon that finite sized particles with inertia in an incompressible fluid do not behave as point like tracers. The motion of inertial particles can be very non trivial even in simple looking two dimensional flows. Some examples of this non trivial motion are preferential concentration, clustering and separation of particles as observed in numerous studies [64, 75, 66]. The inertial dynamics of solid particles can have important implications in natural phenomena, e.g., formation of rain clouds [21] by coalescence around dust particles and formation of plankton colonies in oceans [1]. Similarly, the inertial dynamics of reactant particles is important in chemically active flows such as coalescence type reactions [46] and mixing sensitive reactions. Inertial particle dynamics are the key to many methods of separation of particles in micro scale flows. References [34, 14],[17], [42] are a few

examples of such applications.

A study of the inertial particle dynamics from a geometric phase space point of view began in the last decade with the works of Babiano, Cartwright, Wiggins and Haller. Babiano and Cartwright rely on a simplified equation of motion of inertial particles that shows sensitive dependence of trajectories on initial conditions. They use the strain tensor of the fluid flow field to identify regions where particles could cluster. However the strain tensor of the fluid flow alone does not explain why particles that start at the same location could end up clustering in different locations of fluid. In [32] and [31] Haller used a reduced order equation for the asymptotic motion of inertial particles. The reduced order equation is a small perturbation of the ambient velocity field, with the order of perturbation being defined by the size of the particles. Attracting and repelling LCS in this perturbed flow were shown to attract or repel inertial particles. However instabilities were observed that make the particle trajectories deviate from the small perturbation approximation. In this chapter we show that the framework of transport barriers identified by LCS can explain the exponential separation of particles in a simple flow. We further show that such a framework can be used to segregate particles by size in a sample flow.

5.2 Review of the governing equations of motion of a spherical particle

The history of the equations of motion of a spherical inertial particle is rich and goes back to the works of Stokes, Basset, Boussinesq and Oseen. We start with a more recent result on the equation of motion of a spherical particle by Maxey and Riley, [45]. The full details of the derivation of the equation can be found in [45]. Here we only present a brief review of the equation to set the context for the simplified equation of motion used in [9], [32], [31] and

our work [71].The governing equation of motion of an spherical particle in a fluid is given by

$$
\begin{aligned}
\rho_p \frac{d\mathbf{v}}{dt} = {} & \rho_f \frac{D\mathbf{u}}{Dt} + (\rho_p - \rho_f)\mathbf{g} - \frac{9\nu\rho_f}{2a^2}\left(\mathbf{v} - \mathbf{u} - \frac{a^2}{6}\nabla^2\mathbf{u}\right) \\
& - \rho_f\left(\frac{d\mathbf{v}}{dt} - \frac{D}{Dt}(\mathbf{u} - \frac{a^2}{6}\nabla^2\mathbf{u})\right) \\
& - \frac{9\rho_f}{2a}\sqrt{\frac{\nu}{\pi}}\int_0^t \frac{1}{\sqrt{t^2 - \tau^2}}\frac{d}{d\tau}(\mathbf{v} - \mathbf{u} - \frac{a^2}{6}\nabla^2\mathbf{u})d\tau
\end{aligned}
\tag{5.1}
$$

where $\mathbf{v}$ is the velocity of the solid spherical particle, $\mathbf{u}$ the velocity field of the fluid, ρ_p the density of the particle, ρ_f, the density of the fluid, ν the kinematic of the viscosity of the fluid, a, the radius of the particle and $\mathbf{g}$ the acceleration due to gravity. The term on the right hand side are the force exerted by the undisturbed flow on the particle, the force of buoyancy, the Stokes drag, the added mass correction and the Basset-Boussinesq history force respectively. It is assumed that the disturbance flow due to the motion of the spherical particles is of a sufficiently low Reynolds number so that the resulting force on the sphere can be treated as due to an unsteady Stokes flow. Eq (5.1) is valid under the following restrictions.

$$
a(\mathbf{v} - \mathbf{u})/L \quad << \quad 1
\tag{5.2}
$$

$$
a/L \quad << \quad 1
$$

$$
\left(\frac{a^2}{\nu}\right)\left(\frac{U}{L}\right) \quad << \quad 1
$$

where L and U/L are the length scale and velocity gradient scale for the undisturbed fluid flow. We are interested in the case where the particles are of an intermediate size, that is they are small enough that a^2 can be neglected but large enough that a cannot be neglected. Next we assume that the relative acceleration of the particles is not very large so as to ignore the Basset-Boussinesq terms [9]. Lastly we assume that the spherical particles are neutrally buoyant, i.e $\rho_p = \rho_f$. For further simplicity we assume that the fluid flow is inviscid and two

dimensional. The resulting simplified equation is

$$\frac{d\mathbf{v}}{dt} = \frac{D\mathbf{u}}{Dt} - St^{-1}(\mathbf{v} - \mathbf{u}) - \frac{1}{2}\left(\frac{d\mathbf{v}}{dt} - \frac{D\mathbf{u}}{Dt}\right) \tag{5.3}$$

where $St = \frac{2a^2U}{9\nu L}$, is the particle Stokes number. The derivative

$$\frac{D\mathbf{u}}{Dt} = \frac{\partial\mathbf{u}}{\partial t} + (\mathbf{u} \cdot \nabla)\mathbf{u} \tag{5.4}$$

is the acceleration of a fluid particle along the fluid trajectory whereas the derivative

$$\frac{d\mathbf{v}}{dt} = \frac{\partial\mathbf{v}}{\partial t} + (\mathbf{v} \cdot \nabla)\mathbf{v} \tag{5.5}$$

is the acceleration of a solid particle along the solid particle trajectory. Strictly speaking these are not equal. We can relate them by

$$\frac{D\mathbf{u}}{Dt} = \frac{d\mathbf{u}}{dt} + (\mathbf{u} \cdot \nabla)\mathbf{u} - (\mathbf{v} \cdot \nabla)\mathbf{u} \tag{5.6}$$

Substituting (5.4) and (5.5) into (5.3), and setting $\mathbf{w} = (\mathbf{v} - \mathbf{u})$, the relative velocity of the particle with respect to the surrounding fluid, the evolution of $\mathbf{w}$ becomes

$$\frac{d\mathbf{w}}{dt} = -(J + \mu I) \cdot \mathbf{w} \tag{5.7}$$

and the change in the particle position is given by

$$\frac{d\mathbf{r}}{dt} = \mathbf{w} + \mathbf{u} \tag{5.8}$$

where J is the gradient of the undisturbed velocity field of the fluid, $\mathbf{u}$, and $\mu = \frac{2}{3}St^{-1}$ is a constant for a particle with a given Stokes number St.

Equations (5.7) and (5.8) can be rewritten as the vector field

$$\frac{d\xi}{dt} = \mathbf{F}(\xi) \tag{5.9}$$

with $\xi = (\mathbf{r}, \mathbf{w}) = (x, y, w_x, w_y) \in \mathbb{R}^4$. Eq (5.9) defines a dissipative system with constant divergence $-\frac{4}{3}\mu$. The subspace $\mathbf{w} = 0$ is a global attractor for the system for time independent flows. For general time dependent flows, it has been shown by Haller [32] that an exponentially attracting slow manifold exists for general unsteady inertial particle motion as long as the particle Stokes number is small enough. Despite the existence of a global attractor and in the case of time dependent flows, the existence of a globally attracting slow manifold, the convergence to this attractor is not exponential. There exist subsets of the domain, where a component of the relative velocity can grow. This can be seen by diagonalizing equation (5.7).

$$\frac{d\mathbf{w}_d}{dt} = \begin{pmatrix} -\lambda - \mu & 0 \\ 0 & \lambda - \mu \end{pmatrix} \cdot \mathbf{w}_d$$

$\pm\lambda$ are the eigenvalues of the Jacobian J of the fluid velocity field. The two eigenvalues add up to zero because a two dimensional inviscid fluid flow is conservative. If μ is less than λ then one component of the relative velocity grows exponentially. Even for particles of the same size (same μ) small initial differences in the relative velocity can grow exponentially if the particles visit subsets of the fluid domain where the stretching of fluid elements is high. This suggests that there exist distinguished codimension one hyperbolic sets that produce exponential separation of particles. To make the subsequent discussion more concrete we first consider a simple two dimensional flow in the next section.

5.3   Two dimensional cellular flow

We use a two dimensional incompressible cellular flow as an example to show the idea of partial LCS and transport barriers that can segregate inertial particles. Such cell flows have been studied extensively in ocean flows (the double gyre flow), and have possible applications to flows in air ducts and micro fluidic devices [69] and [70].The flow is defined by the stream function

$$\psi(x, y, t) = A \cos x \cos y \tag{5.10}$$

The velocity field is given by,

$$u = -A \cos x \sin y \tag{5.11}$$

$$v = A \sin x \cos y \tag{5.12}$$

The streamlines of the flow form a periodic array of cells within which they are concentric circles. The fixed points of the flow are $(n\pi, m\pi)$, $(\pm\pi/2, \pm\pi/2)$ where n and m are integers. The fixed points $(n\pi, m\pi)$ are centers while the fixed points $(\pm\pi/2, \pm\pi/2)$ are saddles. The heteroclinic trajectories connecting two saddle type fixed points are the fluid LCS. Stretching is higher than vorticity in a subset close to the heteroclinic trajectory will experience high stretching, the size of the subset depending on the value of A. For $A = 100$ this subset is shown in blue in figure 5.2. In this subset one component of the relative velocity of the particles can grow exponentially, a feature that can be exploited to produce trajectories sensitive to initial conditions.

5.4   Sensitivity of particle dynamics to initial relative velocity using partial LCS

The phase space for the dynamics of an inertial particle is $\mathbb{R}^4$. The flow map $\phi : \mathbb{R}^4 \times \mathbb{R} \mapsto \mathbb{R}^4$ is defined by $\phi(x(t_0), y(t_0), w_x(t_0), w_y(t_0), t) = (x(t), y(t), w_x(t), w_y(t))$. The gradient of the

flow map is a 4×4 matrix given by

$$\Phi = \begin{pmatrix} \frac{dx(t)}{dx(t_0)} & \frac{dx(t)}{dy(t_0)} & \frac{dx(t)}{dw_x(t_0)} & \frac{dx(t)}{dw_y(t_0)} \\ \frac{dy(t)}{dx(t_0)} & \frac{dy(t)}{dy(t_0)} & \frac{dy(t)}{dw_x(t_0)} & \frac{dy(t)}{dw_y(t_0)} \\ \frac{dw_x(t)}{dx(t_0)} & \frac{dw_x(t)}{dy(t_0)} & \frac{dw_x(t)}{dw_x(t_0)} & \frac{dw_x(t)}{dw_y(t_0)} \\ \frac{dw_y(t)}{dx(t_0)} & \frac{dw_y(t)}{dy(t_0)} & \frac{dw_y(t)}{dw_x(t_0)} & \frac{dw_y(t)}{dw_y(t_0)} \end{pmatrix} \quad (5.13)$$

or in a concise form as

$$\Phi = \begin{pmatrix} \phi_{\mathbf{r},\mathbf{r}} & \phi_{\mathbf{r},\mathbf{w}} \\ \phi_{\mathbf{w},\mathbf{r}} & \phi_{\mathbf{w},\mathbf{w}} \end{pmatrix} \quad (5.14)$$

However, because the system is dissipative and the global attractor is the $x - y$ subspace, initial perturbations evolve in such a way that the perturbations in the $\mathbf{w}$ subspace converge to zero. Therefore $\phi_{\mathbf{w},\mathbf{w}}$ converges to zero. If the initial perturbation in the $\mathbf{w}$ subspace is zero, then the relative velocity is always zero for a time independent flow. Therefore $\phi_{\mathbf{w},\mathbf{r}}$ is zero. $\phi_{\mathbf{r},\mathbf{r}}$ is the gradient of the fluid flow itself. The fluid flow itself has a LCS, which we term as LCS_f, which are the heteroclinic trajectories of the cell flow. So the sensitivity of the inertial particle trajectories is primarily due to the initial perturbations in the $\mathbf{w}$ subspace. The LCS for the the four dimensional flow is a 3D manifold. However since the 2×2 matrix $\phi_{\mathbf{r},\mathbf{w}}$ is enough to study the sensitivity of the inertial particle trajectories, we can restrict our attention to the LCS in the 2D subspace $\mathbf{w}$. Initial perturbations are of the form

$$\delta\xi(t_0) = [0, 0, \Delta w_x, \Delta w_y]^* \quad (5.15)$$

where $\Delta w_x, \Delta w_y$ are the perturbations in the relative velocity subspace. The evolution of the perturbation is given by

$$\delta\xi(t) = \mathbf{U}^{-1}(t_0, t) e^{(t-t_0)\sqrt{\mathbf{\Sigma}^2(t_0, t)}} \mathbf{U}(t_0, t)\delta\xi(t_0) \quad (5.16)$$

where $\mathbf{U}(t_0, t)$ is obtained from the singular value decomposition of $\mathbf{\Phi}$

$$\mathbf{\Phi} = \mathbf{U}(t_0, t_f)\mathbf{\Lambda}^{1/2}(t_0, t)\mathbf{V}(t_0, t) \tag{5.17}$$

where $\mathbf{\Lambda}(t_0, t)$ is the diagonal matrix of the eigenvalues of $\mathbf{\Phi}^*\mathbf{\Phi}$. The growth of perturbation in the xy plane is given by the first two components of $\delta\xi(t)$. One can choose a finite time, $T = (t - t_0)$, such that the evolution of the initial perturbation comes arbitrarily close to the xy plane, i.e., the last two components of $\delta\xi(t)$ approach zero. In this way the sensitivity of the final spatial location of the particles to initial relative velocity can be computed.

From the point of view of computations this means that one can work with only a 2×2 matrix $\phi_{\mathbf{r},\mathbf{w}}$ which is evaluated numerically using finite differences as

$$\phi_{\mathbf{r},\mathbf{W}} = \begin{pmatrix} \frac{x_{i,j,k+1,l}(t_0+T)-x_{i,j,k-1,l}(t_0+T)}{\Delta W_x(t_0)} & \frac{x_{i,j,k,l+1}(t_0+T)-x_{i,j,k,l-1}(t_0+T)}{\Delta W_y(t_0)} \\ \frac{y_{i,j,k+1,l}(t_0+T)-y_{i,j,k-1,l}(t_0+T)}{\Delta W_x(t_0)} & \frac{y_{i,j,k,l+1}(t_0+T)-y_{i,j,k,l-1}(t_0+T)}{\Delta W_y(t_0)} \end{pmatrix} \tag{5.18}$$

A heuristic reason is provided to justify that ridges in $\phi(\mathbf{r}, \mathbf{w})$ are partial LCS, $LCS_p = \mathbf{w} \cap LCS$. Since the eigenvalues of $\mathbf{\Phi}\mathbf{\Phi}^*$ and $\mathbf{\Phi}^*\mathbf{\Phi}$ are the same, we will use the right Cauchy Green tensor $\mathbf{\Phi}\mathbf{\Phi}^*$ writing which explicitly gives

$$\mathbf{\Phi}\mathbf{\Phi}^* = \begin{pmatrix} \phi_{\mathbf{r},\mathbf{r}}\phi_{\mathbf{r},\mathbf{r}}^* + \phi_{\mathbf{r},\mathbf{w}}\phi_{\mathbf{r},\mathbf{w}}^* & \phi_{\mathbf{r},\mathbf{r}}\phi_{\mathbf{w},\mathbf{r}}^* + \phi_{\mathbf{r},\mathbf{w}}\phi_{\mathbf{w},\mathbf{w}}^* \\ \phi_{\mathbf{w},\mathbf{r}}\phi_{\mathbf{r},\mathbf{r}}^* + \phi_{\mathbf{w},\mathbf{w}}\phi_{\mathbf{r},\mathbf{w}}^* & \phi_{\mathbf{w},\mathbf{r}}\phi_{\mathbf{w},\mathbf{r}}^* + \phi_{\mathbf{w},\mathbf{w}}\phi_{\mathbf{w},\mathbf{w}}^* \end{pmatrix} \tag{5.19}$$

But $\phi_{\mathbf{w},\mathbf{w}}$, $\phi_{\mathbf{w},\mathbf{r}}$ converge (non uniformly) to zero since $\mathbf{w} = 0$ is the global attractor.

$$\mathbf{\Phi}\mathbf{\Phi}^* \approx \begin{pmatrix} \phi_{\mathbf{r},\mathbf{r}}\phi_{\mathbf{r},\mathbf{r}}^* + \phi_{\mathbf{r},\mathbf{w}}\phi_{\mathbf{r},\mathbf{w}}^* & 0 \\ 0 & 0 \end{pmatrix} \tag{5.20}$$

The sub matrix $\phi_{\mathbf{r},\mathbf{r}}$ is zero for every $\mathbf{r} = (x, y)$, except in a small neighborhood of the LCS_f, which in our case are the heteroclinic trajectories of the cell flow. Hence $\phi_{\mathbf{r},\mathbf{w}}\phi_{\mathbf{r},\mathbf{w}}^*$ gives the partial LCS, LCS_p for $\mathbf{r}$ sufficiently far away from the heteroclinic trajectories.

Further by the smoothness of the solutions of the system (5.9) for the cell flow, varying the initial position r of the inertial particles smoothly gives the full LCS. Mathematically

$$LCS = \left(\bigcup_{\mathbf{r} \in B_1} LCS_p \right) \cup \left(\bigcup_{\mathbf{r} \in B_2} LCS \right) \tag{5.21}$$

where B_1 is the open subset in the fluid flow that excludes the LCS_f and B_2 is the interior of the complement of L_1. Then the partial particle FTLE for a finite time $T = t - t_0$ on B_1 is

$$\sigma(x, y, W_x, W_y) = \frac{1}{|T|} \ln \sqrt{\lambda_{max}(\phi_{\mathbf{r},\mathbf{w}}^* \phi_{\mathbf{r},\mathbf{w}})} \tag{5.22}$$

5.5 Partial LCS for inertial particles in the two dimensional cellular flow

We applied the computational procedure of the previous sections to the calculation of partial FTLE field specifically the partial FTLE from $\phi_{\mathbf{r},\mathbf{w}}$, to first the simple case of points starting on the heteroclinic trajectory. In this case the ridges in the FTLE field should have a symmetry about the heteroclinic trajectory. We took a grid of initial conditions in a subset of the relative velocity subspace, $(w_x, w_y) \in [-100, 100] \times [-100, 100]$ with a uniform grid size of 0.5 non dimensional units. The initial starting position is along the heteroclinic trajectory as shows in figure 5.1(a). The Stokes number of the particles is $St = 0.1$. We used the ODE45 function in Matlab to integrate equations (5.7) and (5.8).

The FTLE field for these corresponding starting positions is shown in figure 5.1(b - l). The ridges in the partial FTLE field shown in this figure are not a slice of the LCS. This is because the partial FTLE field is computed on the heteroclinic trajectory, the fluid LCS, where the final position of the particles are sensitive to variation of initial position. Nevertheless the small variations in initial velocity effectively play this role by perturbing the particle trajectories from heteroclinic trajectory. The smooth variation of the partial FTLE

(a)initial positions of particles

(b)$(x = 0, y = \pi/2)$

(b)$(x = 0.1\pi/2, y = \pi/2)$

(d)$(x = 0.2\pi/2, y = \pi/2)$

(e)$(x = 0.3\pi/2, y = \pi/2)$

(f)$(x = 0.4\pi/2, y = \pi/2)$

(g)$(x = 0.5\pi/2, y = \pi/2)$

(h)$(x = 0.6\pi/2, y = \pi/2)$

(i)$(x = 0.7\pi/2, y = \pi/2)$

(j)$(x = 0.8\pi/2, y = \pi/2)$

(k)$(x = 0.9\pi/2, y = \pi/2)$

(l)$(x = \pi/2, y = \pi/2)$
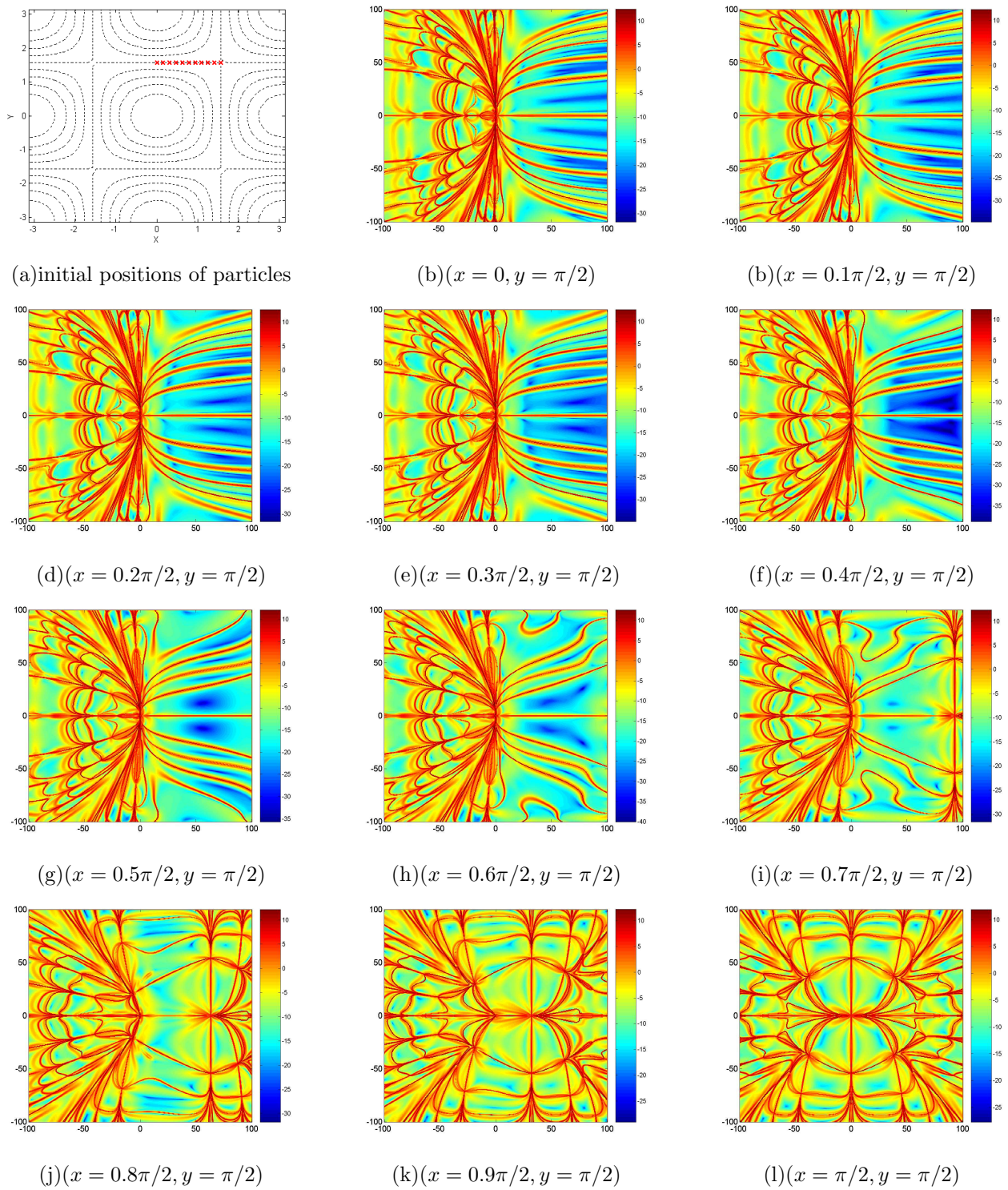
Figure 5.1: Partial FTLE field for integration time, $T = 0.48$ plotted at varying positions in the fluid domain. For (b)-(l) w_x is on the horizontal axis and w_y on the vertical axis.

field with variation in initial position along the heteroclinic trajectory shows that the partial FTLE field can be used to identify transport barriers which do not change in non smooth way with variation of initial position.

We are interested in identifying transport barriers sufficiently far away from the hetero-clinic trajectory as otherwise the sensitivity would be entirely due to transport barriers in the fluid domain itself. To this end we choose an initial starting point of $(x, y) = (3\pi/8, 3\pi/8)$ and $St = 0.1$. This point is chosen because it lies in the middle of a region of the fluid domain where the fluid flow is such that the relative velocity of the particles can grow in one direction according to equation (5.10). This region is shown in blue in figure 5.2. A sample
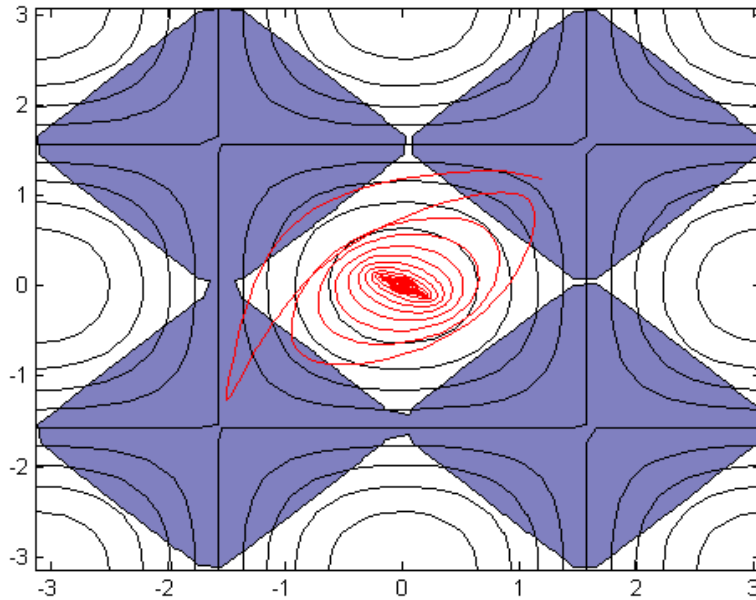
Figure 5.2: Region of instability (in blue) where perturbations in initial relative velocity can grow.

trajectory of an inertial particle of $St = 0.1$ is also shown whose initial relative velocity was $(w_x, w_y) = (-10, -10)$. The particle's trajectory cut's across streamlines as one of the components of it's initial relative velocity first grows. Eventually the relative velocity converges to zero.

Once again we chose $St = 0.2$ and a grid of initial conditions in the relative velocity subspace, $(w_x, w_y) \in [-100, 100] \times [-100, 100]$ with a uniform grid size of 0.5 non dimensional units and integration time of 0.048. The partial FTLE field is shown in figure 5.3.
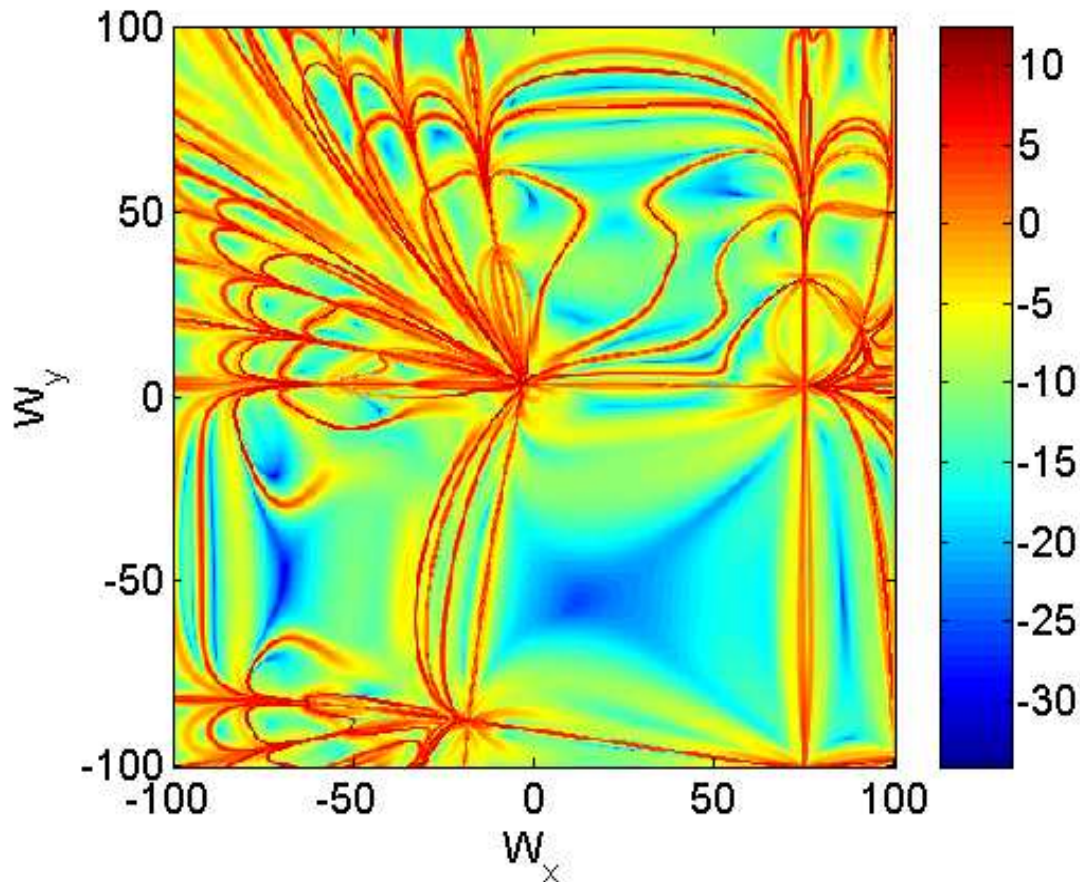
Figure 5.3: Partial FTLE field for integration time, $T = 0.48$ for $St = 0.2$.

The ridges in the partial FTLE field partition the velocity subspace into sets whose final positions in the fluid domain are significantly different. Figure 5.4 shows only the ridges in the partial FTLE field and how this partitioning works to separate particles that start at $(x, y) = (3\pi/8, 3\pi/8)$. Three sample sets in the relative velocity subspace for this purpose.
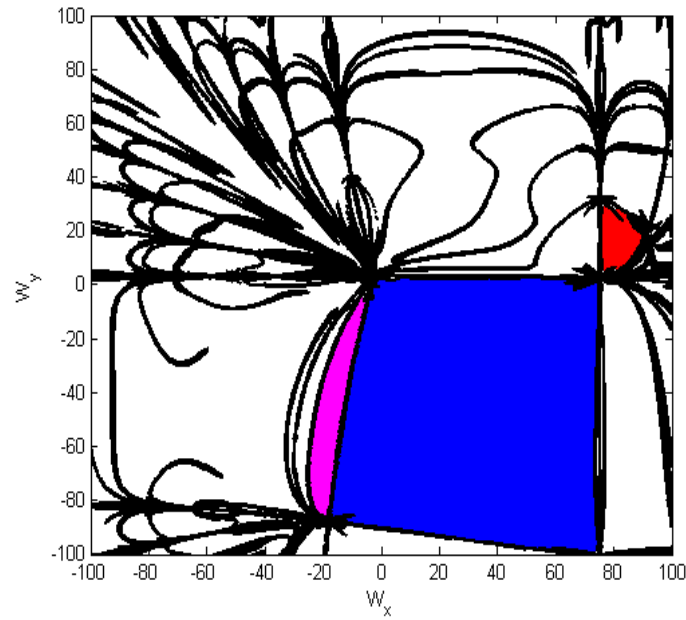
(a)Ridges of partial FTLE partition the relative velocity subspace
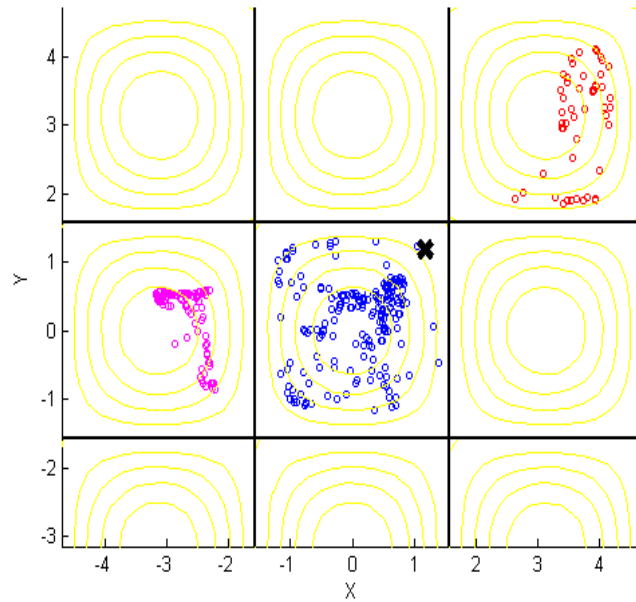
(b)Final position of particles after $T = 0.048$.

Figure 5.4: Three sample sets are chosen in partitioned relative velocity subspace. The initial position of all the particles is at $(x, y) = (3\pi/8, 3\pi/8)$, shown by a **X** in (b). The initial relative velocity of the particles belong to the sets of their respective colors in (a).

5.6 A partial FTLE framework for segregation of inertial particles by size

In the previous section we showed how the partial LCS partitions the velocity subspace into sets of distinct fates in the fluid domain, by acting as transport barriers. We seek to exploit this transport barrier property to segregate particles by Stokes number. First we observe that the partial FTLE field depends on the Stokes number via equation (5.7). Thus we can expect that the FTLE field will be different for particles of different Stokes numbers or diameters. For example the partial FTLE field for particles of $St = 0.1$ starting at $(x, y) = (3\pi/8, 3\pi/8)$ is shown in figure 5.5.
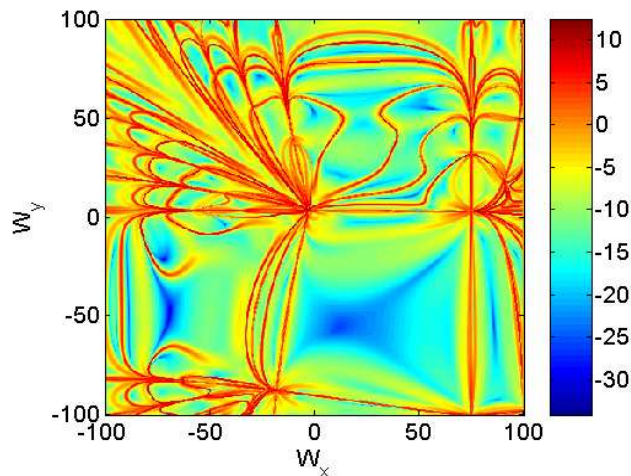
Figure 5.5: Partial FTLE field for integration time, $T = 0.48$ for $St = 0.1$.

By comparing this with the partial FTLE field for $St = 02.$, we observe that there are subsets in relative velocity subspace which are sandwiched between the ridges of the two different sized particles as shown in figure 5.6.

In particular we choose a set shown in grey subset, S_g, of the velocity subspace because it extends from close to zero relative velocity to a large magnitude of relative velocity. From the phase space partitioning property of the ridges in partial FTLE field, that was
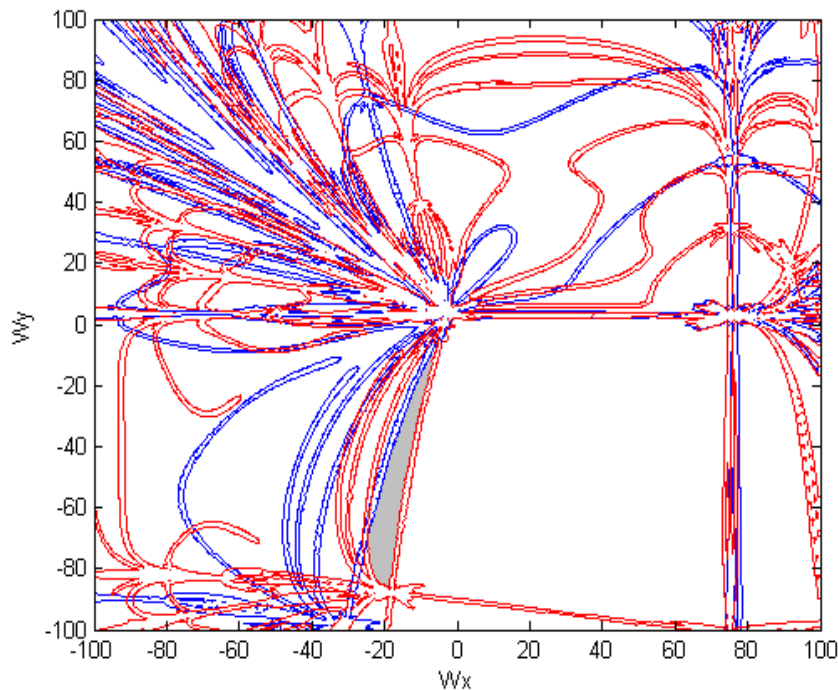
Figure 5.6: Ridges in partial FTLE field for integration time, $T = 0.48$ and initial $(x, y) = (3\pi/8, 3\pi/8)$. Blue ridges are for $St = 0.1$ and red ridges are for $St = 0.2$.

shown in section 5.5, particles with $St = 0.1$ and $St = 0.2$ whose initial relative velocities $(w_x, w_y) \in S_g$ lie in partitions of $\mathbf{w}$ whose final positions in the fluid are significantly different. We can expect that particles with $St = 0.1$ and $St = 0.2$ that start with relative velocity in S_g at the initial location $(x, y) = (3\pi/8, 3\pi/8)$, will be segregated after time $T = 0.048$. This segregation is shown in figure 5.7.

The initial relative velocity is just enough to kick the red particles into the adjacent cell, while it is not so for the blue particles. This is clearly seen in figure 5.7(b) - (c). Moreover once segregated in 5.7 (c) at $T = 0.012$ they remain segregated till $T = 0.048$ and beyond because relative velocity of most of the particles converges to zero by this time.

53

(a)$T = 0.001$

(b)$T = 0.006$

(b)$T = 0.012$

(d)$T = 0.017$

(e)$T = 0.022$

(f)$T = 0.027$

(g)$T = 0.032$

(h)$T = 0.037$

(i)$T = 0.042$

(k)$T = 0.048$
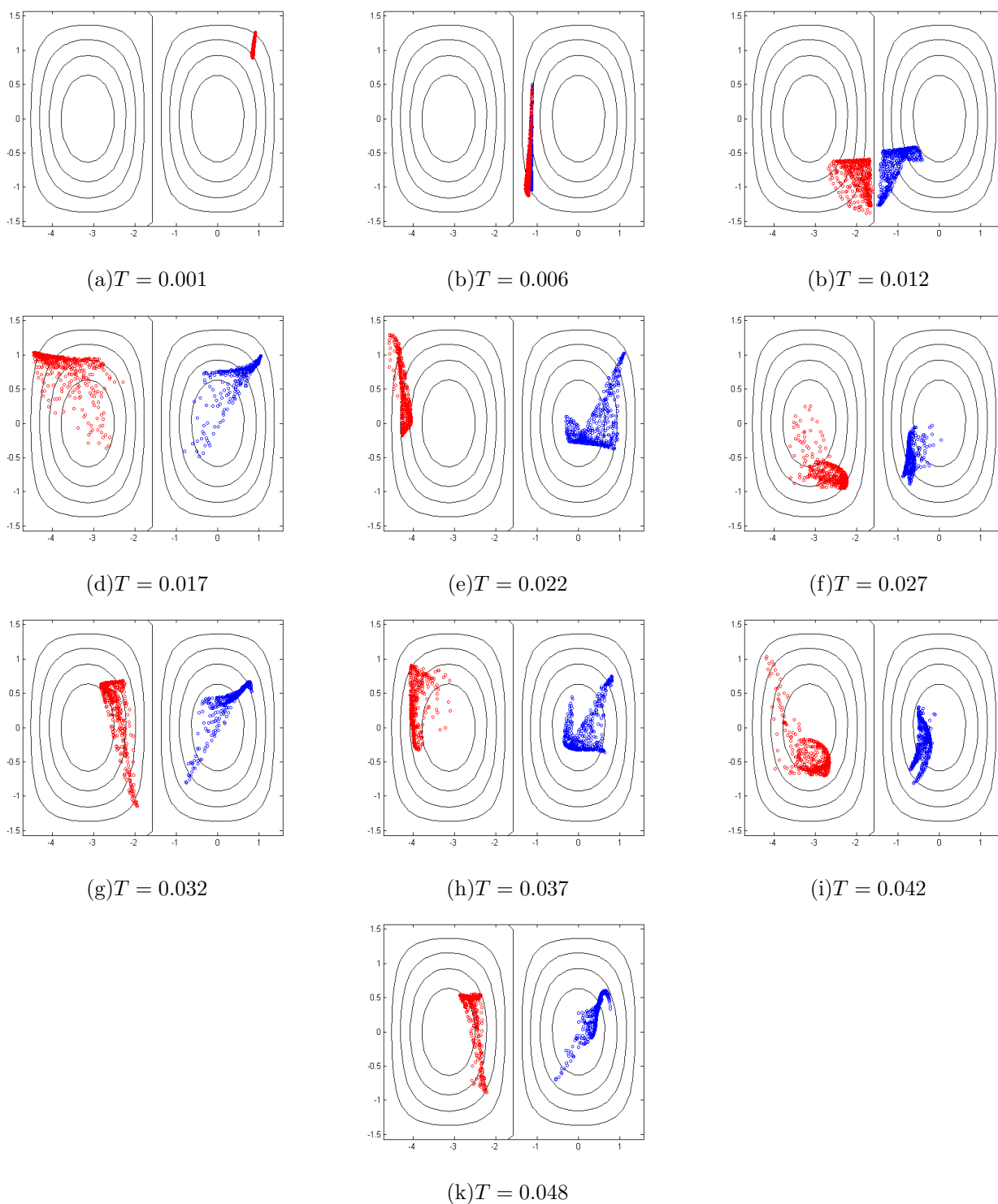
Figure 5.7: Segregation of particles by Stokes number - red particles have $St = 0.2$ and blue particles have $St = 0.1$.

5.7   Contribution to literature

The dynamics of inertial particles in a fluid flow can exhibit sensitivity to initial relative velocity. We demonstrated that ridges in the relative velocity sensitivity field at each spatial point effectively partition phase space into sets of different particle fates, i.e., inertial particles initially located on either side of a ridge will evolve to different spatial locations after a short time. The phase space location of these ridges depends on the Stokes number, and by implication the size of the inertial particles of interest. This dependence can be exploited to make particles of different sizes cluster in different regions of the fluid and thus separate and segregate them.We used this method to achieve segregation using a simple test model of two-dimensional flow: cellular flow. By injecting a mixture of inertial particles of different sizes into the fluid at a common relative velocity range that is sandwiched between the ridges of different Stokes number, the particles are segregated by size in a short time.

Though we have based our results on only cellular flow, the methodology presented only requires that the underlying flow has a (coarse) spatial partition, i.e., separatrices in the fluid flow partition the fluid domain into distinct non mixing sets. These requirements ensure that segregated particles do not remix. The method does not rely on any other flow characteristic or specific stream function. In future work, the approach employed here can be adapted to segregate non-neutrally-buoyant particles, and to segregate particles by other characteristics, e.g., density and shape, with a goal of designing flows that can fractionally separate particles for a range of inertial parameters.

Another interesting point that emerges from this chapter is that we have directly computed a partitioning of the phase space based solely on time averaged stretching in phase space, without using the stable and unstable manifolds of fixed points. This avoids the computationally expensive method of numerically generating accurate stable and unstable manifolds starting from a fixed point. This method could be used in lieu of the method of stable and unstable manifolds for nonlinear autonomous systems.

Chapter 6

Atmospheric transport barriers in the lower atmosphere - introduction and motivation

Many aerosols (e.g, spores, seeds, dust particles as well as chemical pollutants generated by human activity) can be transported across very large distances sometimes on a continental scale in the troposphere. The atmosphere serves as a medium of transport as well as a reservoir for many of these particles. Several studies show the existence of such long range transport of dust, trace chemicals and biota in the atmosphere [19] [47], [4], [52], [67], [54] and [36]. Isard and Gage [36] is an excellent resource that documents many instances of the long range transport of various plant pathogen and insects. In our work we are interested in the punctuated changes in the concentration of the spores of a genus of fungi, *Fusarium*. By punctuated changes we mean a sudden (temporal) change in the concentration at a particular location. This is explained with an example later in section 6.2. Our motivation to study this problem is to apply the concept of dynamical (moving) transport barriers that can partition the atmosphere into sets of different composition. Such transport barriers have earlier been used to study the dispersal of pollutants in Monterey Bay [12] and the splitting

of the ozone hole over Antarctica [40]. In this thesis we seek to apply the dynamical concepts outlined in earlier chapters to identify transport in the lower atmosphere and correlate them with experimental measurements of *Fusarium* collected with autonomous unmanned aerial vehicles (UAVs) performed by David Schmale's group at Virginia Tech's Kentland farm $(37°11', -80°35')$, [61] and [74].

In this chapter we provide a brief review of the process of atmospheric transport of spores, present our hypotheses on the role of atmospheric transport barriers (ATBs) in punctuated changes in concentration of spores in the lower atmosphere and provide a statistical framework to test the hypotheses concerning the puntuated changes of *Fusarium* in the atmosphere. For long range transport the large scale flow structure of the atmosphere plays a critical role as compared to short time gusts and small scale turbulence. Chapter 7 provides a review of this large scale flow and will serve as the theoretical background for the use of isobaric trajectories in our study. In chapter 8 we present our computational methodology for computing the trajectories of particles, the FTLE field and extracting the ridges in the FTLE field to identify LCS and the results of said computations. We also present the results of the statistical testing of the hypotheses on the role of ATBs in punctuated changes of spore concentrations.

6.1   Atmospheric transport of spores

The transport of plant spores can be categorized into three stages [36] - (1) emission and ascent into the planetary boundary layer (PBL), (2) long range transport in the PBL and (3) deposition of spores into a new habitat. Figure 6.1 illustrates these three stages schematically. In the first stage, that of emission and ascent, spores (or any passively moving particles) have to cross a thin boundary layer that can extend in height up to 50 m, called the surface boundary layer (SBL). The SBL is the lowest 'layer' of the atmosphere and being in contact with the ground, it has very strong vertical gradients in wind speed, temperature
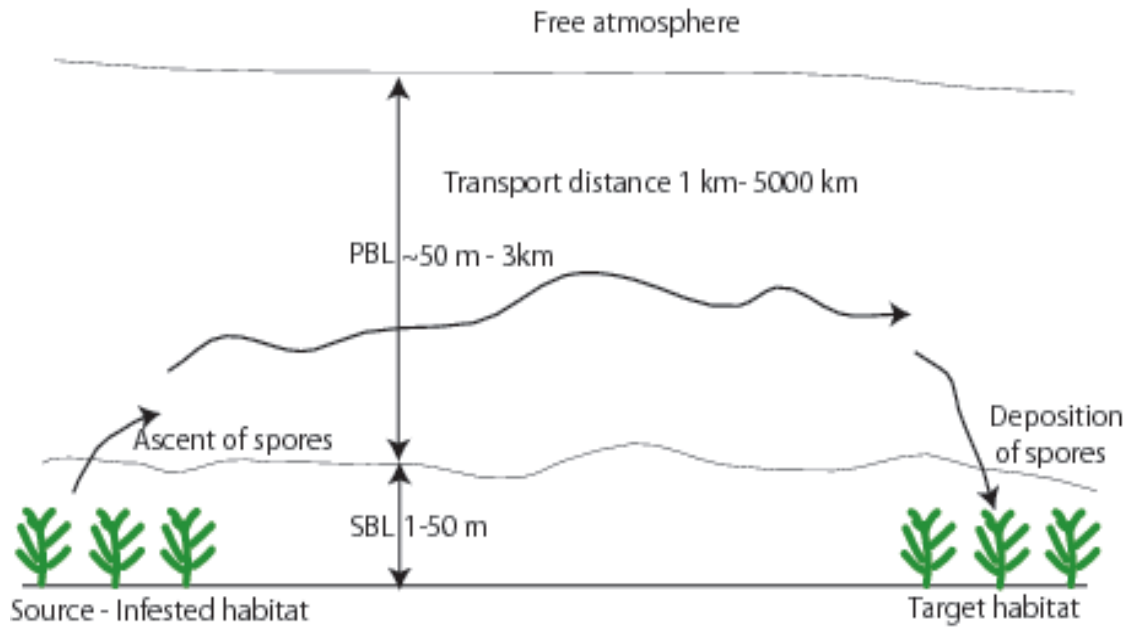
Figure 6.1: Long range transport of plant pathogen spore.

and humidity. The flow in this layer is highly turbulent because of the surface effects [82] and [33]. The motion of spores in this layer can seem random and indeed the Fokker-Planck equation is one way to describe their motion in this layer [10]. Above the SBL is the PBL, a well-mixed layer in which the turbulence due to the surface forcing decreases. The height of the PBL extends from 50m to 3 km above the ground. There is a large day-night variation in the height of the PBL, with the top of the PBL dropping to as little as 300 m during night. Some authors classify the SBL to be the lowest part of the PBL [33]. Above the PBL is the free atmosphere, where the flow of air is along constant pressure surfaces. Once spores manage to cross the SBL and enter the PBL they can be transported over long distances.

The first and third stages have received considerable attention in terms of developing computational models, for example in the works of Aylor [8], [5], [10] and Schmale [60] and [63] and other co-workers. The second stage, that of long range transport has usually been studied using a few sample trajectories [6], [15] and [27]. However, studying individual trajectories cannot explain punctuated changes in the composition of the atmosphere. Moreover,

such studies rely on arbitrarily long computations in time, which can lead to many uncertainties in trajectory computations. We propose a geometric framework of transport barriers in this chapter, a framework that utilizes short time computations of trajectories and the resulting FTLE field and verify this with experimental measurements of the fungi in the genus *Fusarium* in the atmosphere.

6.1.1 Atmospheric transport of *Fusarium*

Microbes belonging to the genus *Fusarium* were selected by the Schmale group for studying the role of ATBs in the long range atmospheric transport. *Fusarium* was chosen as a good test candidate because -

- The genus *Fusarium* is common in the atmosphere, [44].

- Many members of the genus cause important diseases in plants and animals.

- Reliable methods for collecting *Fusarium* have been developed.

- Data collected by the Schmale group using unmanned air vehicles (UAVs) has shown that the lower atmosphere is teeming with *Fusarium* [44].

Autonomous unmanned air vehicles (UAVs) were used by the Schmale group to collect colonies of *Fusarium* from the lower atmosphere (height 100 m above ground) at Kentland farm, from 2006 to March 2010. More than 100 flights were conducted. The UAVs carried collection plates containing a *Fusarium* selective medium on the wings. The collection plates were incubated in the laboratory and the colonies allowed to develop. Figure 6.2 shows one of the UAVs and collection plates after the colonies (i.e. viable spores that grew on the plates) developed. The number of colonies in the collection plates were counted and used to compute the concentration of spores in the atmosphere. All the experimental work of piloting the UAVs, collection, culturing of spores and identification of individual strains was done by Schmale's group.

(a)
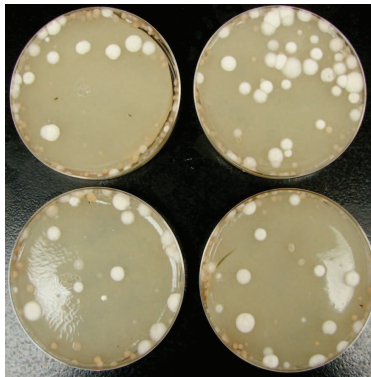
(b)

Figure 6.2: (a) UAV and (b) petri plates showing white colonies of *Fusarium* cultured from an individual sampling mission. Figures from [57].

6.1.2 Calculation of spore concentration

The spore count obtained experimentally has to be converted to a form that is independent of total flight time and flight speed. One way to do is this to obtain a spore count per unit time per unit volume sampled, which is enough for identifying punctuated changes. An alternative way is to estimate the concentration (number/volume) of the spores, which is a useful quantity in aerobiology. We use the method given in [7] and [59] to estimate the concentration of spores from the number of spores and other parameters of the flight. The UAVs used for collection of *Fusarium* were flown in a circular flight path at a nearly constant speed. Due to the circular path the relative velocity of the air with respect to the UAV is approximately the same as the speed of the UAV. This is because the upwind and downwind

contributions of the wind speed cancel each other. Let the number of spores sampled in a flight be denoted by N_p, the average air speed by U, the flight time by T_f, the radius of the petri plates on the volume of air sampled be denoted by r and the volume of air sampled by the UAV by $V = UT_f\pi r^2$, the concentration of spores by C. To obtain the concentration C from N_p and V we use the formulas given in [7] and [59] -

$$C = \frac{N_p}{E_{pp}V} \tag{6.1}$$

$$E_{pp} = \frac{0.99}{1 + 0.268S^{-1.527}} \tag{6.2}$$

where E_{pp} is the efficiency of collection of spores of the petri plates and S the Stokes number of the spores. The Stokes number of the spores is calculated using the formula $S = U\tau_R/2r$ and $\tau_R = v_s/g$ where U is the airflow speed in the free upstream approaching the sampler, τ_R the particle relaxation time, v_s the settling speed of the spores in still air and g the acceleration due to gravity. We used a value of $v_s = 1.3$ mm/s which is the average value of the experimentally determined range of settling speeds of a particular variety of *Fusarium* spores [59] that are representative of those sampled. The final concentration is converted to number of spores per 1000 m^3 of air. The concentration of the spores collected from 100 flights is shown in figure 6.3. A punctuated change in the concentration of atmospheric *Fusarium* (in general any tracer) is a high magnitude in the temporal gradient of the tracer at a particular location, i.e. a rapid change in the concentration of the tracer. The mean value of the spore concentrations shown in figure 6.3 is 1915 /1000 m^3 and the standard deviation is 4776.0 /1000 m^3. We arbitrarily define a high concentration to be 3350 spores per 1000 m^3, which is approximately the mean plus half a standard deviation. We define a punctuated change to be a change in the concentration by at least 30%. We exclude changes in concentration which are within the low concentration regime. This is because the genus *Fusarium* is relatively abundant in the atmosphere [44] and small fluctuations within the low concentration regime are possible due to small scale inhomogeneities in the atmosphere.
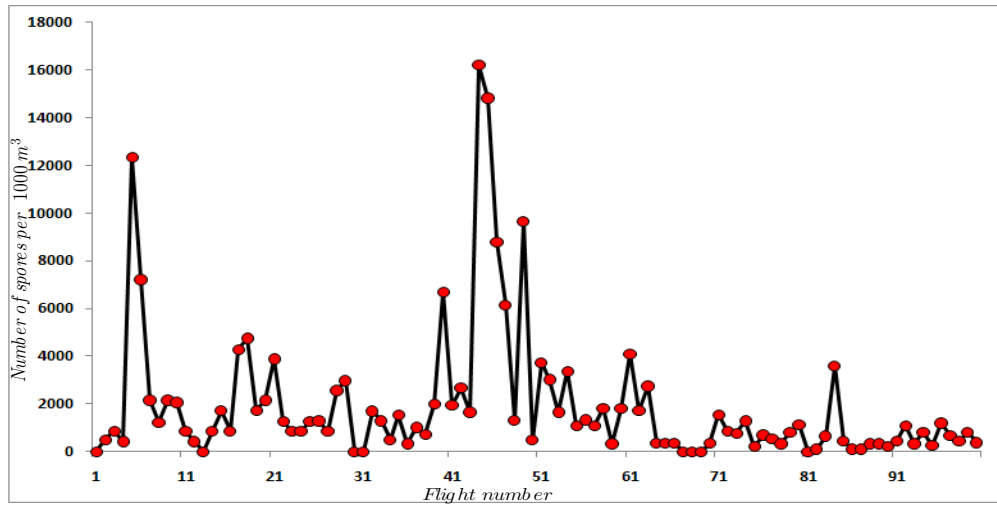
Figure 6.3: Concentration of spores (number/1000 m^3) is on the y-axis for samples from a 100 flights conducted between 2007 and 2010.

6.2 Hypotheses on the role of dynamical transport barriers in punctuated changes

An example of a punctuated change in the concentration of atmospheric *Fusarium* sampled at Kentland Farm is shown in figure 6.4. The figure shows two punctuated changes, one a rapid increase in the concentration of *Fusarium* from 30 April 2007 to the morning of 1 May 2007 and the second a rapid decline from the morning to late afternoon of 1 May 2007.

The punctuated changes in the concentration of *Fusarium* imply that we are sampling masses of air that have significantly different composition that have not mixed. We seek to explain this in terms of transport barriers.
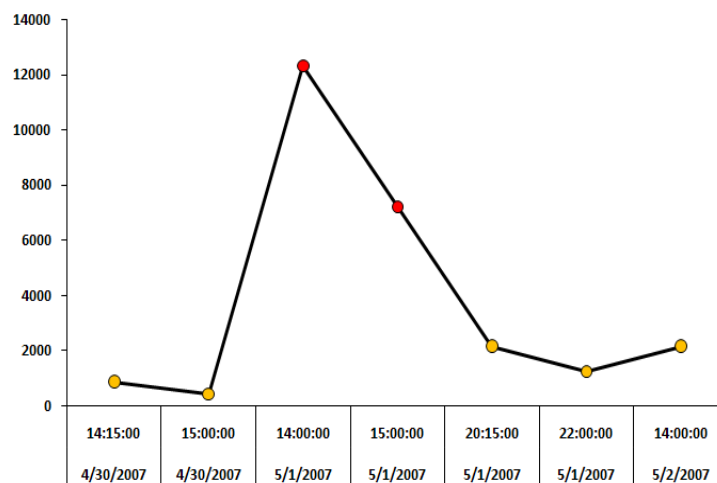
Figure 6.4: An example of a punctuated change in the concentration of atmospheric *Fusarium*. The y-axis shows the concentration of viable *Fusarium* spores in spores/m^3 and the x-axis shows the date and time in UTC. One of the samples shown in red color contained the NIV strain.

6.2.1 Punctuated changes are caused by the movement of atmospheric transport barriers

To examine the role of transport barriers we are interested in punctuated changes of the concentration *Fusarium* in the air, which are shown in figure 6.4. This sample is of particular interest. An analysis of the specific strains of *Fusarium*, observed in the two samples collected on 1 May at 14:00 and 15:00 UTC, showed the presence of a mycotoxin genotype called NIV [62]. This is a genotype that was not detected in the wheat fields of Virginia. About a thousand samples were collected from six states; Virginia, North Carolina, New York, Kentucky, Pensylvania and Maryland [58]. Of these the NIV strain was present in only some of samples from New York and North Carolina. The wheat farms at which the NIV strain was observed are hundreds of kilometers away from Blacksburg. Therefore the sample set from 29 April 2007 to 2 May 2007 presents us with a very good case of punctuated change in the atmospheric concentration of *Fusarium* that was not due to emission of spores from local farms.

We hypothesize that moving atmospheric transport barriers are responsible for the punctuated changes in the concentration of *Fusarium* in the air. The hypothesis is schematically illustrated in figure 6.5. In the figure 6.5, the red curves are atmospheric transport

(a) t_1 (b) t_2 (c) t_3
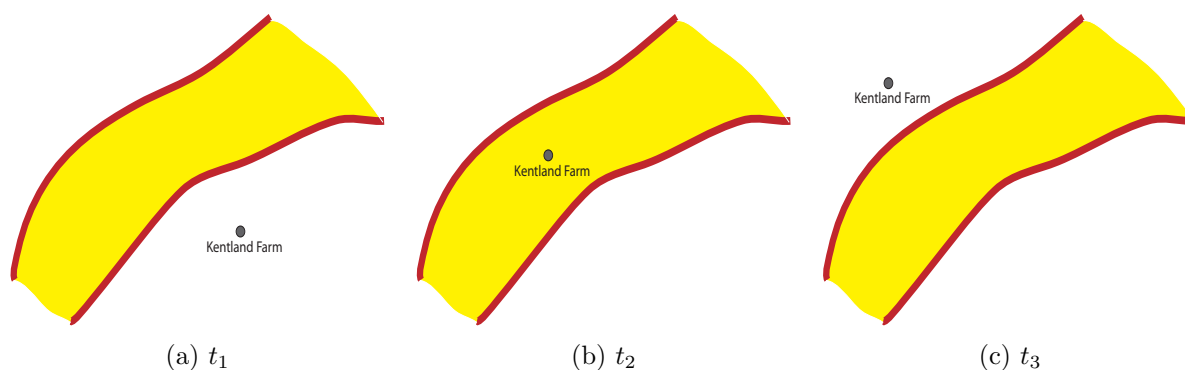
Figure 6.5: Movement of repelling ATBs with time and the punctuated changes.

barriers (repelling LCS) and the yellow colored set of air contains *Fusarium*. The (locally) repelling LCS repel the air mass around them. At time t_1, when the first sample is collected, no *Fusarium* is detected. This air is pushed away by a repelling LCS between times t_1 and t_2 and the *Fusarium* containing mass of air is sampled at time t_2. Another repelling barrier pushes away the *Fusarium* laden air mass between t_2 and t_3. At t_3 no *Fusarium* is detected in the sampled air.

Another alternative hypothesis to explain punctuated changes shown in figure 6.6 is

(a) t_1 (b) t_2 (c) t_3
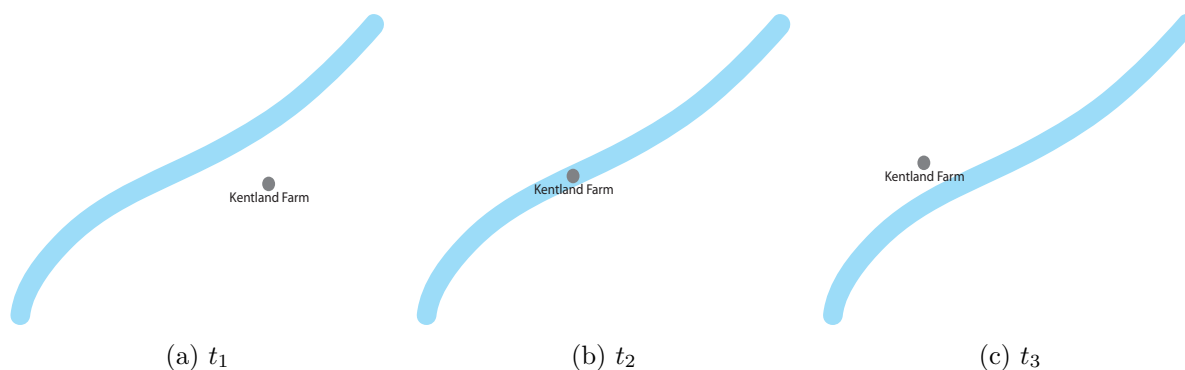
Figure 6.6: Movement of attracting ATBs with time and the punctuated changes.

using the attracting LCS. The (locally) attracting LCS acts as an atmospheric highway to which tracers stick for a long time (many days). Blobs of air get stretched along the attracting LCS quickly. Whenever the air in the attracting LCS is sampled, it has a distinct composition compared to the air on points that are on either side of it and sufficiently far from it. Thus the alternative hypothesis is that a punctuated change is caused by the passage of an attracting LCS over the sampling point.

We combine the role of the repelling and attracting LCS in one hypothesis on the punctuated changes -

Hypothesis 6.2.1. H_1 *Punctuated changes in the atmospheric concentration of Fusarium is caused by the movement of an atmospheric transport barrier (attracting or repelling LCS) over the sampling point, between the two sampling times.*

The hypothesis H_1 only says that punctuated changes imply the passage of an LCS and not the converse. The null hypothesis is -

Hypothesis 6.2.2. H_0 *Punctuated changes in the atmospheric concentration of Fusarium are NOT caused by the movement of an atmospheric transport barrier (attracting or repelling LCS) over the sampling point between the sampling time intervals.*

6.2.2 Hypothesis testing

To test the hypothesis of the previous section, we need a statistical framework of hypothesis testing. The data available is a time series of the concentration of spores against which we compute the atmospheric LCS. The representative velocity of air on the 900 mb isobaric surface is 10 m/s. The distance traveled by a parcel of air in an hour is 36 km. If the temporal spacing between the samples is very large, say a week, then a significant change in spore concentration can occur because the sampled air masses will be too far away from each other and can have very different compositions, even without the existence of any repelling transport barrier. This requires that to measure punctuated changes, we need to define a

maximum time interval over which we measure the changes in the spore concentration. We set this to be 24 hours to capture any day-night effects and because it is on the order of the time scale of motion. So if a sample is not followed by another sample in a time less than 24 hours, we cannot use it to measure punctuated changes. Out of the samples collected from 100 flights we have samples from 74 flights which satisfy this criteria. A change in concentration is considered a punctuated change if the absolute value of the change in concentration is more than a preset value $C > C_{min}$ and the percentage change in the concentration $|\Delta C/C| > r_{min}$, where r_{min} is the minimum ratio of the change in concentration to original concentration. These criteria are necessary to rule out any small spatial and temporal fluctuations in the spore concentration. Using the time series graph of the spore concentration in figure 6.3, we have set $r_{min} = 0.3$, which rules out the small changes in concentration. The criteria we used are heuristic and classify only a few concentration changes as punctuated changes. These conservative criteria are also partly necessary because of the approximations in the computation of trajectories of air parcels and the collection of aerial samples at virtually just one location.

We can categorize the change in concentrations as (1) punctuated change or (2) NOT a punctuated change. For each change in concentration, we can determine whether an atmospheric transport barrier has passed within the vicinity of the sampling point, Kentland farm, or not. Therefore our variables are categorical. A categorical variable is one for which the measurement scale consists of a set of categories [2]. In our case this set of categories consists of two values, *Yes* and *No*. Contingency tables are a good way to describe bivariate categorical data [2]. To explain the use of contingency tables and correlation we first define our variables precisely. Our random variables are ΔC_P, a punctuated change in concentration, and L, the passage of a transport barrier over Kentland farm. These variables can take the categorical values *Yes* and *No*. The correlation between the two variables can be studied by the 2×2 contingency table shown in table 6.1 The statistical correlation between the two

Table 6.1: Contingency table

	Punctuated change has occurred (ΔC_p)	
LCS passed over Kentland farm (L)	Yes	No
Yes	n_1	n_2
No	n_3	n_4

tables can be measured by the ϕ coefficient defined by

$$\phi = \frac{n_1 n_4 - n_2 n_3}{\sqrt{(n_1 + n_2)(n_3 + n_4)(n_2 + n_4)(n_1 + n_3)}} \tag{6.3}$$

if the denominator is not zero, with n's as in table 6.1. If any of the sums in the denominator of equation (6.3) is zero, then ϕ is defined to be 0, i.e., the variables are statistically independent. We use the phi-coefficient as a test of our hypothesis. If $\phi = 1$ then the two variables, the passage of LCS and punctuated changes in the concentration of atmospheric *Fusarium* are perfectly correlated. However our hypothesis $\mathbf{H_1}$ does not imply a two way correlation between the passage of LCS and punctuated changes in the concentration of *Fusarium*. Hence we do not expect the value of ϕ to be close to 1.

Besides the degree of correlation, one can glean further understanding of the two variables by two other ratios called sensitivity and specificity. If one were to use the movement of atmospheric transport barriers as a diagnostic tool to predict the occurrence of punctuated changes in atmospheric *Fusarium*, then in table 6.1, the number of true positives is n_1, the number of false positives is n_2, the number of false negatives is n_3 and the number of true negatives is n_4. The specificity s_1 is defined as

$$s_1 = \frac{n_4}{n_4 + n_2} \tag{6.4}$$

A specificity of 1 means that the LCS diagnostic test does not produce any false positives,

i.e., the test is very specific. The sensitivity s_2 of a test is defined as

$$s_2 = \frac{n_1}{n_1 + n_3} \tag{6.5}$$

A sensitivity of 1 means that the LCS diagnostic test identifies all punctuated changes in the concentration of atmospheric *Fusarium*. The results of the hypothesis testing are provided in chapter 8.

Chapter 7

Review of results from geophysical fluid dynamics

Geophysical fluid dynamics is the study of large scale naturally occurring fluid flows on Earth. The key aspect of this is *scales* of motion; only large scale motion is studied. This excludes various problems and phenomena such as river flow, small scale turbulence in the atmosphere and the upper ocean and cloud formation. The distinguishing features of geophysical fluid dynamics are rotation of the planet and stratification due to density differences. The influence of rotation and stratification leads to many peculiar phenomena but also allows various simplifications of the equations of motion.

In rapidly rotating homogenous fluids, the Coriolis force imparts vertical rigidity to the fluid. Particles in a vertical column evolve such that the vertical alignment persists over long period of time. The most famous example of this phenomena are the so called Taylor curtains; a dye released in a rotating fluid forms vertically coherent sheets or curtains. In the atmosphere such perfect vertical coherence is not observed because the rotation of the earth is not fast enough and the density of the fluid is not perfectly homogeneous. Nevertheless it is well established that vertical coherence persists for short time scales [33], [82] and [13]. Stratification arises because of density differences in the oceans and the atmosphere due

to for example warm and cold masses of air and fresh and saline waters. The gravitational force tends to vertically stack the fluid in horizontal layers of decreasing density. This vertical stacking is stable to small perturbations [43], however large perturbations that are persistent over long periods of time can cause mixing and convection. The appropriate choice of scales of motion, shows that the evolution of trajectories in the atmosphere is along isobaric surfaces along with vertical rigidity of columns of air. This is also supported by meteorological data and by some computations. The choice of scales of motion is heuristic and more of an art than a science. In what follows we reproduce a standard simplified derivation of the primitive and homogenous geostrophic equations of atmospheric flow. Much of this follows the textbooks by Cushman-Roisin and Beckers [13], Zdunkowski and Bott [82] and Majda [43]. We omit many of the rigorous proofs for the simplifications which can be found in [43].

7.1 Governing equations of motion

The governing equations of motion are mass conservation and momentum conservation. Augmented with the Coriolis force these equations lead to the Boussinesq approximation and with further simplification using scaling arguments lead to the primitive and geostrophic equations. The equations are derived in cartesian coordinates. The loss of accuracy due to the lack of curvature terms is negligible for length scales of a few hundred kilometers. Alternatively and more commonly these equations can be thought of as describing phenomena in a cartesian projection such as the Lambert conformal projection. Let x, y and z be the regular cartesian coordinates and u, v, and w be the velocities in the respective directions at a particular tangent point on the sphere. Gravity acts in the downward z direction. The angular velocity of the earth about the North-South axis is Ω, the latitude is denoted by φ and longitude by λ. A schematic representation of the coordinates is shown in figure
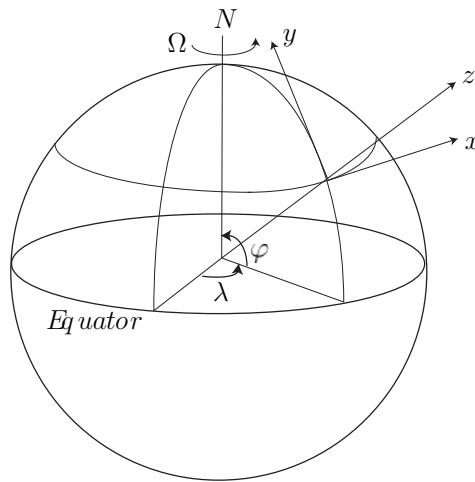
Figure 7.1: Coordinate system for the governing equations.

Mass balance gives the standard continuity equation.

$$\frac{d\rho}{dt} = \frac{\partial \rho}{\partial x} + \nabla \cdot (\rho \mathbf{v}) = 0 \tag{7.1}$$

where the vector $\mathbf{v}$ is the velocity. In local coordinates the equation is

$$\frac{\partial \rho}{\partial t} + \frac{\partial (\rho u)}{\partial x} + \frac{\partial (\rho v)}{\partial y} + \frac{\partial (\rho w)}{\partial z} = 0 \tag{7.2}$$

where ρ is the density of the fluid. Employing the usual notation of τ_{ij} for the components of the stress tensor, p for pressure and g for acceleration due to gravity, momentum conservation

augmented by the Coriolis forces leads to a modified version of the Navier Stokes equation.

$$\rho\frac{du}{dt} + (f_* w - fu) = -\frac{\partial p}{\partial x} + \frac{\partial \tau_{xx}}{\partial x} + \frac{\partial \tau_{xy}}{\partial y} + \frac{\partial \tau_{xz}}{\partial z} \tag{7.3}$$

$$\rho\frac{dv}{dt} + fu = -\frac{\partial p}{\partial y} + \frac{\partial \tau_{xy}}{\partial x} + \frac{\partial \tau_{yy}}{\partial y} + \frac{\partial \tau_{yz}}{\partial z} \tag{7.4}$$

$$\rho\frac{dw}{dt} - (f_* u) = -\frac{\partial p}{\partial z} - \rho g + \frac{\partial \tau_{xz}}{\partial x} + \frac{\partial \tau_{yz}}{\partial y} + \frac{\partial \tau_{zz}}{\partial z} \tag{7.5}$$

where $f = 2\Omega \sin \varphi$ and $f_* = 2\Omega \cos \varphi$ are the Coriolis and reciprocal Coriolis parameters respectively. Further simplification of the above equations is possible through the so called Boussinesq approximation. In the atmosphere the density of air varies from a maximum at ground height to nearly zero at very high altitudes. However most of this variation is due to hydrostatic pressure. Further within the troposphere where most of the weather phenomena and long range transport occur, the fluctuations in density are less than 5% [82]. Hence one can assume the density of the fluid can be expressed as a sum of a mean density, ρ_0 and a variation ρ_v.

$$\rho = \rho_0(x, y, z) + \rho_v(x, y, z, t) \tag{7.6}$$

with $|\rho_v| << \rho_0$. The density $\rho_0(x, y, z)$ is the temporal mean density of the air at a given point. The mean is for a time duration on the order of a day. Plugging this into the mass balance equation (7.2) we get

$$\rho_0 \left(\frac{\partial u}{\partial x} + \frac{\partial v}{\partial y} + \frac{\partial w}{\partial z} \right) + \rho_v \left(\frac{\partial u}{\partial x} + \frac{\partial v}{\partial y} + \frac{\partial w}{\partial z} \right) + \left(\frac{\partial \rho_v}{\partial t} + u\frac{\partial \rho_v}{\partial x} + v\frac{\partial \rho_v}{\partial y} + w\frac{\partial \rho_v}{\partial z} \right) = 0 \tag{7.7}$$

The spatial variations of ρ_v are much smaller than the spatial variation of the velocity which makes the third set of terms in (7.7) smaller in magnitude than those in the second set of terms. The second set of terms are much smaller than the first because of the assumption $|\rho_v| << \rho_0$. Thus the first term is the dominant one and will be the only one retained. This

converts the mass balance equation to volume conservation.

$$\rho_0 \left(\frac{\partial u}{\partial x} + \frac{\partial v}{\partial y} + \frac{\partial w}{\partial z} \right) = 0 \tag{7.8}$$

Air is a Newtonian fluid, i.e., the stress tensor and velocity gradient are linearly related. Using the index notation where $u_1 = u$, $u_2 = v$, $u_3 = w$, $x_1 = x$, $x_2 = y$ and $x_3 = z$,

$$\tau_{ij} = \mu \frac{\partial u_i}{\partial x_j} \tag{7.9}$$

In the x and y momentum equations of (7.3) neglecting ρ_v in comparison to ρ_0, using volume conservation and putting kinematic viscosity $\nu = \frac{\mu}{\rho_0}$ one obtains simplified x and y momentum equations.

$$\frac{du}{dt} + f_* w - f v = -\frac{1}{\rho_0} \frac{\partial p}{\partial x} + \nu_x \frac{\partial^2 u}{\partial x^2} + \nu_x \frac{\partial^2 u}{\partial y^2} + \nu_z \frac{\partial^2 u}{\partial z^2} \tag{7.10}$$

$$\frac{dv}{dt} + f u = -\frac{1}{\rho_0} \frac{\partial p}{\partial y} + \nu_x \frac{\partial^2 v}{\partial x^2} + \nu_x \frac{\partial^2 v}{\partial y^2} + \nu_z \frac{\partial^2 v}{\partial z^2} \tag{7.11}$$

Here the viscosity is not due to molecular motion, which on the geophysical scales is a very small number. The viscosity ν_x is the eddy viscosity in the horizontal direction and ν_z is the vertical eddy viscosity. These terms are due to the sub grid scale turbulence whose primary effect is dissipation. The difference in the horizontal and vertical eddy viscosities is due to the difference in length and velocity scales of the horizontal and vertical motion. The values of the eddy viscosity, ν_z are typically around 0.02 m^2/s while the values of ν_x are around 1 m^2/s. The horizontal viscosity ν_x in particular is susceptible to the grid size of the meteorological models and can vary significantly from one data set to another.

In the z- momentum equation ρ_v can be neglected on the left hand side of the equation, but not on the right hand side of the equation. On the right hand side after plugging $\rho = \rho_0 + \rho_v$ the term $\rho_0 g$ gives rise to hydrostatic pressure. Pressure p can be decomposed into a

hydrostatic component p_0 and a component p_v that varies around p_0.

$$p = p_0(x, y, z) + p_v(x, y, z, t) \tag{7.12}$$

$$p_0 = P_0 - \rho_0 gz \tag{7.13}$$

where P_0 is the hydrostatic pressure at the ground height. Plugging $\frac{dp_0}{dz} = -\rho_0 g$ into the z - momentum equation gives

$$\frac{dw}{dt} - f_* u = -\frac{1}{\rho_0} \frac{\partial p_v}{\partial z} - \frac{g\rho_v}{\rho_0} + \nu_x \frac{\partial^2 w}{\partial x^2} + \nu_x \frac{\partial^2 w}{\partial y^2} + \nu_z \frac{\partial^2 w}{\partial z^2} \tag{7.14}$$

Equations (7.10) and (7.14) are the so-called Boussinesq equations.

7.2   Scales of motion

The Boussinesq equations can be further simplified in the context of geophysical flows by arguments of scales of motion. Table 7.1 lists the scales of motion in the atmosphere

Table 7.1: Scales of atmospheric flows

Variable	Scale variable	Scale value
x, y	L	100 km
z	H	1 km
t	T_x, T_z	12 hours
u, v	U, V	10 m/s
w	W	0.1 m/s

The velocity and length scales are the same in both the horizontal directions. Atmospheric flows have a much bigger horizontal domain compared to vertical domain and much

larger horizontal velocities than vertical velocities. The scaling relations are stated as

$$\frac{1}{\Omega} \lesssim T_{xy} \sim T_z \tag{7.15}$$

$$\frac{H}{L} \ll 1 \tag{7.16}$$

$$\frac{U}{\Omega L} \lesssim 1 \tag{7.17}$$

$$\frac{\frac{P}{\rho_0 L}}{\Omega U} \lesssim 1 \tag{7.18}$$

$$\frac{\Omega U}{g \frac{\rho_v}{\rho_0}} \ll 1 \tag{7.19}$$

$$\frac{\frac{\nu_z U}{H^2}}{\Omega U} \lesssim 1 \tag{7.20}$$

Eq.(7.19) states that the pressure gradient is almost of the same scale as the Coriolis term. For example, the typical value of lateral pressure gradient close to the ground in mid latitudes is about 0.01 Pa/m, typical wind speeds are around 10 m/s and the mean density of air is 1.2 kg/m^3, $\frac{P}{\rho_0 L} = 8.3 \times 10^{-3}$ m/s^2 and $\Omega U = 7.28 \times 10^{-4}$ m/s^2. The next two relations can be verified by choosing some typical values of the variables, for example the eddy viscosity is $\nu_e = 10^{-2}$ m^2/s, $\rho_v = 5 \times 10^{-2}\rho$ and $g = 9.81$ m/s^2 give $\frac{\Omega U}{g \frac{\rho_v}{\rho_0}} = 1.5 \times 10^{-3}$ and $\frac{\frac{\nu_e U}{H^2}}{\Omega U} = 0.0138$.

7.3 Homogeneous Geostrophic equations

The scale relationships (7.15) - (7.20) will be used to simplify the Boussinesq equations. The z-momentum equation (7.14) in terms of the scaling variables is

$$\frac{W}{T_z} + U\frac{W}{L} + U\frac{W}{L} + W\frac{W}{H} - \Omega U = -\frac{P}{\rho_0 H} - \frac{g\rho_v}{\rho_0} + \nu_x\frac{W}{L^2} + \nu_x\frac{W}{L^2} + \nu_z\frac{W}{H^2} \tag{7.21}$$

The dominant term on the left-hand-side LHS of (7.21) is ΩU. The first term $\frac{W}{T_z}$ can be eliminated because $\frac{W}{T_z} \lesssim \Omega W$ and $W \ll U$ making $\frac{W}{T_z} \ll \Omega U$. Next $\frac{U}{L} \lesssim \Omega$ and $W \ll U$ making $U\frac{W}{L} \ll \Omega U$. Thus the second and third terms on the LHS in (7.21) are negligible

when compared to ΩU. Finally $\frac{W}{H} \sim \frac{1}{T_z} \sim \Omega$. Thus $W\frac{W}{H} \ll \Omega U$. This eliminates all the terms on the LHS of equation (7.21) except the Coriolis term. On the right-hand-side RHS of equation (7.21) $\nu_x \frac{W}{L^2} \ll \nu_z \frac{W}{H^2}$, thus eliminating the third and the fourth terms. Using equation (7.20) $\nu_z \frac{W}{H^2} \lesssim \Omega U$ and using $\Omega U \ll \frac{g\Delta\rho}{\rho_0}$ it follows that ΩU and $\nu_z \frac{W}{H^2}$ can be neglected in comparison with $\frac{g\Delta\rho}{\rho_0}$. This leaves us with hydrostatic approximation

$$-\frac{\partial p_v}{\partial z} - \rho_v g = 0 \tag{7.22}$$

This is the so called Primitive approximation in geophysical fluid dynamics. Next some non dimensional numbers are reviewed that take advantage of the scaling relationships .

The temporal Rossby number, $Ro_T = \frac{1}{\Omega T}$, is the ratio of the magnitude of acceleration to the Coriolis force. Typically $Ro_T \lesssim 1$. The Rossby number $Ro = \frac{U}{\Omega L}$, is the ratio of advection (velocity) to the Coriolis force. Typically $Ro \lesssim 1$. The Eckman number $Ek = \frac{\nu_e}{\Omega H^2}$ is the ratio of viscous forces to Coriolis force. Typically $Ek \ll 1$. For conditions where $Ro_T \ll 1$, $Ro \ll 1$ and $Ek \ll 1$ and $\rho_v \ll 1$, following similar scaling arguments as for z-momentum equation, the x and y momentum equations (7.10) and the primitive equation reduce to

$$\begin{aligned} fu &= -\frac{1}{\rho_0}\frac{\partial p}{\partial y} & \text{(7.23)} \\ -fv &= -\frac{1}{\rho_0}\frac{\partial p}{\partial x} & \text{(7.24)} \\ 0 &= -\frac{\partial p}{\partial z} \end{aligned}$$

Differentiating the second equation with respect to z and assuming the continuity of partial derivatives of p one gets

$$\frac{\partial u}{\partial z} = 0 \tag{7.25}$$

$$\frac{\partial v}{\partial z} = 0 \tag{7.26}$$

which is the so called Taylor-Proudman result. Essentially (7.25) and (7.26) say that the

atmosphere has vertical rigidity, i.e., at a particular latitude and longitude the horizontal velocity does not change significantly with altitude and each vertical column of air moves coherently. The two equations (7.23) - (7.24) imply that pressure acts as a stream function with the horizontal velocity being orthogonal to the lateral pressure gradient. Therefore isobars become streamlines and the fluid trajectories are restricted to isobaric surfaces.

The Taylor-Proudman equations (7.25) and (7.26) have some important implications to our problem of finding dynamical transport barriers in the atmosphere. The most important result is that the motion of air parcels is restricted to two dimensional isobaric surfaces. This greatly simplifies trajectory computations. Vertical rigidity means that transport barriers on a two dimensional isobaric surface can be extended vertically upwards to different isobaric surfaces. Further the transport barriers will be the same on closely spaced isobaric surfaces. This allows us to use the concept of partial FTLE and reduce the problem of computing two-dimensional transport barriers in the atmosphere to computing one dimensional transport barriers on a two dimensional isobaric surface. From now on, we treat the atmospheric flow as foliated by two-dimensional isobaric surfaces.

The derivation of (7.25) and (7.26) assumes $Ro \ll 1$ and $Ro_T \ll 1$ which is not always true. These numbers can sometimes assume values close to 1 which give rise to non zero vertical velocity. However meteorological data indicates that the vertical velocity is negligible. For example typically $w \leq 0.05$ m/s in the PBL while the horizontal velocity is about 15 m/s. This suggests that we can ignore the vertical motion almost everywhere. More importantly the vertical velocity of interest is the rate of change of pressure. This is because an isobaric pressure surface too rises and falls in height and the deviation of the vertical velocity from zero is usually due to this. The assumption of isobaric flow is also supported by meteorological data where the typical vertical velocity between isobaric surfaces is less than 0.03 Pa/s. In 24 hours an air packet can move about 26 KPa or 26 mb, roughly the difference between two pressure levels in the data provided by NOAA and described in chapter 8.

7.4 Orographic flow

One point that needs clarification is that the derivation of the homogeneous geostrophic equations (7.23) - (7.25) ignores the irregular topography of the planet and instead assumes a perfectly spherical earth. The flow over topographic barriers, called orographic flow is shown in figure 7.2. A packet of air, shown by a red circle, acquires a high vertical velocity.
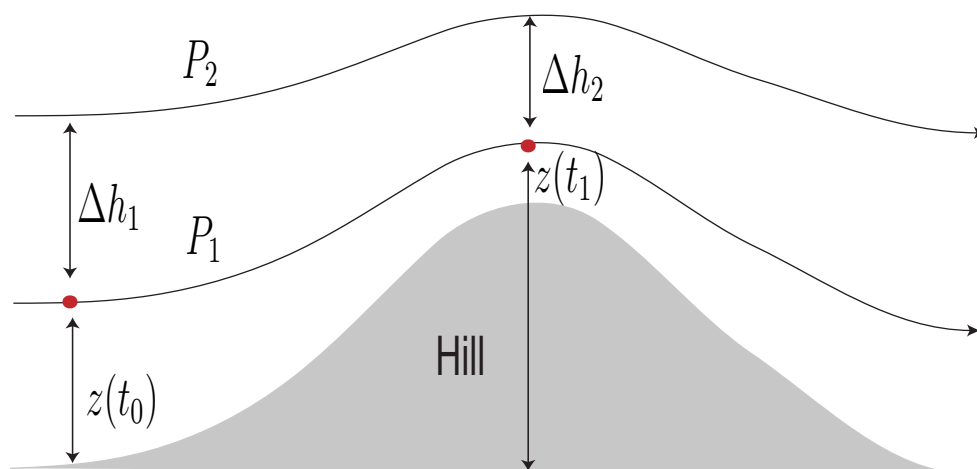
Figure 7.2: Orographic flow above a barrier.

The vertical height from the mean sea level increases from $z(t_0)$ to $z(t)$. But the isobaric surface P_1 too climbs the hill and its height from the ground increases as well. So the parcel of air still lies on the isobaric surface. The kinetic energy of an air packet determines whether the packet of air rises or flows around the barrier. If the topography rises too rapidly and to a great height, then the higher pressure surfaces that are close to the ground initially can intersect the barriers, and the flow is no longer isobaric. To avoid this pitfall we choose an isobaric surface that is always above the height of the mountains in Eastern United States, coupled with the requirement that this surface be just above the PBL, i.e., roughly 100 m - 400 m above the ground. We have chosen the 900 mb pressure surface for our computations

as it satisfies these criteria. Spores were collected by UAVs at a height of 100 m from the ground at Kentland farm, which roughly corresponds to the 900 mb pressure surface.

7.5   Role of advection and diffusion in transport

The generic combined advection diffusion of a substance whose concentration is $c(x, y, z, t)$ is given by,

$$\frac{\partial c}{\partial t} + u\frac{\partial c}{\partial x} + v\frac{\partial c}{\partial y} + w\frac{\partial c}{\partial z} = D_x\frac{\partial^2 c}{\partial x^2} + D_y\frac{\partial^2 c}{\partial y^2} + D_z\frac{\partial^2 c}{\partial z^2} \tag{7.27}$$

where D_x, D_y and D_z are the coefficients of diffusion in x, y and z directions respectively. For the atmosphere $D_x = D_y$. Using the scaling relationships (7.3), advective transport in the horizontal direction scales like $\frac{U\Delta c}{L}$ and diffusion scales like $\frac{D_x\Delta c}{L^2}$. The ratio of advective to diffusive transport is given by the Peclet number, Pe.

$$Pe_x = \frac{UL}{D_x} \tag{7.28}$$

For the atmosphere the dissipation is the strongest very close to the ground, but decreases above the PBL. The horizontal diffusion coefficient D_x is the order of ν_x and can take values between 1-10 m^2/s. This gives $Pe \geq 10^5$. In the vertical direction the ratio of vertical advection to diffusion is given by

$$Pe_z = \frac{WH}{D_z} \tag{7.29}$$

D_z is on the order of ν_z and typically has values of 0.01 m^2/s above the PBL. This gives a Peclet number of 100 in the vertical direction. For such large Peclet numbers, the role of diffusion both horizontally and vertically can be completely ignored.

Chapter 8

Computational results of ATBs using LCS

In this chapter we apply the method of FTLE and LCS to identify transport barriers. The main result of this chapter is that punctuated changes in the concentration of AFAs are governed by the movement of atmospheric transport barriers computed using the method of LCS. Our results also show that these transport barriers cannot be easily identified by just an Eulerian description such as the velocity field. Obviously there is no simple low dimensional model to describe the flow of air in the lower atmosphere. So we used meteorological data from National Oceanic and Atmospheric Administration (NOAA) to perform our computations. We begin with a brief description of the data and coordinate system of the velocity field.

8.1 Meteorological data set

Due to the growing interest in meteorological data, numerical weather prediction and climate studies, the National Climatic Data Center (NCDC), along with the National Centers for Environmental Prediction (NCEP) and the Geophysical Fluid Dynamics Labora-

tory (GFDL), initiated the National Oceanic and Atmospheric Administration (NOAA) Operational Model Archive and Distribution System (NOMADS) project. The NOMADS project utilizes observational data from radar stations, weather balloons and data from satellites as inputs for its meteorological models. The North America Mesoscale, NAM-218 gridded output data model is the most comprehensive model with data given on a grid of 614×428 points spaced at about 12.5km that covers North America. The model contains 66 variables on 42 levels in the vertical direction. The data is available at `http://nomads.ncdc.noaa.gov/data.php#hires_weather_datasets`. We are interested in the isobaric flow data, specifically the data on an isobaric surface of pressure 900 mb. As observed in chapter 7, the flow over long ranges is approximately isobaric and the 900 mb isobaric surface is a sufficient approximation to understand the flow structure in the PBL over eastern United States.

The velocity data in the NAM-218 data is given as horizontal velocity components u and v. The velocities u and v lie on a plane, given by the Lambert conformal projection, a projection method for mapping the earth to a plane. The projection method is schematically explained in the figure 8.1. The method projects the points given by their latitude and

(a) Tangent cone   (b) 'Unrolled' cone   (c) Coordinate axes
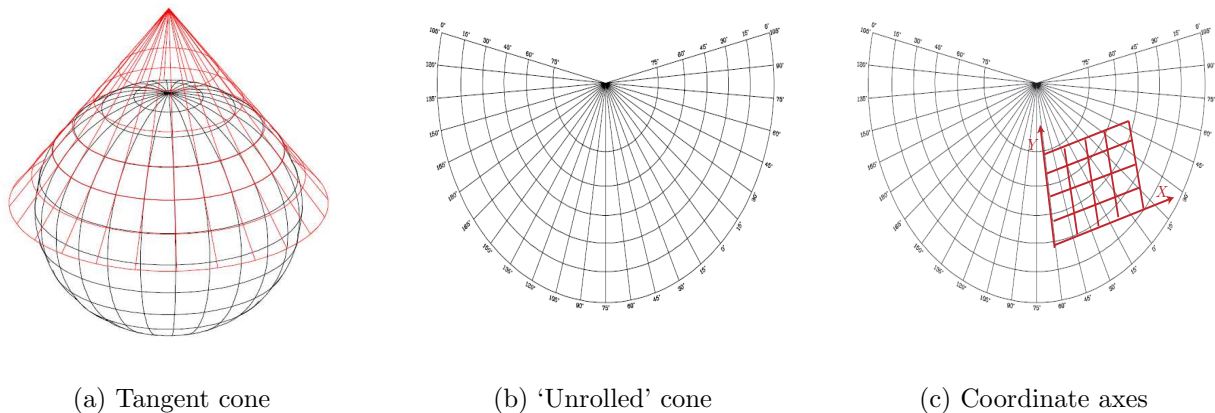
Figure 8.1: Schematic of Lambert conformal conic projection, from [72] and [73]. (a) Projection of points on the sphere to a cone tangent at a reference latitude λ_0. (b) Unrolled cone is the Euclidean domain. (c) Schematic of a coordinate frame on the the projection. The origin is at an arbitrary latitude and longitude and the axes are not parallel to latitudes and longitudes.

longitude (ϕ, λ) on the sphere (earth) to (x, y) which are coordinates parametrizing a cone that is tangent to the sphere along a specific latitude ϕ_0 using the formula, [72],

$$
\begin{aligned}
r &= R \cot \phi_0 \left(\frac{\tan \pi/4 - \phi/2}{\tan \pi/4 - \phi_0/2} \right)^{\sin \phi_0} \\
x &= r \sin \left(\sin \phi_0 (\lambda - \lambda_0) \right) \\
y &= -r \cos \left(\sin \phi_0 (\lambda - \lambda_0) \right)
\end{aligned}
\tag{8.1}
$$

where R is the radius of the earth and λ_0 is a reference longitude. The origin of the coordinates (x, y) is the apex of the cone and does not correspond to any physical latitude on the planet, with the y axis lying on the longitude given by λ_0. In the case of the NAM-218 model the latitude at which the cone is tangent is $\lambda_0 = 35°$ North of the equator and the reference longitude is $-95°$ west. We translated the origin of the coordinates for our computations to Kentland farm $(37°11', -80°35')$. The velocities remain unchanged.

8.2 Computational Method

8.2.1 Advection, FTLE computation and ridge extraction

We take an initial grid of 401×401 points with a uniform spacing of 5 km, centered on Kentland farm. These particles are advected using a RK4 algorithm with a relative tolerance of 10^{-6}. The size of the time step varies adaptively between half a minute to ten minutes. To integrate the velocities and find the trajectories, we need a smoothly defined velocity field. The velocity data we have is defined only every 3 hours and at discrete points spaced at 12.5 km intervals. Therefore we interpolate the data both temporally and spatially. To this end we use a bicubic interpolation spatially to find the velocity in the interior of a cell defined by the NAM-218 data grid points and a cubic interpolation temporally to find the velocity between the 3 hour intervals. We used these specific interpolation methods since they produce a continuous and smooth velocity field while a linear interpolation may not

produce a smooth velocity field. Bicubic and tricubic interpolation methods have been used in earlier works by Lekien and others [39] [12] [65].

An integration time of 24 hours was chosen. We chose this for two reasons; (1) to satisfy the thumb rule of the scales of motion in table 7.1; and (2) to account for the effects of the day-night cycle in the velocity field. The FTLE field $\sigma(x, y)$ obtained by advecting particles for 24 hours will rule out any influence of a day-night cycle. The FTLE field is obtained by finite differences described in section 3.2. Technically this is a partial FTLE field since we are ignoring any sensitivity to variation of initial height of particles. However due to the vertical rigidity of the atmospheric flow, we are ignoring this sensitivity to height. In section 8.3.2 we show some results of FTLE computations on different isobaric surfaces to demonstrate the validity of our assumption of isobaric flow and vertical rigidity. Figure 8.2 shows a sample FTLE field obtained for particles starting at 21:00 UTC, on 15 May 2007 and integrated for 24 hours on a 900 mb pressure surface. The regions of high FTLE are shown in red. The ridges in the FTLE field in this case cannot be obtained by just setting a threshold for the value of σ. Moreover the FTLE field has many small ridges which are not significant as transport barriers on large spatial scales. To overcome these issues, we used a heuristic
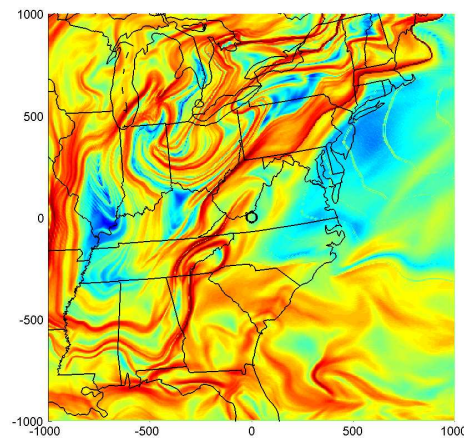
Figure 8.2: Sample FTLE field. The x- and y-axis are in kilometers with the origin centered on Kentland Farm, shown by a circle in the center of the figure.

algorithm that uses the definition of ridges from section 3.3.1. Assuming that the principal curvatures at every point in the FTLE field are given by $\kappa_1(x, y)$ and $\kappa_2(x, y)$ with $\kappa_1 > \kappa_2$, we used three criteria to determine if a point (x, y) in the FTLE field lies on a ridge.

- $\sigma(x, y) \geq \sigma_{min} > 0$

- $\kappa_1(x, y) + \kappa_2(x, y) < 0$

- $\kappa_2(x, y) < \kappa_{2max} < 0$

For a ridge that looks like figure 3.5(c), the second condition says that the mean curvature should be negative, i.e., the saddle surface should be more concave than convex. We used $\sigma_{min} =0.04$/hr and $\kappa_{2max} = -0.001$. For the chosen minimum $\sigma_{min} =0.04$/hr, a line element would be stretched to a length of ≈ 13 km which is about the grid spacing of the NAM data set. As an example, we applied the heuristic criteria on ridge curvature and height to the sample FTLE field shown in 8.2 to extract the FTLE ridges as shown in 8.3.
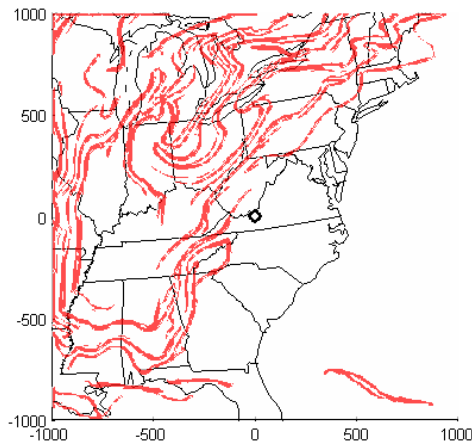
Figure 8.3: Ridges extracted from the sample FTLE field shown in figure 8.2.

8.3   Atmospheric LCS results

We first demonstrate that the atmospheric LCS indeed act as transport barriers. We take two sample sets (green and black colored sets) shown in figure 8.5 on either side of a repelling LCS and integrate them forward for 24 hours and plot their positions every 3 hours.
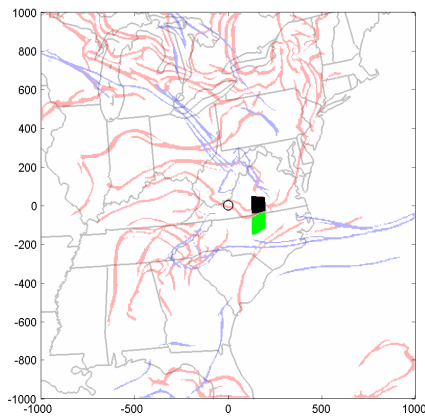
(a) 12:00 May 1st 2007
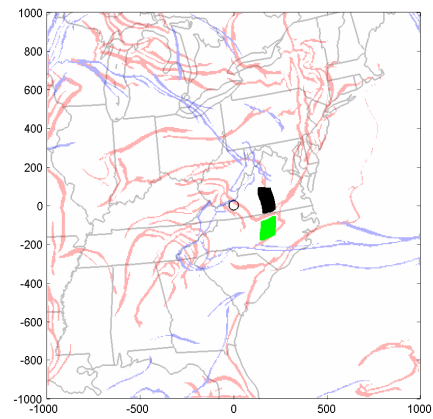
(b) 15:00 May 1st 2007
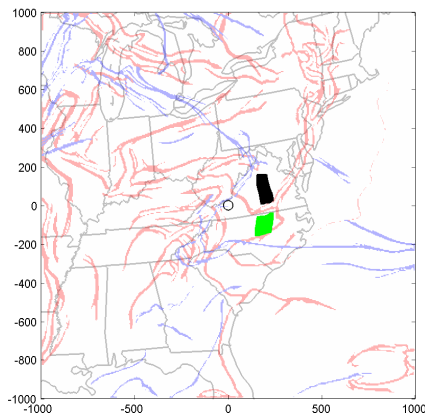
(c) 18:00 May 1st 2007
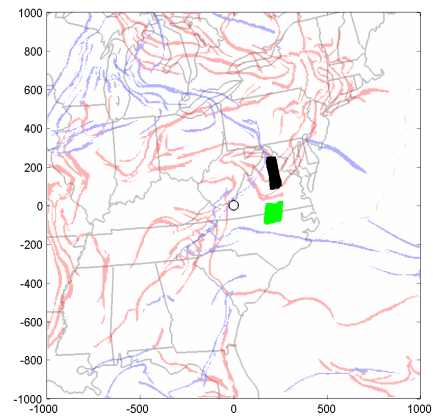
(d) 21:00 May 1st 2007

Figure 8.4: LCS act as transport barriers. Repelling LCS are in red and attracting LCS are in blue.
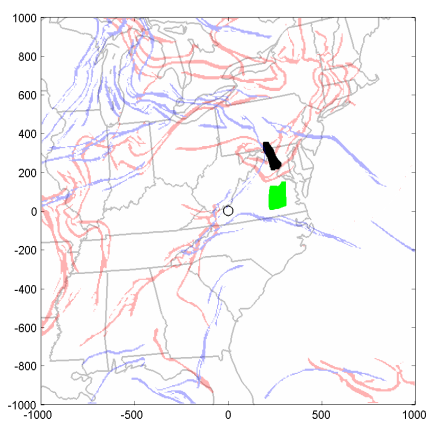
(e) 00:00 May 2nd 2007
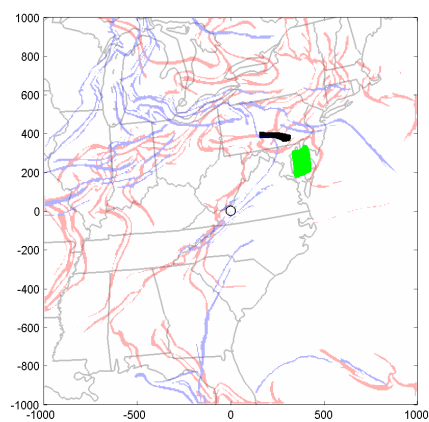
(f) 03:00 May 2nd 2007
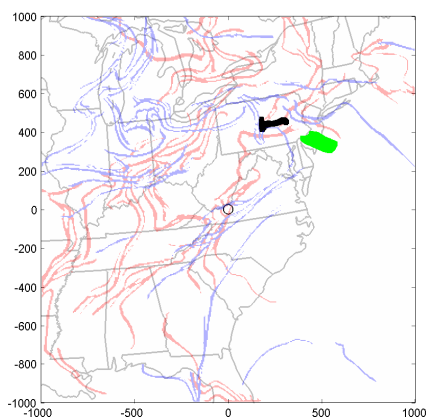
(g) 06:00 May 2nd 2007
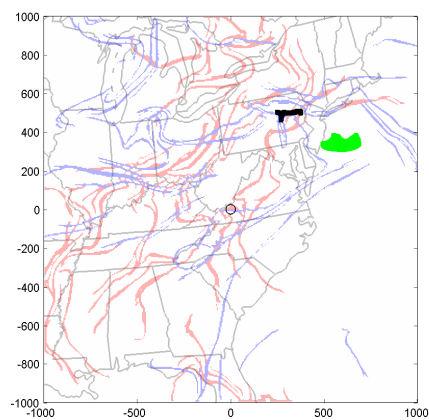
(h) 09:00 May 2nd 2007
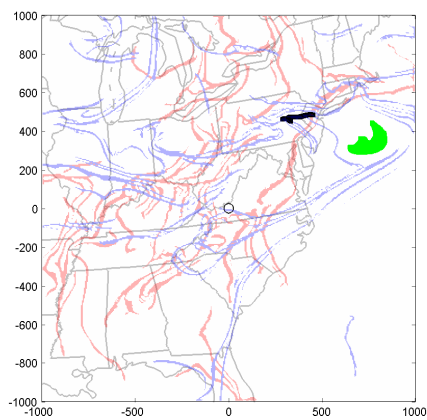
(i) 12:00 May 2nd 2007

Figure 8.5: LCS act as transport barriers. Repelling LCS are in red and attracting LCS are in blue.

The black and the green sets are repelled from each other by (red) repelling LCS. The black set encounters an attracting LCS (blue) in figure 8.5 (f) and gets stretched along the attracting LCS. The attracting LCS now acts as a pipeline that carries the black set. The area of the black set seems to decrease significantly, indicating that the height between consecutive isobaric surfaces is increasing.

8.3.1 Atmospheric LCS and punctuated change in AFAs on May 1st 2007

We computed the repelling and attracting LCS on a 900 mb pressure surface for more than 200 initial instants of time. Of these, 74 computations correspond to times when samples were collected to measure changes in atmospheric concentration of *Fusarium*. We show only some representative and important images of these LCS computations. However all the computational results are used in the hypothesis testing to determine the relationship of atmospheric transport barriers to punctuated changes in the atmosphere. The LCS results for the punctuated changes on 1 May 2007 are shown first. The time series graph of spore concentration for this time period shown initially in chapter 6, is repeated here in figure 8.6.
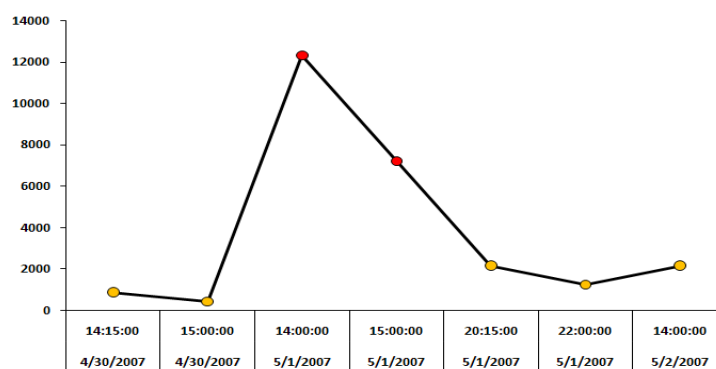
Figure 8.6: An example of a punctuated change in the concentration of atmospheric *Fusarium*. The y-axis shows the concentration of viable *Fusarium* spores in spores/1000m^3 and the x-axis shows the date and time in UTC.
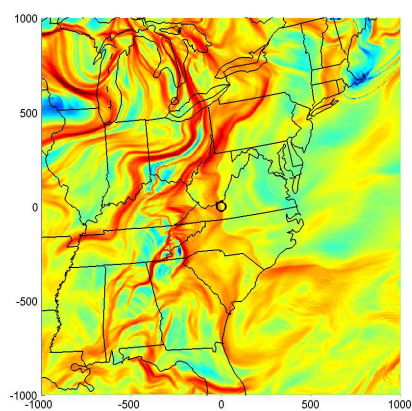
(a) 15:00 30 April 2007
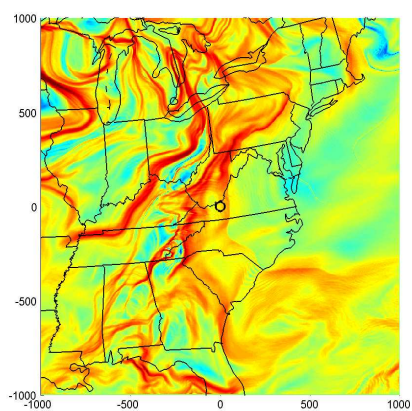
(b) 18:00 30 April 2007
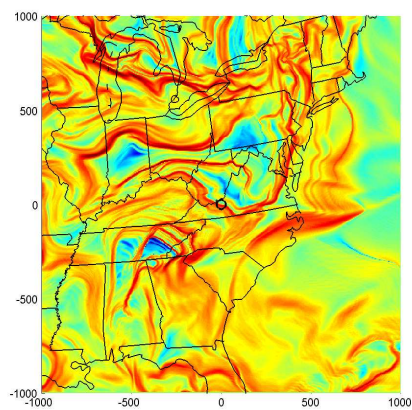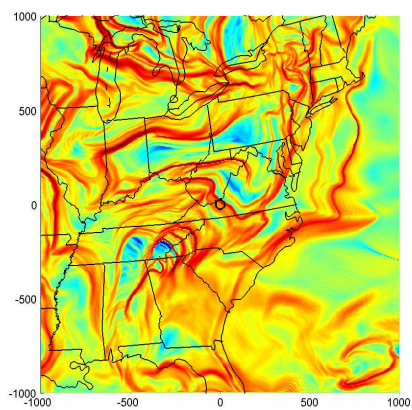
(c) 12:00 1 May 2007
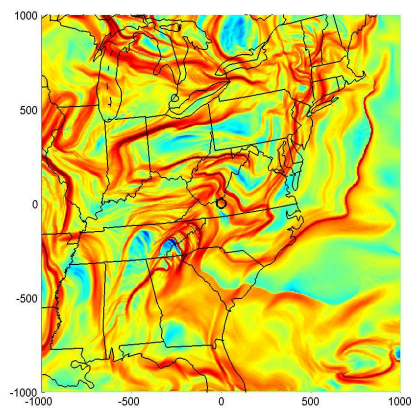
(d) 15:00 1 May 2007

(e) 18:00 1 May 2007
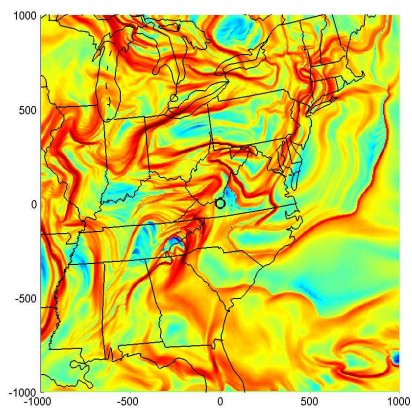
(f) 21:00 1 May 2007

Figure 8.7: Forward time FTLE field. Red indicates regions of high stretching and blue indicates regions of low stretching.

Figure 8.7 shows the forward time FTLE field for an integration period of 24 hours and initial instants of time shown in the figures. The black circle is of radius 25 km centered Kentland Farm. For the first two samples collected on 30th April, the samples were collected from one side (eastern side) of a repelling LCS in 8.7(a) and (b). The repelling LCS pushes away the low spore concentration air. The air containing a high concentration of spores which was sampled at 14:00 and 15:00 hours on 1 May 2007, is pushed away by another repelling LCS in figures 8.7(e) and (f). The movement of repelling LCS caused first a steep rise in the spore concentration, quickly followed by a steep fall; two punctuated changes.

Figures 8.8 and 8.9 show the backward time FTLE field. The red sets are attracting sets in forward time. It is seen that the punctuated changes in the spore concentration are associated with the passage of the attracting LCS as well around Kentland farm.

(a) 15:00 30 April 2007   (b) 18:00 30 April 2007
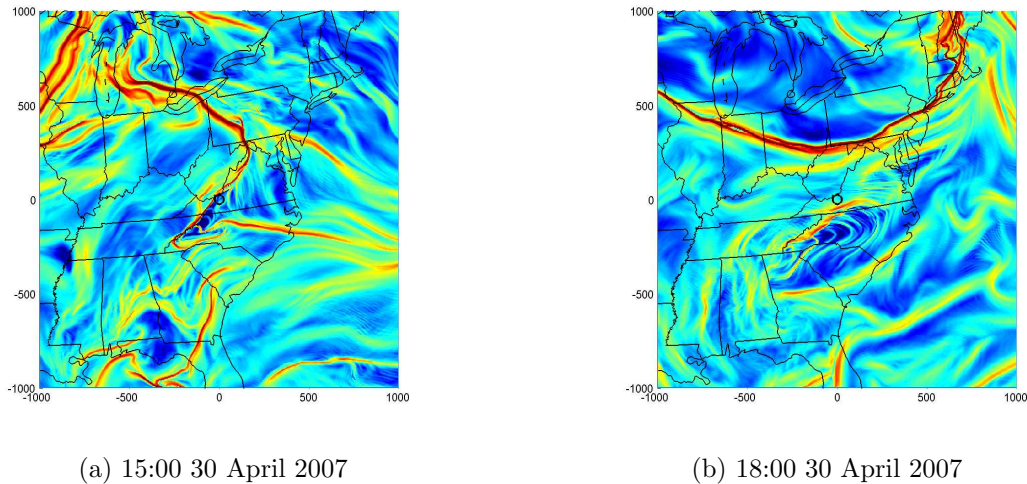
Figure 8.8: Backward time FTLE field. Red indicates regions of high contraction and blue indicates regions of low contraction in forward time.
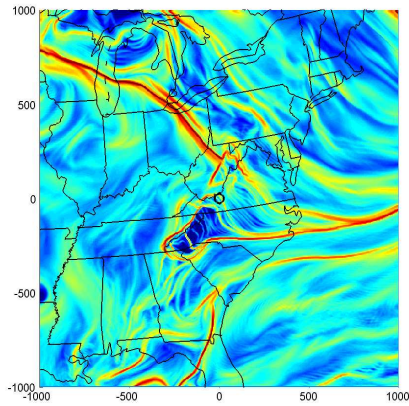
(a) 12:00 1 May 2007
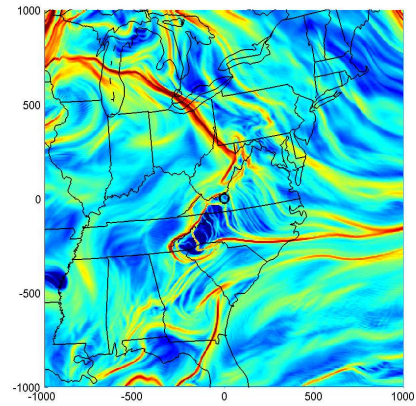
(b) 15:00 1 May 2007
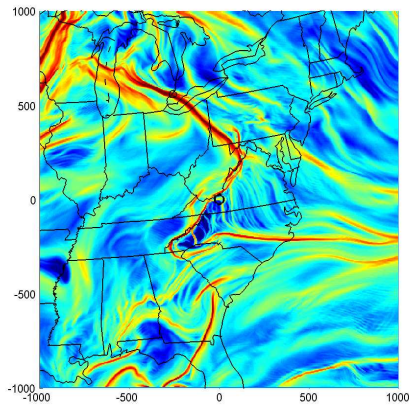
(c) 18:00 1 May 2007
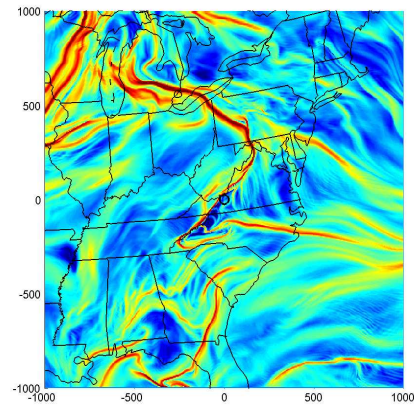
(d) 21:00 1 May 2007

Figure 8.9: Backward time FTLE field. Red indicates regions of high contraction and blue indicates regions of low contraction in forward time.

We track three sets of air that pass Kentland farm at approximately the same time as the sampling times and see that the LCS act as invariant transport barriers as shown in figure 8.10 and 8.11. The figures show the repelling LCS in red and the attracting LCS in blue. The black set is sampled at 15:00 on 30 April, the green set is sampled at 15:00 on 1 May 2007 and the grey set is sampled at 18:00 on 1 May 2007. The green set is laden with *Fusarium* while the black and grey sets have only a small concentration of spores.
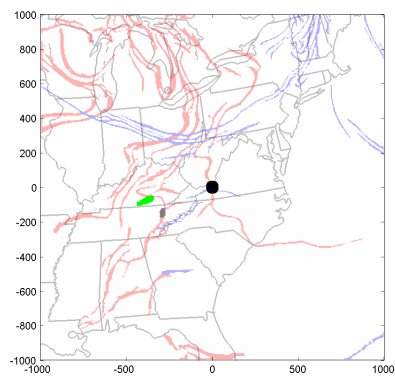
(a) 15:00 30 April 2007
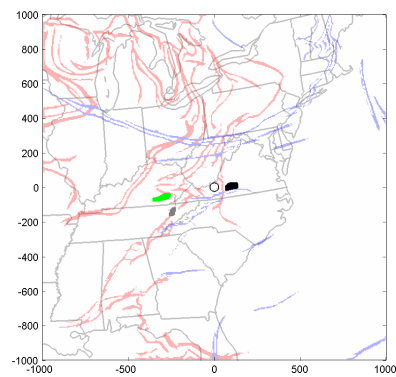
(b) 18:00 30 April 2007
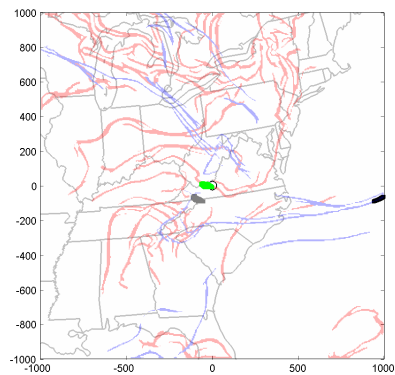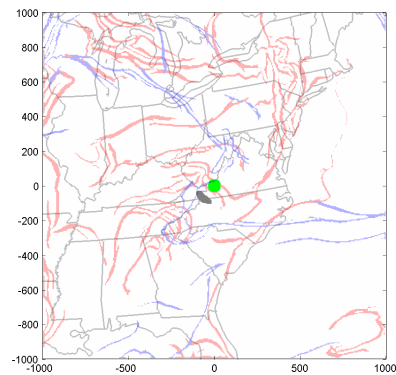
(c) 12:00 1 May 2007

(d) 15:00 1 May 2007

Figure 8.10: Motion of three sample sets.

The action of the attracting LCS is clearly seen again in 8.11(c) and (d) where the green and grey sets are stretched along the attracting LCS.

(a) 18:00 1 May 2007

(b) 21:00 1 May 2007

(c) 00:00 2 May 2007

(d) 03:00 2 May 2007
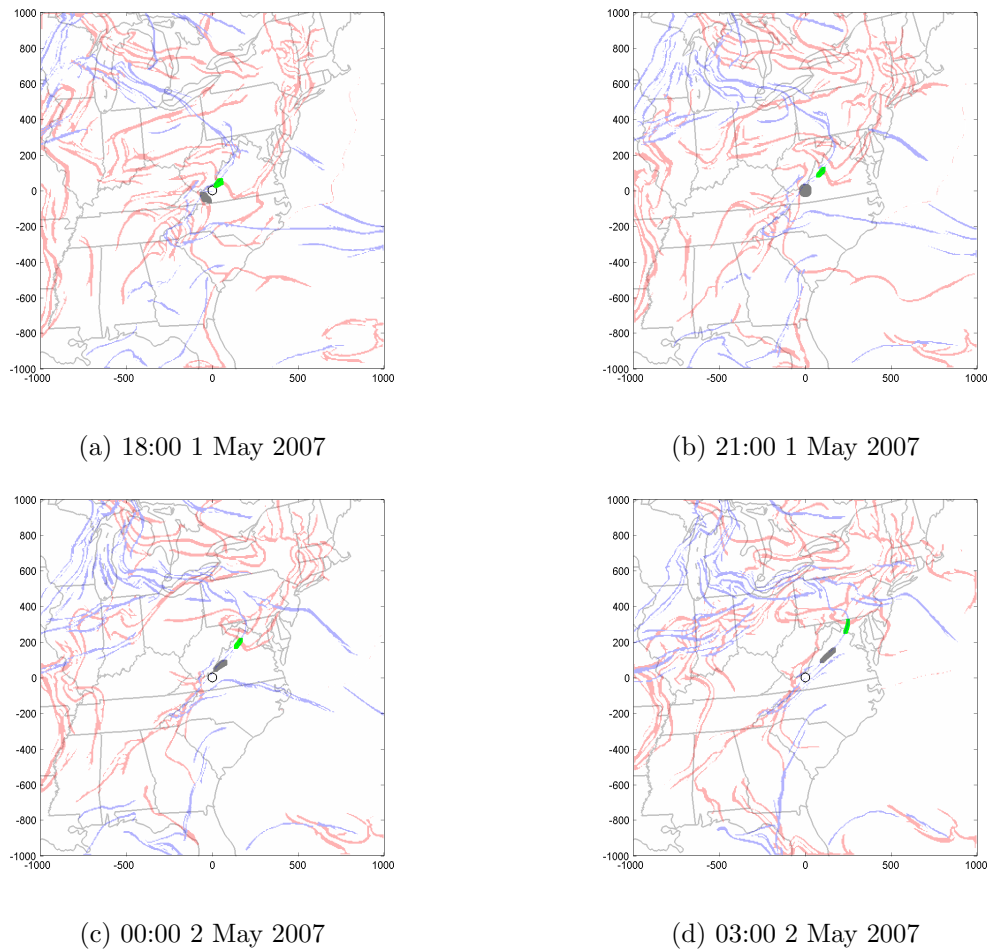
Figure 8.11: Motion of three sample sets.

8.3.2 Vertical rigidity - Comparison of FTLE field on different isobars

All the FTLE computations so far have been on a 900 mb isobaric surface. The computations will become physically irrelevant if the flow, despite being isobaric, varies significantly on closely spaced pressure surfaces. We present numerical results that clearly show that the FTLE computations are insensitive to small finite changes in the initial pressure. This is also a validation of the assumption of vertical rigidity. We compute the forward time FTLE field on a 875 mb pressure surface and on an 925 mb pressure surface for an integration time
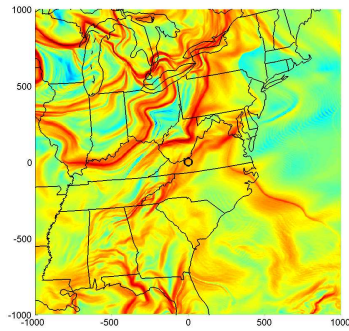
(a) 00:00 1 May 2007, 875 mb
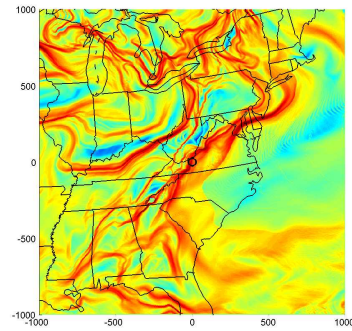
(b) 00:00 1 May 2007, 925 mb
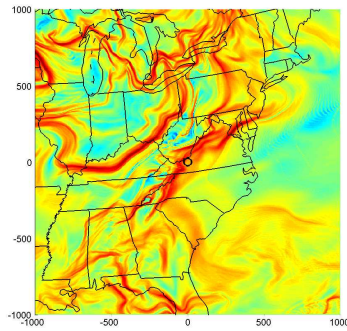
(c) 00:00 1 May 2007, 900 mb

Figure 8.12: Vertical rigidity of the FTLE field.

of 24 hours for various initial times on 1st May 2007. Figure 8.12 shows that the FTLE is qualitatively the same on the 875 mb, 900 mb and 925 mb isobaric surfaces. The differences are indicative of the fact that the flow is not perfectly isobaric. As was pointed out in section 7.3 a parcel of air has a vertical velocity of about 0.03 Pa/s. On average the parcel of air can rise or fall by 26 mb in 24 hours, that is, reach an adjacent pressure level in the NAM data. As the FTLE field on closely spaced pressure levels is almost the same, we have confidence that we do not make a significant error in the computation of transport barriers by assuming an isobaric flow.

8.3.3 Hypothesis Testing

We compute the forward and backward LCS on a 900 mb pressure surface for all the samples that are spaced within 24 hours of another sample. We test the hypothesis **H₁** separately for repelling and attracting LCS. Thus we have two hypotheses to test.

Hypothesis 8.3.1. H₁₁ *Every punctuated change in the atmospheric concentration of Fusarium is caused by the movement of a repelling LCS over the sampling point, between the two sampling times.*

Hypothesis 8.3.2. H₁₂ *Every punctuated change in the atmospheric concentration of Fusarium is caused by the movement of an attracting LCS over the sampling point, between the two sampling times.*

The null hypotheses for each of the two hypotheses is that the movement of the repelling (attracting) LCS is uncorrelated to the punctuated changes in the spore concentration.

The contingency tables for **H₁₁** and **H₁₂** are shown below.

Table 8.1: Contingency table for hypothesis **H₁₁**.

	Punctuated change has occured (ΔC_p)	
Repelling LCS passed over Kentland farm (L)	Yes	No
Yes	15	24
No	1	34

The correlation between the repelling LCS and punctuated changes using equation (6.3) is

$$\phi_{11} = 0.4318. \tag{8.2}$$

The sensitivity of the test is 0.9375 and the specificity of the test is 0.5862. From this we can infer that **almost every punctuated change can be identified by the movement of**

Table 8.2: Contingency table for hypothesis $\mathbf{H_{12}}$.

Attracting LCS passed over Kentland farm (L)	Punctuated change has occured (ΔC_p)	
	Yes	No
Yes	6	10
No	10	48

a repelling LCS. The correlation ϕ_{11} is however not close to 1, because the test has a low specificity, i.e many repelling LCS cross the sampling point without causing any punctuated changes.

The correlation between the attracting LCS and punctuated changes using equation (6.3) is

$$\phi_{12} = 0.2026. \tag{8.3}$$

The sensitivity of the test is 0.3750 and the specificity is 0.8275. The low sensitivity means that punctuated changes occur without the passage of attracting LCS over the sampling point but the high specificity means that whenever an attracting LCS does pass the sampling point, the chance of a punctuated change occurring is high.

We can combine both the hypotheses into a single hypothesis $\mathbf{H_1}$ as in section 6.2.2 for which the contingency table is given in table 8.3. The correlation for hypothesis $\mathbf{H_1}$ is

Table 8.3: Contingency table for hypothesis $\mathbf{H_1}$.

Attracting or Repelling LCS passed over Kentland farm (L)	Punctuated change has occured (ΔC_p)	
	Yes	No
Yes	15	28
No	1	30

$\phi = 0.3794$ with a sensitivity of 0.9365 and specificity of 0.5172. The low correlation of the attracting LCS as well as its low sensitivity to punctuated changes means that it is not a

reliable diagnostic tool to study punctuated changes. Even though correlation of the repelling LCS to punctuated changes is also not very high to be claimed to be statistically significant, the sensitivity of the hypothesis $\mathbf{H_{11}}$ is very high. A quick inspection of the data shows that the low correlation of the repelling LCS to punctuated changes in spore concentration is because of the high number of false positives n_4.

To summarize the results of the hypothesis testing, punctuated changes in the spore concentrations are due to the movement of a repelling LCS, though the movement of every repelling LCS does not cause a punctuated change. There are two reasons for this, (1) the chaotic nature of atmospheric flow ensure that many trajectories have a high local repulsion and (2) we did not discriminate between repelling ridges of high and low magnitude above a threshold. It is possible that punctuated changes can depend on the FTLE value of the repelling LCS, which we have not accounted for in this thesis. On the other hand the movement of attracting LCS usually causes a punctuated change though every punctuated change is not caused by the movement of an attracting LCS. It must be noted that the punctuated changes in spore concentration that we studied are the ones due to long distance transport and not due to local emission by infected plants, whose correlation, if any, to the movement of transport barriers is not investigated here.

8.4   Contribution to literature

In this chapter we have outlined a geometric framework of atmospheric transport barriers that determine punctuated changes in the concentration of a tracer in the atmosphere. We identified these transport barriers with attracting and repelling LCS that can be obtained from trajectory computation using meteorological data in an equation-free manner. Analyzing the FTLE field for the days that the aerial samples were collected on, we found that punctuated changes in spore concentrations can be governed by the movement of repelling LCS. While the concept of transport barriers and in particular those identified by LCS have

been applied in earlier works to study transport in the upper atmosphere [40] and lobe dynamics in hurricanes [76], our work is the first instance of the application of LCS to study meso-scale transport and punctuated changes of a measured tracer in the lower atmosphere.

Chapter 9

Set oriented methods and LCS

In chapter 2 we reviewed both the geometric approach of stretching and the probabilistic approach to dynamical systems using finite-time Lyapunov exponents and the Perron-Frobenius operator. The method of FTLE and LCS has found applications in time-dependent systems especially time-dependent fluid flows in the last decade. Also in the last decade, a different approach has been taken to study mixing and barriers in flows, using the probabilistic approach to identify so called 'almost invariant sets' in a flow, optimally selected sets that do not mix significantly with the rest of the phase space domain. This approach has been advanced in the works of Dellnitz [16] and Froyland [23]. This has raised the question of how the almost invariant sets are related to FTLE, [25]. The recent application of this approach to study mixing in a lid driven cavity flow in [68] and [29] has further generated interest in this question. In this chapter we will present some numerical results of comparison between the AIS approach and LCS approach. Once we identify the qualitative relationship we apply this to obtain a new method of computing LCS which will also have a probabilistic interpretation.

9.1 Review of almost invariant sets

We define an invariant set, using the notation we used of the flow map and σ-algebra of the (domain) set X outlined in chapter 2.

Definition 9.1.1. *A subset $B \subset X$ is said to be invariant, if $\phi_{t_0}^t(B) \subset B$ for all time t. For discrete flow maps $S : X \mapsto X$, a set $B \subset X$ is invariant if $S^n(B) \subset B$ for all n, where $S^n = S \circ S \circ ...S$ (n times), where $\circ$ denotes function composition.*

If the flow map or the discrete map are non invertible, then the definition is true only for $t \geq 0$ and $n \geq 0$. Usually one is interested in a subset B that is maximally or properly invariant, i.e. an invariant set B that does not contain a proper subset that is invariant. Maximal invariance implies $B = \phi_{t_0}^t(B)$. We first redefine an invariant set in terms of the Perron-Frobenius operator.

Definition 9.1.2. *The characteristic function of a set B is defined by $\mathcal{X}_B(x) = 1$ if $x \in B$ and $\mathcal{X}_B(x) = 0$ is $x \notin B$.*

Definition 9.1.3. *Let $(X, \mathcal{B}, \mu)$ be a measure space and $\phi_{t_0}^t : X \mapsto X$ be a nonsingular transformation. A measure ν is said to be invariant under the flow $\phi_{t_0}^t : X \mapsto X$ if $\nu(\phi^{-1})(B) = \nu(B)$ for every $B \in \mathcal{B}$.*

If B is a properly invariant set then define the measure $\nu(A) = \int_X \mathcal{X}_B \mu(A)$ for any $A \in \mathcal{B}$. Then the measure ν is invariant.

Theorem 9.1.1. *Let $(X, \mathcal{B}, \mu)$ be a measure space and $\phi_{t_0}^t : X \mapsto X$ be a nonsingular transformation. Let P be the Perron-Frobenius operator associated with ϕ. Consider a probability density function $f \in L^1$. Then a probability measure ν given by $\nu(B) = \int_B f d\mu$ is invariant if and only if f is a fixed point of P [38].*

The proof follows from a direct application of the Radon-Nikodym theorem and can be found in [38]. Taking $f = \frac{1}{\mu(B)} \mathcal{X}_B$, a uniform probability density function on the set B, then

since $f = Pf$, we get $Pf = \frac{1}{\mu(B)}\mathcal{X}_B$ from which the invariance of B follows. It is easily seen that if an invariant measure exists, then the maximum eigenvalue of P is 1 [28], [16], [38].

The examples that we study in this chapter are flows on $\mathbb{R}^2$. In practice the domain is discretized into a finite number of boxes, say $\{B_1, B_2, ..., B_n\}$, the probability density function is approximated as a sum of simple functions on the discretized domain $f = \sum_{i=1}^{N} c_i\mathcal{X}_{B_i}$ and the Perron-Frobenius operator P becomes a matrix (linear operator) between finite dimensional vector spaces, called a stochastic transition matrix. The entries of the matrix P are determined by a Monte-Carlo simulation [16] and [23]. Each box in the domain contains a fixed a number of points (initial conditions), which are integrated from a time t_0 to t. The final position of the points gives the matrix P as -

$$P_{ij} = \frac{\mu(B_i \cup \phi^{-1}(B_j))}{\mu(B_i)} \tag{9.1}$$

The theorems from Markov chains that are used to prove this in [16] and [23]require a time reversible a operator P. This is achieved by creating a reversible Markov operator P_r given by

$$P_r = \frac{P + \overline{P}}{2} \tag{9.2}$$

where $\overline{P}$ is the time reversed analogue of P. Its elements are given by

$$\overline{P} = \frac{u_j P_{ji}}{u_i} \tag{9.3}$$

where u_j and u_i are components of the first left eigenvector of P. For a conservative flow in which the domain is uniformly discretized, $\overline{P} = P^*$, the transpose of P.

9.1.1 Partitioning the domain into two almost invariant sets

Now we are interested in sets that are not perfectly invariant under the flow, but almost so; i.e., we allow a subset of non-zero measure to leak out.

Definition 9.1.4. *A set $B \in \mathcal{B}$ is said to be almost invariant if*

$$\rho_\mu(B) = \frac{\mu(B \cup \phi^{-1}(B))}{\mu(B)} \approx 1 \tag{9.4}$$

Intuitively $P_r f \approx f$ or $P_r f = \lambda f$ giving rise to an eigenvalue problem. The first (maximum) eigenvalue is still 1 and the eigenvector is the invariant measure, which makes the whole domain as the largest invariant set. It was shown in [16] [23] that the left eigenvector corresponding to the second eigenvalue gives the 'second most' almost invariant set, the invariance being higher if the second eigenvalue of P is closer to 1. For computational reasons we will make use of the singular vectors of P_r instead of the eigenvectors as was done in [22]. This is because the singular value decomposition is well conditioned and less sensitive to small changes in the matrix P_r introduced due to the discretization. It should be noted that P_r is self adjoint since $P_r = 0.5(P + P^*) = P_r^*$. From the spectral theorem, [53], [37], the SVD of P_r is unique. The SVD of P_r is

$$P_r = U\Sigma V^* = P_r^* = V\Sigma U^* \tag{9.5}$$

which gives $U = V$. Next P_r is a normal matrix, i.e., $P_r^* P_r = P_r P_r^*$. So again from the spectral theorem P_r has a unitary eigen-decomposition and and the left eigenvectors of P_r are given by

$$P_r = Y^*\Lambda Y \tag{9.6}$$

with $Y^* = Y^{-1}$ From the equations (9.6) and (9.5) we get $U = Y$, i.e. the left singular vectors and left eigenvectors of P_r are the same.

The problem of partitioning the phase space domain X into a given number of sets between which transport is minimal is a difficult one [16]. But partitioning the domain into two almost invariant sets is an easier problem. First we note that the singular vectors V^* form an orthonormal basis for P_r. The first singular vector V_1^*, associated with the singular value 1, is the stationary distribution and is positive. Since $V_2^* \perp V_1^*$ we can infer that V_2^* has

both positive and negative parts. From the definition of a Markov operator the $P_r(V_2^*)^+ > 0$ and $P_r(V_2^*)^- < 0$. So the sets on which the positive and negative parts of the second singular vector V_2^* are supported are almost invariant sets and partition the domain X into two parts.

9.1.2 Stretching and the Perron-Frobenius operator

Our motivation here is to examine the relationship between the almost invariant sets and the FTLE field defined by stretching. A theorem in [38] relates the deformation gradient $\frac{d\phi}{dx}$ with the Perron-Frobenius operator.

Theorem 9.1.2. *Let $(X, \mathcal{B}, \mu)$ be a measure space and $\phi_{t_0}^t : X \mapsto X$ be a nonsingular transformation and $f : X \mapsto \mathbb{R}$ a probability density function. Then for every $B \in \mathcal{B}$,*

$$\int_{\phi^{-1}(B)} f(\phi(x))d\mu = \int_B f J^{-1}(x)d\mu$$

where J is the determinant of the deformation tensor $J = \frac{d\phi}{dx}$ and $J^{-1} = \frac{d\phi^{-1}}{dx}$. The proof is obtained by change of variables and is given in [38]. Applying the Radon-Nikodym theorem one obtains $Pf(x) = f(\phi^{-1}(x))J^{-1}(x)$. So if $J = 1$ we get $Pf = f$, making f an invariant probability density function. The Cauchy Green tensor is obtained from the deformation tensor $\frac{d\phi}{dx}$. The square root of the eigenvalues of C are the eigenvalues of $\frac{d\phi}{dx}$. However we cannot directly use this relation between stretching and the Perron-Frobenius operator to relate almost invariant sets and LCS in a flow. This is because theorem 9.1.2 uses only the determinant of the deformation tensor and not the individual eigenvalues. If the flow preserves the Lebesgue measure, such as in Hamiltonian systema $J = 1$ everywhere despite the existence of expansion and contraction in the domain of the flow.

9.2 Coherent sets and stretching in time dependent flows

We seek to measure the stretching and deformation of a set without relying on computing the stretching of line elements as was done by the FTLE method in chapter 3. Instead we develop the analogy between the Radon-Nikodym theorem and the Perron-Frobenius operator with the evolution of a physical mass or blob in a two-dimensional Euclidean setting and arrive at a heuristic measure of stretching and FTLE. We discuss some issues with extending the method of almost invariant set (AIS) to time dependent flows and the issues with the computation of FTLE and its application to finding sets that do not mix significantly with other sets which have motivated the work in the rest of the chapter.

We define coherent sets and mixing in general time-dependent flows in a physically intuitive manner. We define a δ-interior set of B by $B_\delta = \{x : N_\delta(x) \subset B\}$ where $N_\delta(x)$ denotes the neighborhood of radius δ around x, i.e. all points of B that are at least a distance of δ from the boundary of B. If the size of this δ interior does not decrease under the action of the flow then the set has not mixed with the rest of the domain and it is coherent. More precisely $\frac{\mu(\phi(B_\delta))}{\mu(B_\delta)} \approx 1$. In figure 9.1 sets B_1 and B_2 are advected by a flow ϕ. Set B_1 is coherent since $\mu(B_{1\delta}) \approx \mu(\phi(B_{1\delta}))$ while B_2 is not coherent since $\mu(B_{2\delta}) >> \mu(\phi(B_{2\delta}))$. Mixing has
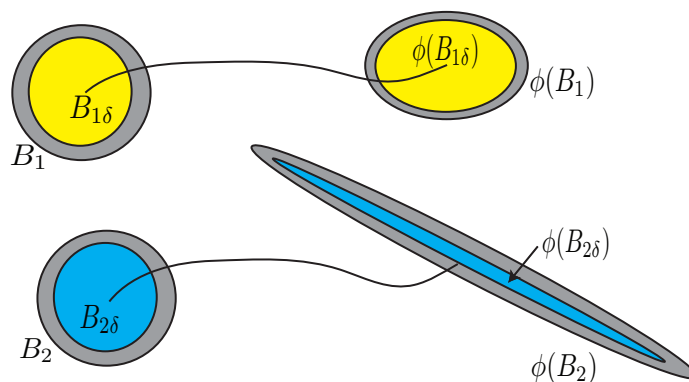
Figure 9.1: Concept of coherent sets in time dependent flows. B_1 is coherent and B_2 is not.

traditionally been considered to be produced due to stretching and folding of sets and this has often been quantified using entropy measures that relied on computing the stretching of line elements. Stretching and folding decrease the ratio $\frac{\mu(\phi(B_\delta))}{\mu(B_\delta)}$. The definition of coherent sets here is based on this intuition.

9.3 Issues with the methods of AIS and FTLE in time dependent flows

We observe that f is a probability density function and Pf is the evolution of the probability density function under the action of the flow. If f is supported on a subset B, then the set is almost invariant if $Pf \approx f$. This method has a physical meaning in terms of mixing; the almost invariant sets do not mix significantly with the rest of the domain. But this method of identifying almost invariant sets cannot be extended to time dependent flows, or to even flows that are almost periodic without first knowing what the approximate time period is. The problem is illustrated in figure 9.2. Sets B_1 and B_2 in figure 9.2 advected by the flow
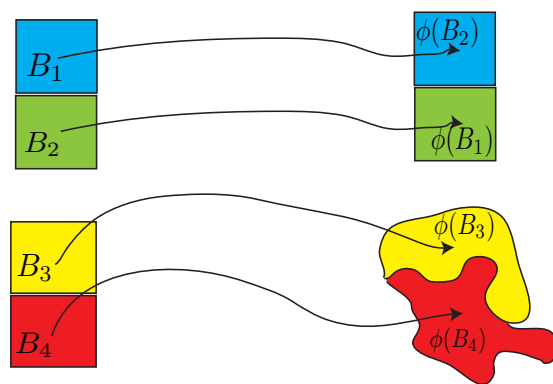
Figure 9.2: None of the sets B_1, B_2, B_3 and B_4 are almost invariant.

$\phi_{t_0}^t$ do not distort and mix with each other or the rest of the domain. However there is no 'overlap' between $\phi(B_1)$ and $\phi(B_2)$ and B_1 and B_2 respectively because the flow 'translates' them. So the sets B_1 and B_2 cannot be identified by the second eigenvalue-eigenvector of P.

Sets B_3 and B_4 clearly have distorted and mixed partially with each other and the rest of the domain.

It becomes even more difficult to extend the definition of almost invariant sets to flows in which the domain is 'leaky'. An example is the atmospheric flow where the meteorological data is well defined over North America, but very coarsely defined over the rest of the globe. Particles that exit the domain of the data are either lost or have to tracked using very coarse data. For a leaky domain the first eigenvalue of P is not 1 and the criteria of the second eigenvalue being close to 1 can become problematic.

The method of FTLE has the drawback that it uses the linearized flow equation (3.1) rewritten here,

$$\delta \mathbf{x}(t_0 + t) = \phi_{t_0}^t(\mathbf{x}) - \phi_{t_0}^t(\mathbf{x} + \delta \mathbf{x}) = \frac{d\phi_{t_0}^t}{d\mathbf{x}} \delta \mathbf{x}(t_0) + O(\|\delta \mathbf{x}^2(t_0)\|).$$

The evolution time $T = t - t_0$ has been selected in a subjective fashion depending on the problem. However this time has to be such that the second order terms $O(\|\delta \mathbf{x}^2(t_0)\|)$ do not grow to be too large. Usually this is accomplished by selecting a very small $\delta \mathbf{x}$ and either by keeping the time of evolution T small as we did in this thesis or rescaling the perturbation as it grows very large. To compute LCS at n points uniformly spaced in the domain, we evolve a grid of n initial points. For the method of rescaling we need $2n$ perturbed trajectories for each of the n reference trajectories. This quickly becomes computationally expensive as we increase n.

Another issue with the method of LCS is that it often identifies too much structure in the flow. One may not be interested in the small spatial scale repelling and attracting structures in the flow. In complex flows like the atmosphere almost every trajectory can have small localized expansion around it, but there could exist a collection of sets that has not stretched significantly. To the best of our knowledge there is no definition or method to identify such sets from the FTLE field.

9.4 Computation of FTLE using the covariance of probability density functions

We developed a novel method to compute the FTLE that will not use the linearized equations of the flow, or the stretching of individual line elements. The method of computing FTLE using the SVD of the Cauchy-Green tensor essentially computes the deformation of a neighborhood under the action of the flow $\phi_{t_0}^t$ as shown in figure 9.3. The FTLE for the
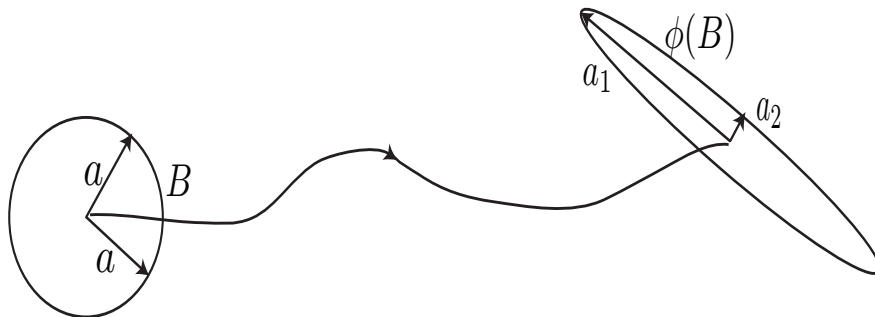
Figure 9.3: Deformation of a blob under the flow

reference trajectory in this case is $\sigma = \frac{1}{T} \log \left(\frac{a_1}{a} \right)$ where T is the time of evolution of the trajectory. For simplicity we assume the flow is in $\mathbb{R}^2$. We can treat the evolution of the set B as the evolution of two random variables X_1 and X_2 defined by a probability density function $f(x_1, x_2)$ which is initially $f = \frac{1}{\mu(B)} \mathcal{X}_B$, i.e., a uniform probability density over the set B and zero every where else. The covariance matrix of f is defined by $I_{ij} = E[(X_i - X_{im})(X_j - X_{jm})]$ where X_{1m} and X_{2m} are mean values of the random variables X_1 and X_2 and $E[\cdot]$ denotes the expectation $E[X_i] = \int x_i f$. Under the action of the flow ϕ, f is mapped to Pf where P is the associated Perron-Frobenius operator.

Definition 9.4.1. *Let I_0 be the covariance matrix of f and I the covariance matrix of Pf and let $\lambda_{max}(I)$ denote the maximum principal moment of inertia of I. Then the FTLE denoted by σ_I is defined by -*

$$\sigma_I = \frac{1}{T} \log \left(\frac{\lambda_{max}(I)}{\lambda_{max}(I_0)} \right) \tag{9.7}$$

We note that the covariance matrix is the same as the area moment of inertia for the set B and measures the deformation or distortion of the set. The definition of σ_I avoids the linearization of the flow and the measurement of the stretching of line elements which can be computationally expensive. Further it is a set-oriented method and directly computes the deformation of a set instead of inferring it from the deformation of line elements.

A probability density function f is almost invariant under the flow $\phi_{t_0}^t$ if $Pf \approx f$. This difference has been measured by the second eigenvalue and eigenvector of P. Another way to view the difference is in terms of stretching measured by second moments of the probability density functions. In figure 9.4, the set B_1 is not stretched significantly and remains almost invariant while the set B_2 is stretched and is not invariant. The inequality of f and Pf is captured by the second moments or the covariance matrix of f and Pf. We use this
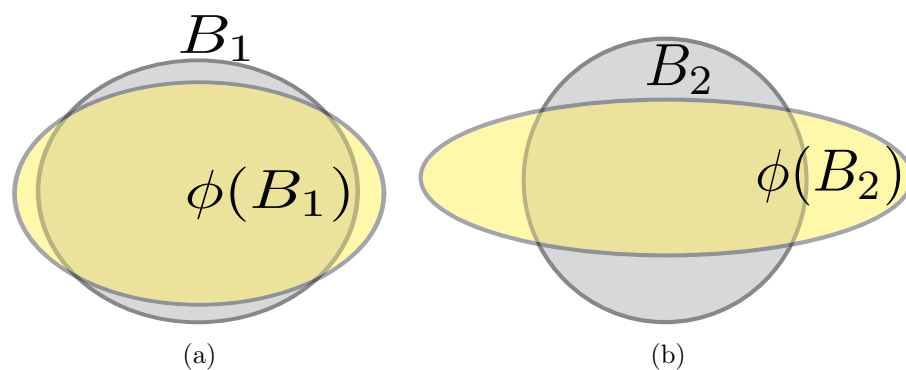
Figure 9.4: Stretching and almost invariant sets - set B_1 is almost invariant while the set B_2 is not.

relationship between stretching defined by the covariance matrix and almost invariance to extend the definition of almost invariant sets to time dependent flows.

Definition 9.4.2. *A probability density function f supported on a set B is almost coherent if Pf supported on $\phi(B)$ has almost the same covariance as f. Then B is almost coherent.*

This definition of coherence captures the essential feature of a coherent set - it does not mix or spread significantly in the domain. This definition also can identify non-mixing translating sets of the type shown in figure 9.2. Computationally we divide the domain

into boxes with a fixed number of initial points. The covariance matrix is calculated for each box about the mean of each of the boxes. While the covariance based definition of coherent sets can be applied to time-dependent flows, it suffers from the drawback of the covariance being non linear in the variables X_i. Thus one cannot pose the problem of finding an optimal combination of the boxes that will minimize the covariance as an eigenvalue problem. Compared to the standard method of computing the FTLE, by line stretching, this method does not rely on a linearized flow and hence one can use larger box sizes or integration times to heuristically find coherent sets. We see the covariance based method as a bridge between the geometric approach of measuring line stretching and the probabilistic approach of almost invariant sets.

9.5   Examples

We apply the method of almost invariant sets, the method of the FTLE described in chapter 3 and the method of computing the FTLE described in the previous section to three examples. The first two are periodic flows and the third is the atmospheric flow on a 900 mb isobaric surface.

9.5.1   Lid driven cavity flow

The first example we consider is the lid driven cavity flow in which mixing has been recently studied by the method of almost invariant sets in [29] and [68]. The model has been extensively studied in [11] and is considered here as the first example because of its physically simple piecewise steady velocity field. The flow is described by the stream function

$$\psi(x, y) = \sum_{n=1}^{2} U_n C_n f_n(y) \sin\left(\frac{n\pi x}{a}\right) \tag{9.8}$$

defined on the domain $[0, a] \times [-b, b]$ for time $0 \geq t \geq \tau_f/2$. where

$$f_n = \frac{2\pi y}{a} \cosh\left(\frac{n\pi b}{a}\right) \sinh\left(\frac{n\pi y}{a}\right)$$

and

$$C_n = \frac{a^2}{2n\pi^2 b} \left[\frac{a}{2n\pi b} \sinh\left(\frac{2n\pi b}{a}\right) + 1\right]^{-1}$$

For time $\tau_f/2 \geq t \geq \tau_f$, the sign of the velocity term U_1 is changed. This reflects the streamlines about $x = a$ every after a time $\tau_f/2$. The streamlines of the flow are shown in figure [fignum].

Using specific symmetry arguments given in [11], a specific ratio of the magnitudes of the terms U_2/U_1 along with a fixed value of the period of the flow τ_f is found such that it generates three period-3 fixed points in the domain $[0, a] \times [-b, b]$. The specific values of the constants that we borrowed from [11] are $U_1 = -1$ and $U_2 = 0.841298$ and $\tau_f^*/2 \approx 4.740202$ for the domain $[0, a] \times [-b, b] = [0, 6] \times [-1, 1]$.

A perturbation of the time period of the flow from the critical value of $\tau_f^*/2 \approx 4.740202$ destroys the fixed points. The method of almost invariant sets was used in [29] and [68] to study mixing for different values of the perturbed time period. Since our main interest here is to compare the method of AIS and LCS, we have chosen a single case, a specific value of half time period $\tau_f/2 = 4.848$ for our study.

We divided the domain into 4800 boxes each box containing a 100 points and found the time reversible Perron-Frobenius matrix P_r, by integrating a total of 480,000 initial points for a period equal to τ_f. Figure 9.5 contains 120×40 boxes which are the discretized finite approximation of the infinite dimensional space of Lebesgue integrable functions. Each box is a basis vector for the finite dimensional vector space. The second singular value is 0.99255639 and the second left singular vector U_2 of P_r is shown in figure 9.5, .

The sign of the eigenvector is positive in roughly half the domain and negative in the other half. By the property of the Markov operators 2.3.3, the positive and negative
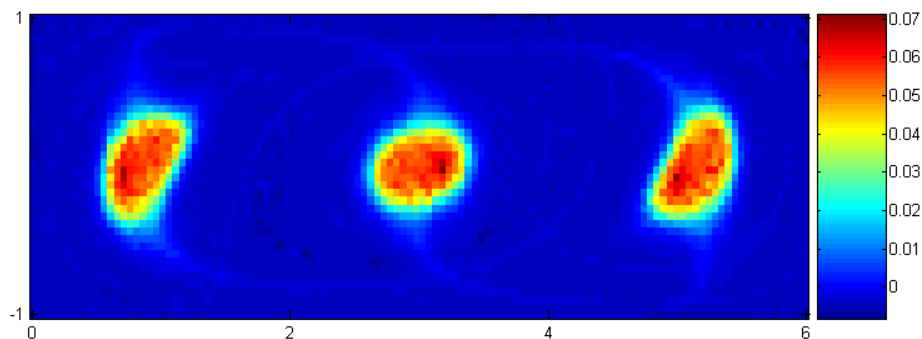
Figure 9.5: Second eigenvector u_2.

eigenvectors are invariant under the action of the Perron-Frobenius operator. Therefore the zero contour in the figure 9.7 forms the boundary of the almost invariant sets as shown in figure 9.6.
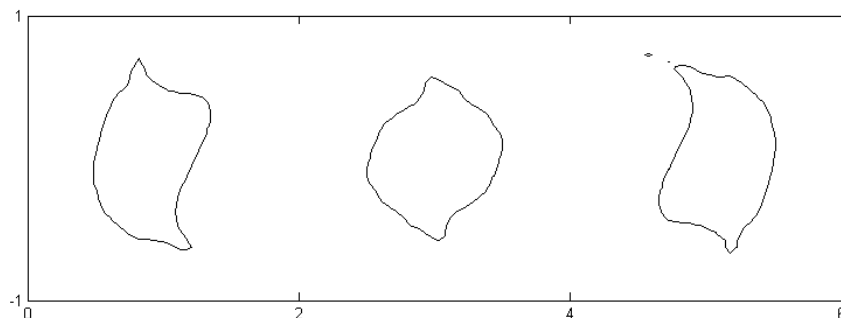
Figure 9.6: Zero contour of the second eigenvector showing the boundary of the almost invariant set.

We performed the FTLE computation for the same system for different integration times that are multiples of the period τ_f, the results of which are shown in figure 9.7.

The third method we used was the computation of the LCS and coherent sets using the covariance based method. For this we used the same discretization of 4800 boxes, with each box containing a 100 points, as was done in the case of the AIS approach. The results of this are shown in figure 9.8.

(a) $T = \tau_f$

(b) $T = 2\tau_f$

(c) $T = 3\tau_f$

(d) $T = 4\tau_f$

(e) $T = 5\tau_f$
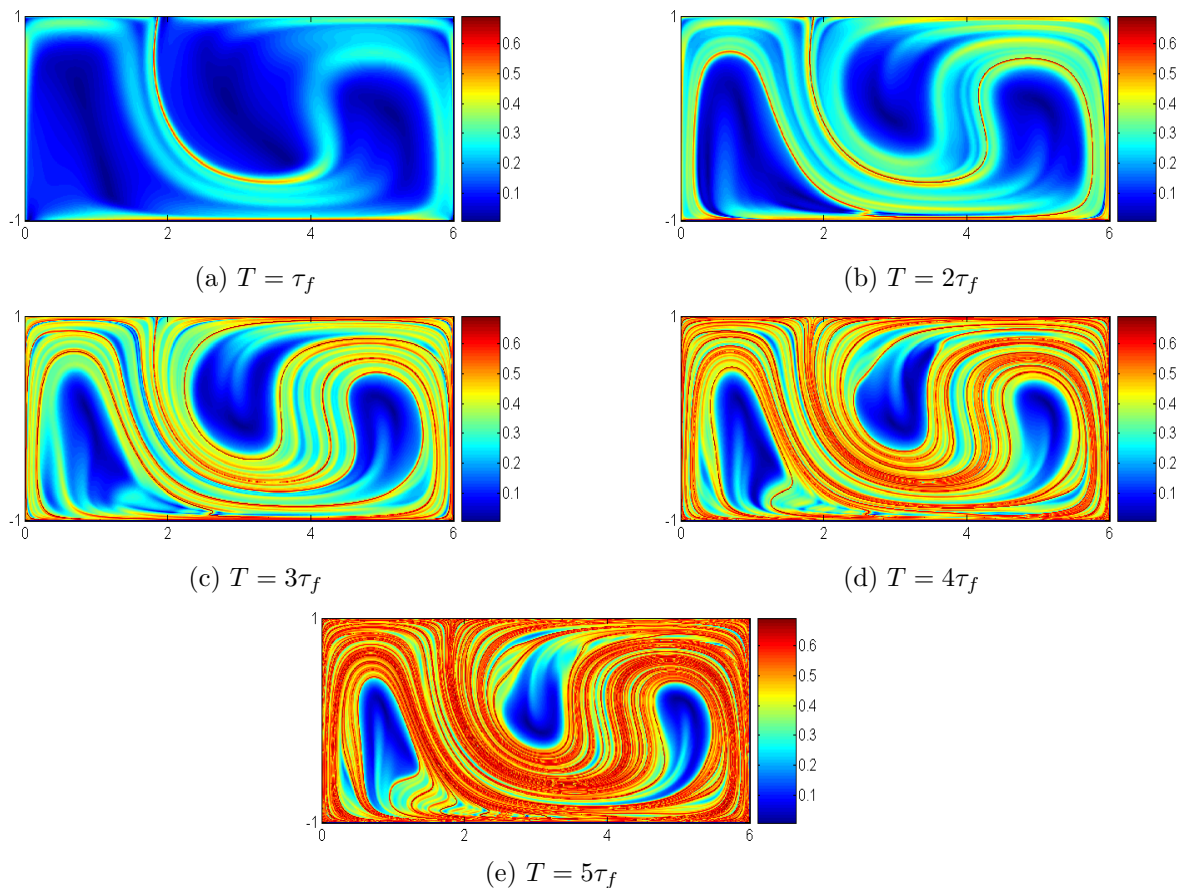
Figure 9.7: FTLE for integration time T for the lid driven cavity flow.

Comparing the results in figures 9.7 and 9.8 we find that the covariance approach of computing the FTLE agrees with the standard approach of computing the FTLE, using line stretching. This agreement is in the structure of the FTLE field only and not in the exact values of the FTLEs. As expected the FTLE computed from the covariance approach is higher. Comparing the FTLE obtained from either of the two methods with the AIS in figure 9.5, it is immediately obvious that an arbitrary threshold can be set in the FTLE field to partition the domain into sets that stretch less and those that stretch more, as shown in figure 9.9. Even after setting an arbitrary threshold, the sets of low stretching do not match very well with the AIS shown in figure 9.6.

However one needs to be careful with the comparison of the almost invariant sets

(a) $T = \tau_f$

(b) $T = 2\tau_f$

(c) $T = 3\tau_f$

(d) $T = 4\tau_f$

(e) $T = 5\tau_f$
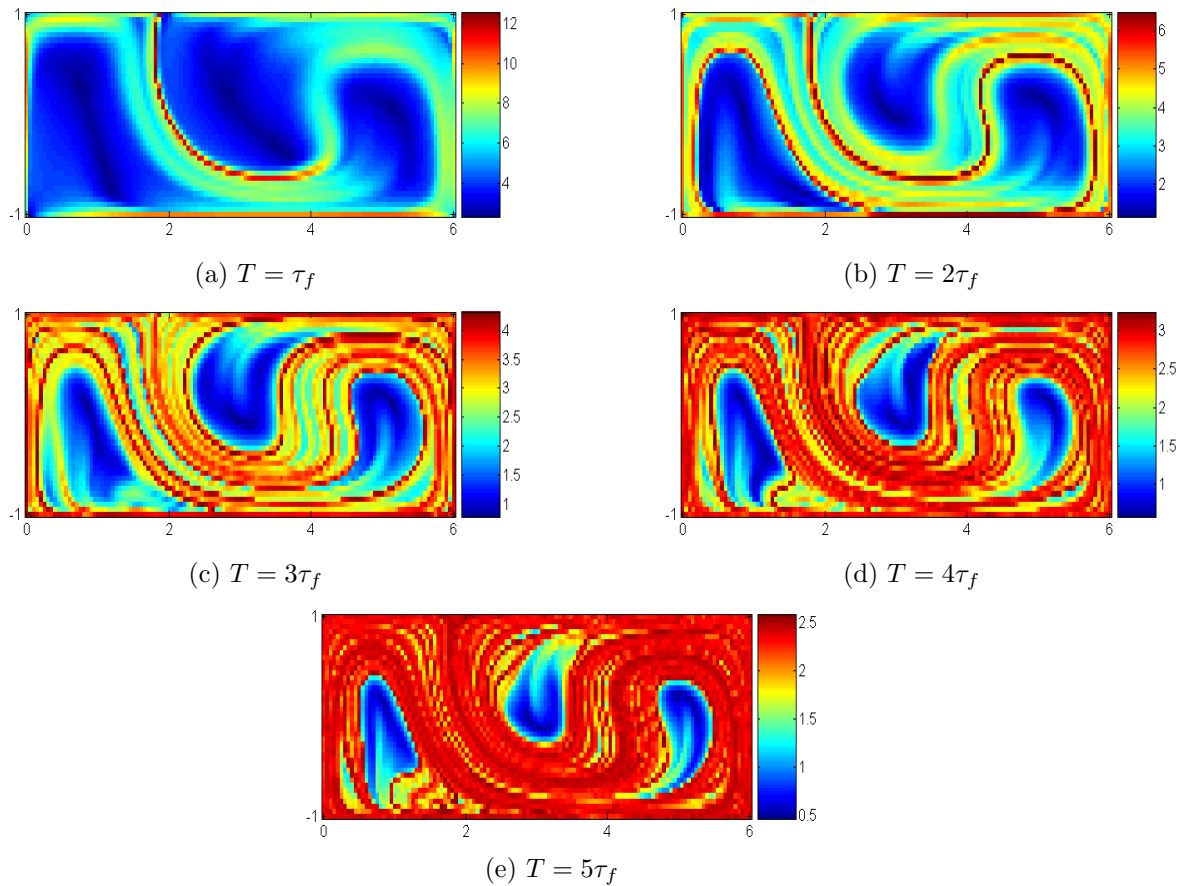
Figure 9.8: The covariance based FTLE for integration time T for the lid driven cavity flow.

(a) $FTLE < 0.2$

(b) Covariance based $FTLE < 1.2$
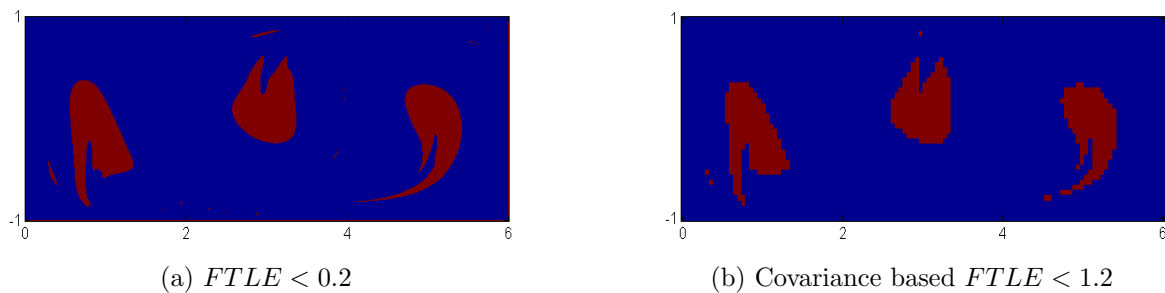
Figure 9.9: Almost invariant sets obtained by setting a threshold for the FTLE obtained by the method of (a) line stretching and (b) covariance.

with the FTLE field, because of the interpretation of invariance. We computed the first 6 singular values and vectors of the discretized Perron-Frobenius operator. The values are

$\lambda_2 = 0.99255639$, $\lambda_3 = 0.98292780$, $\lambda_4 = 0.9516905$, $\lambda_5 = 0.9473769$ and $\lambda_6 = 0.94344106$, with the corresponding singular vectors u_3 to u_6 shown in figure 9.10.

(a) u_3, $\lambda_3 = 0.98292780$

(b) u_4, $\lambda_4 = 0.9516905$

(c) u_5, $\lambda_5 = 0.9473769$

(d) u_6, $\lambda_6 = 0.94344106$
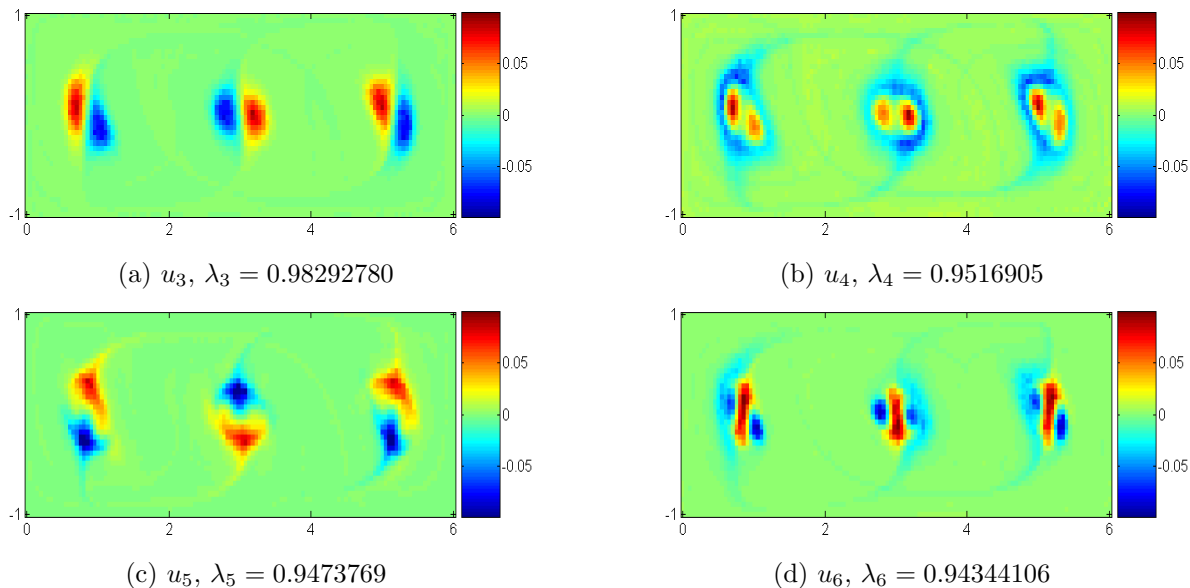
Figure 9.10: Higher eigenvectors u_3 to u_6.

The eigenvalues measure the invariance of a set, and since they are close to each other in magnitude, one can obtain other almost invariant sets that are slightly less invariant than those obtained from the second eigenvector. Linear combinations of the eigenvectors can produce a family of almost invariant sets that can be hard to distinguish from each other. The zero contours of the eigenvectors u_2 to u_6 are shown in figure 9.11. Let u_n^+ and u_n^- denote the nonnegative and negative parts of nth eigenvector, i.e., $u_n = u_n^+ - u_n^-$. Consider the vector $f = u_2^+ + u_3^+ + u_4^- + u_5^+ + u_6^+$. Then f is non negative over the domain and from the properties of the Markov operator 2.3.3, $Pf > 0$. Then the support of f is almost invariant.

From figure 9.11, it is seen that the support of u_4 contains the support of u_2, u_3, u_5 and u_6 and hence the support of f is at least $\lambda_4 = 0.9516905$ invariant. We can only conjecture that the ridges of the FTLE field capture a particular linear combination of the eigenvectors of P.
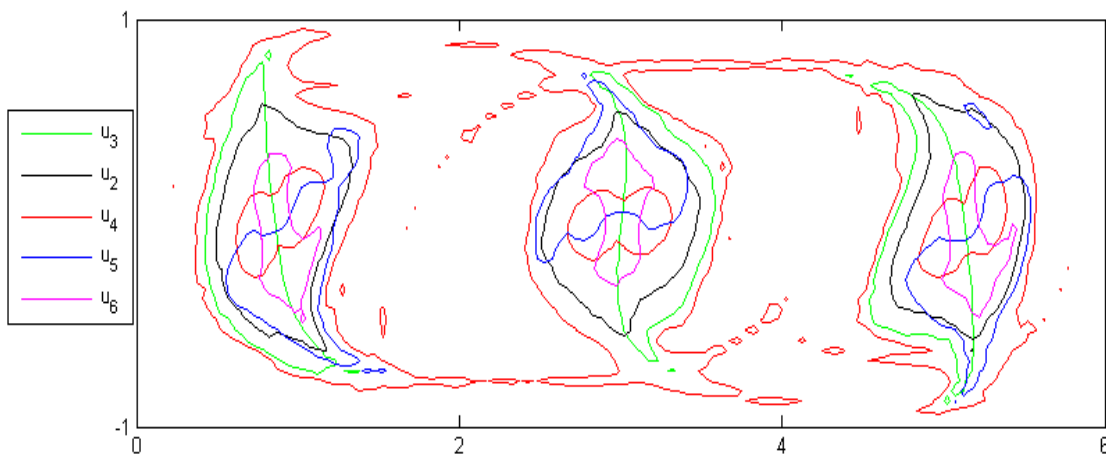
Figure 9.11: Zero contours of eigenvectors u_2 to u_6.

9.5.2 Double gyre flow

The lid driven cavity flow in the previous section is not only piecewise smooth, but piecewise time independent. We return to the example of the double gyre flow which is time dependent but periodic, to apply the method of AIS and compare it with the FTLE field. The double gyre flow is defined by the stream function $\psi(x, y, t) = A \sin(\pi f(x, t)) \sin(\pi y)$, with the variables A, f, a, b and ω defined as in section 3.2.2. The parameter values chosen are $A = 0.25$, $\omega = 2\pi$ and $\epsilon = 0.25$. The time period of the flow is $\tau = 1$. We chose these particular parameter values to compare our results with [25] in which the same values were chosen for computing the almost invariant sets. The FTLE fields obtained for an integration period $T = 10$, using the methods of line stretching and the covariance are shown in figure 9.12. The FTLE field using the line stretching method was computed using a grid of points initially spaced uniformly at a distance of 0.001. For the covariance based method we discretized the domain into 80000 square boxes of size 0.005 each containing 625 points. Using the same discretization for the Perron-Frobenius operator P of the flow, we found the eigenvalues of P to be $\lambda_2 = 0.99974084$ $\lambda_3 = 0.99954927$, $\lambda_4 = 0.99874607$, $\lambda_5 = 0.99811312$ and $\lambda_6 = 0.99714149$. The eigenvalues for this problem are very closely spaced and here we find
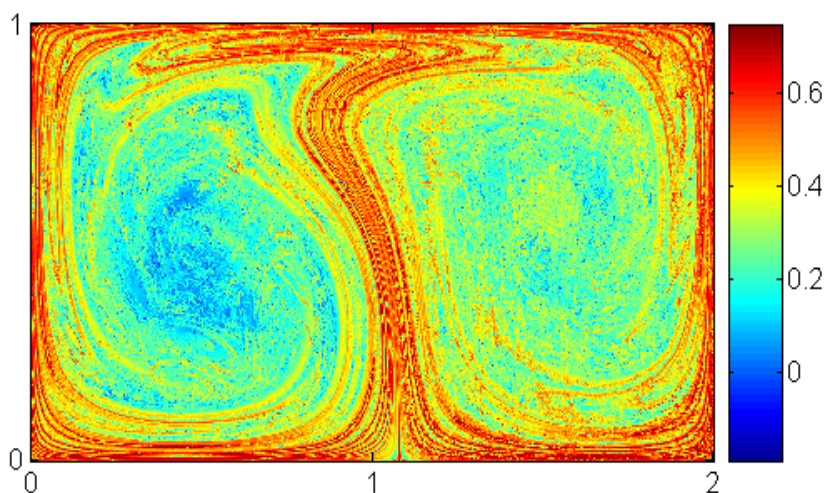
(a)FTLE obtained from line stretching.
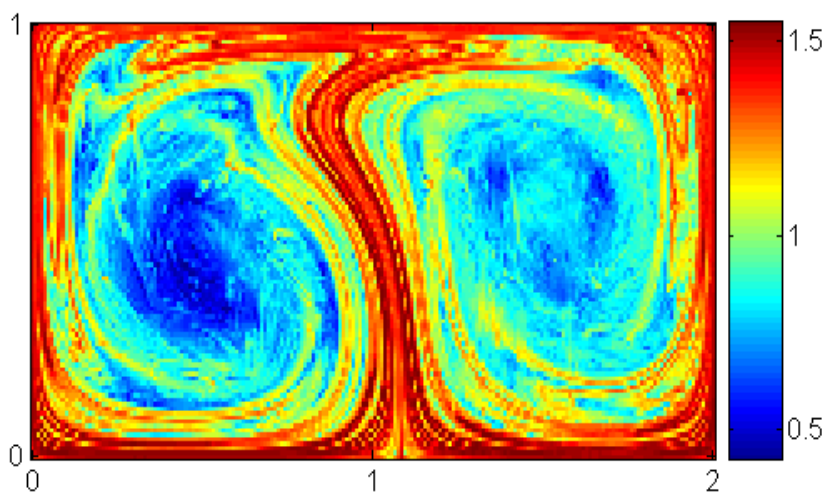
(b)FTLE field obtained from covariance method

Figure 9.12: FTLE field for the double gyre flow for an integration time of $T = 10$.

that the eigenvectors from u_2 to u_6 shown in figure 9.13 have a similar structure. It has been pointed out in [22] that in problems where there exists a cluster of eigenvalues close to 1, the computation of the eigenvectors are sensitive to the discretization of the domain. From the point of view of physical applications, the almost invariant sets obtained from any of the eigenvectors u_2 to u_6 are the same.

(a) u_2, $\lambda_3 = 0.99974084$

(a) u_3, $\lambda_3 = 0.99954927$

(b) u_4, $\lambda_4 = 0.99874607$

(c) u_5, $\lambda_5 = 0.99811312$

(d) u_6, $\lambda_6 = 0.99714149$
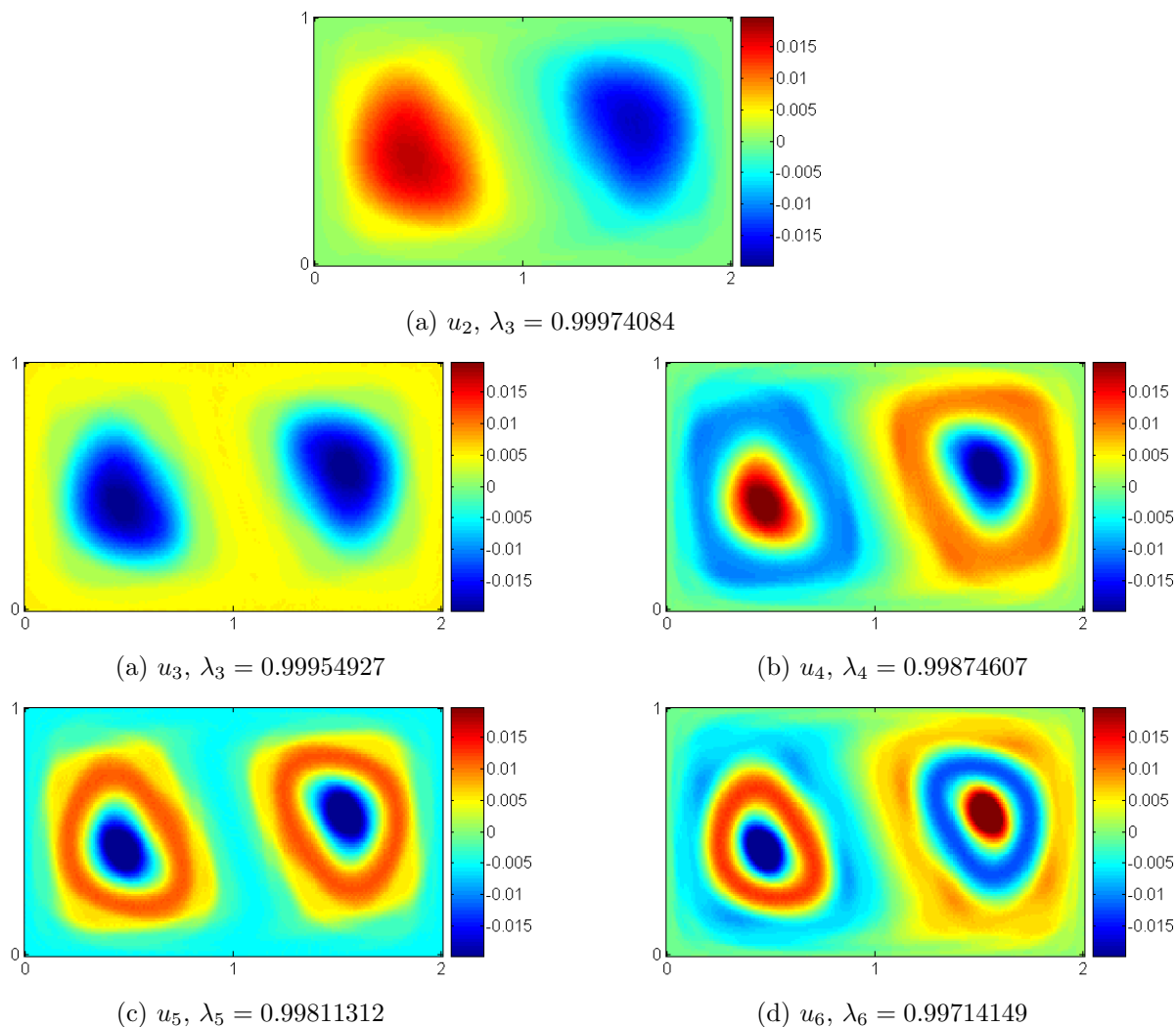
Figure 9.13: The eigenvectors, u_2 to u_6, of the Perron-Frobenius operator for the double gyre flow.

Comparing the almost invariant sets in figure 9.13 with the FTLE fields in figure 9.12 we can only infer that the regions of low stretching are approximately the same as the almost invariant sets given by the eigenvectors u_2 to u_6 and once again conjecture that a linear combination of the eigenvectors will produce an almost invariant set that can be identified by the regions of low stretching in the FTLE field.

9.5.3   Atmospheric flow

We now apply the covariance based method of computing the FTLE to the atmospheric flow, a time dependent aperiodic flow, defined by the meteorological velocity data. We took the velocity data for May 1st 2007 on a 900 mb pressure surface in a domain that is 1200 km × 1200 km centered around Kentland farm. We discretized the domain into 14400 square boxes each of size 10 km and containing 81 points spaced at intervals of 1 km. We integrated the 1.44 million points for a time period of 24 hours. The covariance based FTLE is shown in figures 9.14 and 9.15.

(a) 00 : 00

(b) 03 : 00

(c) 06 : 00

(d) 09 : 00
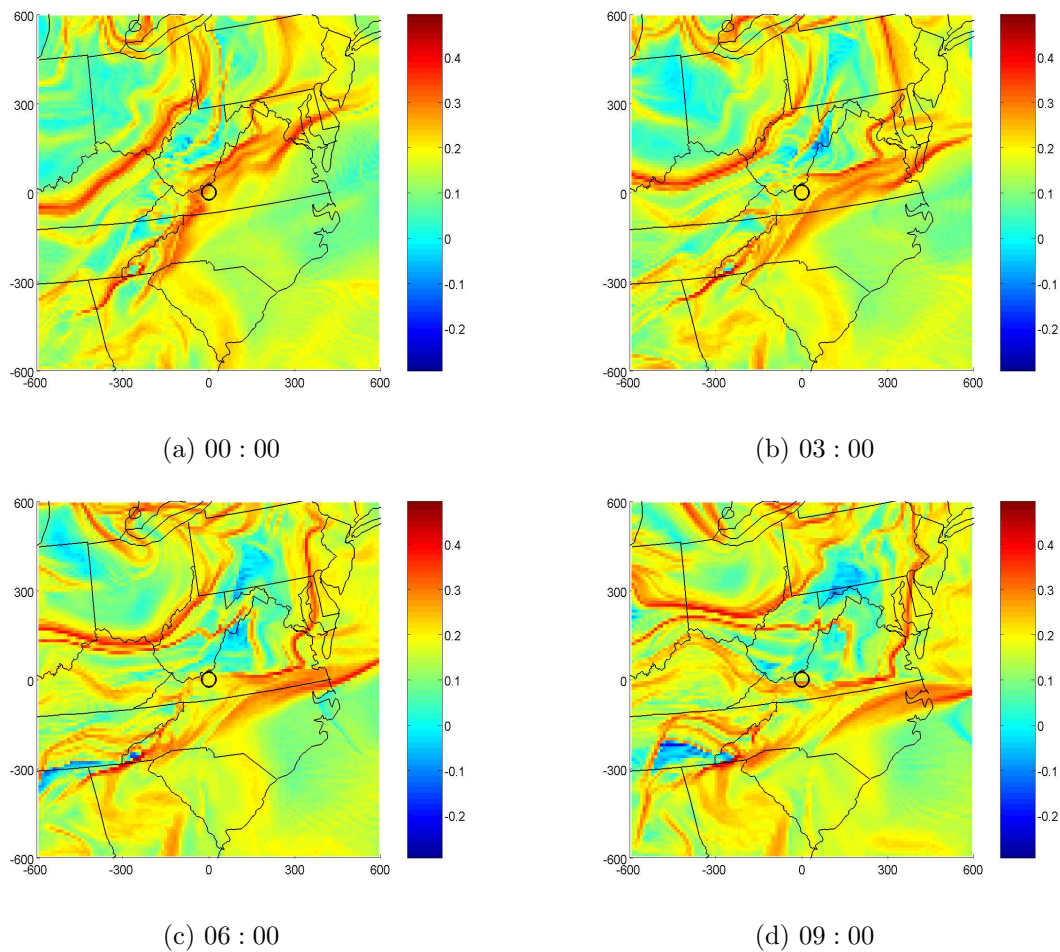
Figure 9.14: Covariance based FTLE field on 1st May 2007 for an integration time $T = 24$ hours for initial starting times (a) - (d).

(a) 12 : 00

(b) 15 : 00

(c) 18 : 00

(d) 21 : 00
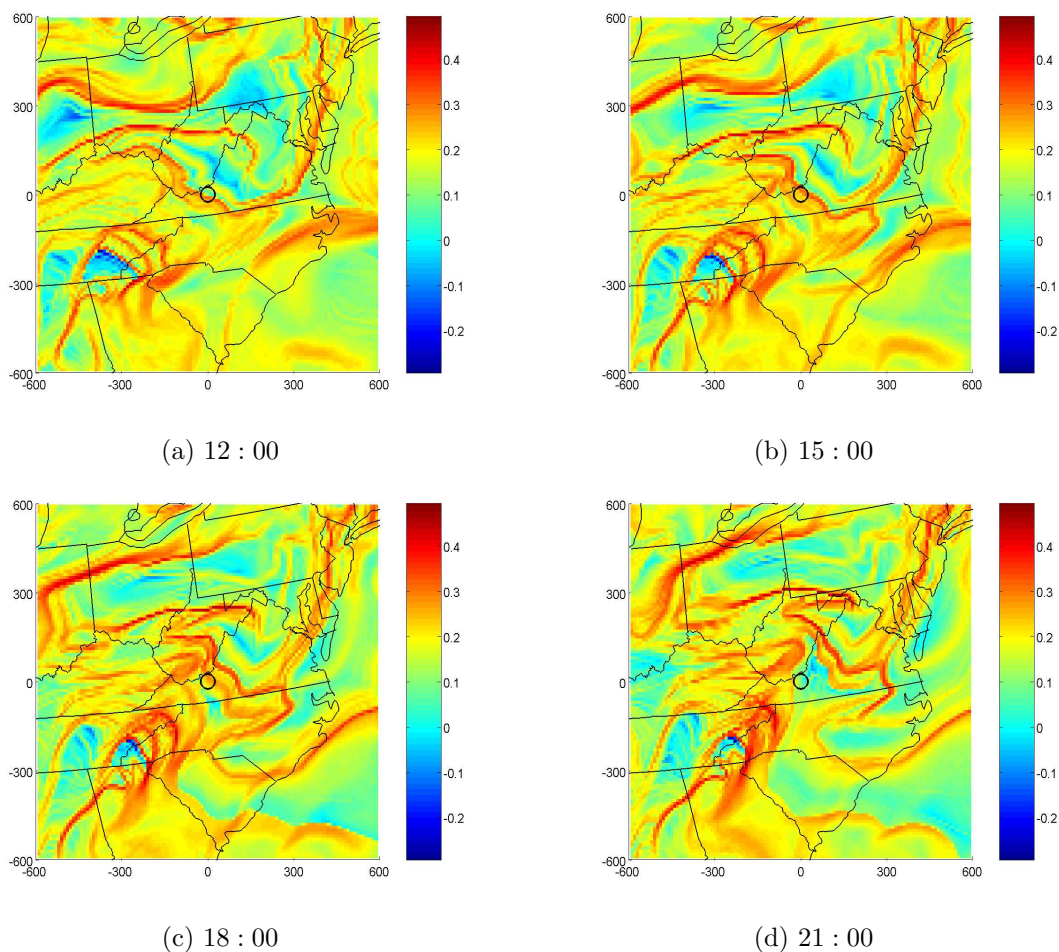
Figure 9.15: Covariance based FTLE field on 1st May 2007 for an integration time $T = 24$ hours for initial starting times (a) - (d).

Comparing with the FTLE field obtained from the line stretching method we see that the main ridges in the FTLE field are the same, but the covariance based FTLE does not have many small spatial scale ridges unlike in the FTLE field. The movement of the transport barrier over Kentland farm is clear from figure 9.14(f). We can obtain the coherent sets by setting a threshold (of 0.14/hr) on the covariance FTLE field as shown in figure 9.16. For a FTLE value of 0.14/hr, the covariance matrix of an initially square box of size 10 km would evolve to have a maximum radius of gyration of 27 km in 24 hours, approximately the radius of the 'sampling circle'.

(a) 15 : 00 30 April 2007

(b) 15 : 00 1 May 2007
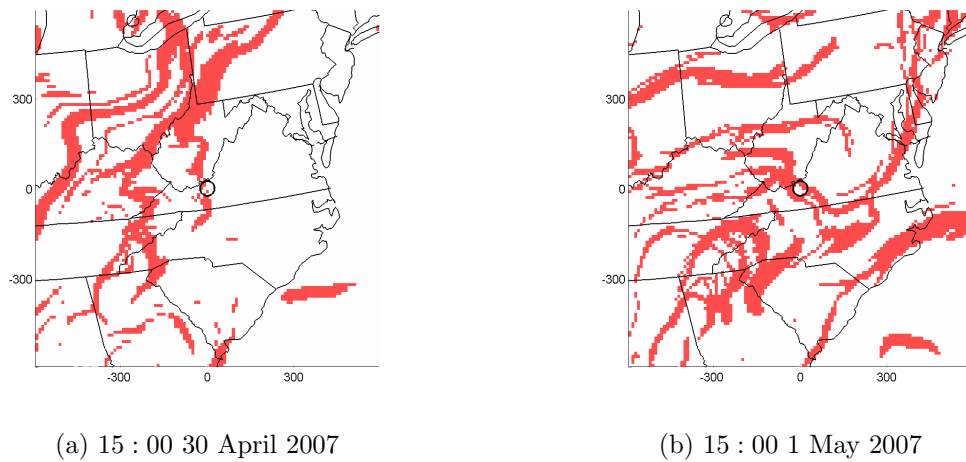
Figure 9.16: Coherent sets separated by regions of high FTLE (in red).

(a) 00 : 00

(b) 03 : 00
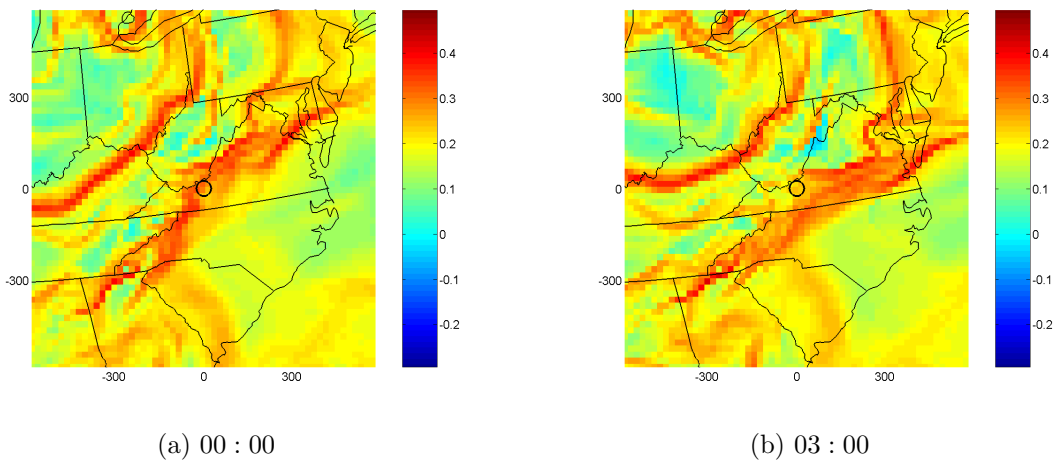
Figure 9.17: Covariance based FTLE field on 1st May 2007 for an integration time $T = 24$ hours for initial starting times (a) - (b) and box size of 20 km.

Since we do not rely on the tangent linearization, we can choose a larger box size. For example the covariance based FTLE field for a box size of 20 km is shown in figures 9.17 and 9.18.

(a) 06 : 00

(b) 09 : 00

(c) 12 : 00

(d) 15 : 00

(e) 18 : 00

(f) 21 : 00
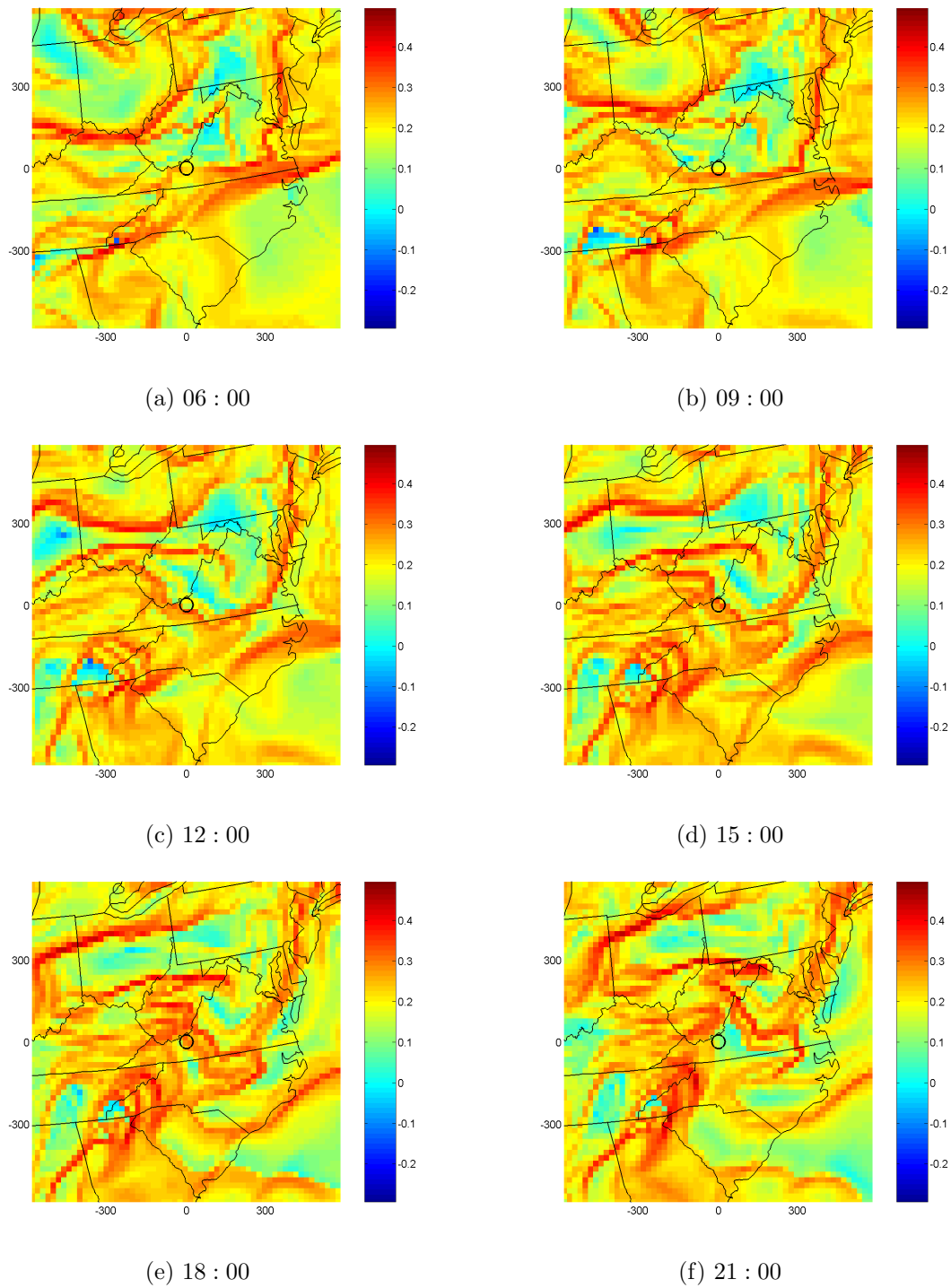
Figure 9.18: Covariance based FTLE field on 1st May 2007 for an integration time $T = 24$ hours for initial starting times (a) - (f) and box size of 20 km.

Comparing the FTLE field computed using the different box sizes, it can be seen that the main ridges can still be detected by increasing the box size. We consider this to be the main advantage of covariance based FTLE; we can choose the size of the sets of interest without the constraint of linearization.

9.6   Contribution to literature

In complex flows stretching and folding can be high making the tangent linearization invalid after a short integration period. The covariance based method of computing the FTLE is the first instance of finding finite-time Lyapunov exponents that does not use the linearized equations of a flow making it more general in scope of application. The covariance matrix can be geometrically interpreted as a measure of stretching in phase space as well as have a probabilistic interpretation. This bridges the gap between geometric and probabilistic methods of studying phase space transport.

Chapter 10

Conclusion

Until recently time-dependent (or aperiodic) systems have not been easy to study using the traditional tools of nonlinear dynamical systems, such as Poincare maps and method of invariant manifolds. The tangent linearization for time dependent systems has attracted extensive interest over many decades in the mathematics community which led to many new insights and results on Lyapunov and other spectra and generalized stable and unstable manifold theorem. However the restrictive nature of these results precluded their application to real world natural and engineering systems which cannot be characterized by smooth flows for infinite time. Starting in the 90's the easily applicable, equation free, computational method of LCS emerged in the works of Wiggins, Haller, Marsden, Lekien and Shadden. The work in this PhD thesis is a small step in the direction of extending and applying these methods to high dimensional and complex time dependent flows.

Our focus throughout the thesis has been on partitioning the phase space using codimension-one sets that act as barriers to transport. We exploited this framework of transport barriers in two problems. The first problem we applied this framework to was for the dynamics of inertial particles in a two dimensional fluid flow. We showed that the repelling LCS can be used to segregate particles with different Stokes number. The second problem we studied is the role of transport barriers in the motion of pathogen spores in the lower atmosphere.

We showed that a statistically significant relationship exists between punctuated changes in spore concentrations and the passage of the repelling LCS over the sampling point. We view this as a significant contribution to the problem of tracking the spread of plant pathogens in the atmosphere, one that can aid in the development of new dynamical systems based tools to study advective transport of tracers in the atmosphere.

We also investigated the theoretical considerations behind the computation of the FTLE. We defined the partial LCS and used it to identify transport barriers in the first problem on segregation of inertial particles. FTLE computations are often done for a small integration time period, to ensure the validity of the tangent linearization. This can be problematic since the structure of transport barriers can often emerge only for long integration times. To over come this we used the idea of quantifying the covariance of a probability density function or analogously the covariance of the support of the density function to define a FTLE that does not rely o linearization. We used the covriance based idea of stretching to make a heuristic connection between the geometric FTLE method and the probabilistic almost-invariant set method with two examples; the lid-driven wide cavity flow and the double-gyre flow. Using the FTLE we then defined coherent sets as the time-dependent analogs of almost-invariant sets and used the definition to identify large scale coherent sets in the lower atmosphere.

Some immediate future lines of research that can be followed from this thesis include

- Extension of the concept of atmospheric LCS to three dimensional transport barriers which will account for possible variations in transport due to three dimensional features of the flow that effect the trajectories of air masses for long integration periods. This will have to simultaneously account for the fact that the linearized equations will be not be valid for long integration periods.

- Integration of the computation of LCS into a near real-time forecast scheme to predict punctuated changes and spread of pathogens via the atmosphere.

- Development of possible control strategies that will use the LCS to manipulate the motion of inertial particles in Stokes flows.

- Development of a method to compute the FTLE using measure theoretic methods which exist for the computation of Lyapunov exponents for ergodic systems. This will enable the computation of a large finite time FTLE field using only a short time of integration and the global information of all the short time trajectories.

Bibliography

[1] E. R. Abraham. The generation of plankton patchiness by turbulent stirring. *Nature*, 391:577–580, 1998.

[2] A. Agresti. *Categorical Data Analysis*. John Wiley and Sons Inc, first edition, 1990.

[3] G. Ahlers. Experiments on spatio-temporal chaos. *Physical Review A*, 249:18–26, 1998.

[4] D. E. Aylor. A framework for examining inter-regional aerial transport of fungal spores. *Agricultural and Forest Meteorology*, 38:263–288, 2002.

[5] D. E. Aylor. Settling speed of corn (*Zea mays*) pollen. *Journal of Aerosol Science*, 33:1599–1605, 2003.

[6] D. E. Aylor. Spread of plant disease on a continental scale: Role of aerial dispersal of pathogens. *Ecology*, 84:1989–1997, 2003.

[7] D. E. Aylor, M. T. Boehm, and E. J. Shields. Quantifying aerial concentrations of maize pollen in the atmospheric surface layer using remote-piloted airplanes and lagrangian stochastic modeling. *Journal of Applied Meteorology and Climatology*, 45:1003–1015, 2006.

[8] D. E. Aylor and T. K. Flesch. Estimating spore release rates using a lagrangian stochastic simulation model. *Journal of Applied Meterorology*, 40:1196–1208, 2001.

[9] A. Babiano, J. H. E. Cartwright, O. Piro, and A. Provenzale. Dynamics of a small neutrally buoyant sphere in a fluid and targeting in hamiltonian systems. *Physical Review Letters*, 84:5764–5767, 2000.

[10] M. T. Boehm and D. E. Aylor. Lagrangian stochastic modeling of heavy particle transport in the convective boundary layer. *Atmospheric Environment*, 39:4841–4850, 2005.

[11] J. Chen. *Topological chaos and mixing in lid-drive cavities and rectangular channels.* PhD thesis, Virginia Polytechnic Institute and State University, 2008.

[12] C. Coulliette, F. Lekien, J. D. Paduan, G. Haller, and J. Marsden. Optimal pollution mitigation in monterey bay based on coastal radar data and nonlinear dynamics. *Environmental Science and Technology*, 41:6562–6572, 2007.

[13] B. Cushman-Roisin and J. M. Beckers. *Introduction to geophysical fluid dynamics.*

[14] J. A. Davis, D. W. Inglis, K. J. Morton, D. A. Lawrence, L. R. Huang, S. Y. Chou, J. C. Sturm, and R. H. Austin. Deterministic hydrodynamics : Taking blood apart. *Proceedings of National Academy of Sciences*, 103:14779–84, 2006.

[15] J. M. Davis. Modeling the long-range transport of plant pathogens in the atmosphere. *Annual review of phytopathology*, 25:169–188, 1987.

[16] M. Dellnitz and O. Junge. On the approximation of complicated dynamical behavior. *SIAM Journal on Numerical Analysis*, 36:491–515, 1998.

[17] D. DiCarlo, D. Irimia, R. G. Tompkins, and M. Toner. Continuous inertial focusing, ordering, and separation of particles in micro channels. *Proceedings of National Academy of Sciences*, 104(48):18892–18897, 2007.

[18] L. Dieci and E. S. Van Vleck. *Lyapunov and other spectra : a survey. Collected Lectures on the Preservation of Stability under Discretization.* SIAM, 2002.

[19] R. A. Duce, C. K. Unni, B. J. Ray, J. M. Prospero, and J. T. Merrill. Long-range atmospheric transport of soil dust from asia to the tropical north pacific: Temporal variability. *Science*, 209:1522–1524, 1980.

[20] D. Eeberly. *Ridges in Image and Data Analysis*. Kluwer Academic Publishers, second edition, 1996.

[21] M. C. Facchini, M. Mircea, S. Fuzzi, and R. J. Charlson. Cloud albedo enhancement by surface-active organic solutes in growing droplets. *Nature*, 401:257 – 259, 1999.

[22] D. Fritzsche and V. Mehrmann. An SVD approach to identifying metastable sets of markov chains. *Technical report from Institut fur Mathematik, Technishe Universitat Berlin*, 2006.

[23] G. Froyland and M. Dellnitz. Detecting and locating near optimal almost invariant sets and cycles. *SIAM Journal on Scientific Computing*, 24:1507–1523, 2009.

[24] G. Froyland, K. Judd, and A. I. Mees. Estimation of lyapunov exponents of dynamical systems using a spatial average. *Physical Review E*, 51:2844–2855, 1995.

[25] G. Froyland and K. Padberg. Almost-invariant sets and invariant manifolds - connecting probabilistic and geometric descriptions of coherent structures in flows. *Physica D*, 236 (16):1839–1863, 2003.

[26] E. S. Gawlik, J. E. Marsden, P. C. Du Toit, and S. Campagnola. Lagrangian coherent structures in the planar elliptic restricted three-body problem. *Celestial mechanics and dynamical astronomy*, 3:227–249, 2009.

[27] D. W. Griffin. Atmospheric movement of microorganisms in clouds of desert dust and implications for human health. *Clinical Microbiology Reviews*, 20(3):459–477, 2007.

[28] G. Grimmett and D. Stirzaker. *Probability and Random Processes*. Oxford University Press, third edition, 2001.

[29] P. Grover. *Finding and exploiting structure in complex systems via geometric and sta-tistical methods.* PhD thesis, Virginia Polytechnic Institute and State University, 2010.

[30] G. Haller. Lagrangian structures and the rate of strain in a partition of two-dimensional turbulence. *Physics of Fluids A*, 13:3368–3385, 2001.

[31] G. Haller and T. Sapsis. Instabilities in the dynamics of neutrally buoyant particles. *Physics of Fluids*, 20(017102), 2008.

[32] G. Haller and T. Sapsis. Where do inertial particles go in fluid flows? *Physica D*, 237:573–583, 2008.

[33] J. R. Holton. *An introduction to dynamic meteorology.* Elsevier Academic Press, fourth edition, 2004.

[34] L. R. Huang, C. E. Cox, R. H. Austin, and J. C. Sturm. Continuous particle separation using deterministic lateral displacement. *Science*, 304:987–990, 2004.

[35] K. Ide, D. Small, and S. Wiggins. Distinguished hyperbolic trajectories in time depen-dent fluid flows: Analytical and computational approach for velocity fields as data sets. *Nonlinear Processes in Geophysics*, 9:237–263, 2002.

[36] S. Isard and S. H. Gage. *Flow of Life in the Atmosphere: An Airscape Approach to Understanding Invasive Organisms.* Michigan State University Press, East Lansing, MI, first edition, 2001.

[37] E. Kreyszig. *Introductory Functional Analysis with Applications.* Wiley, first edition, 1989.

[38] A. Lasota and M. C. Mackey. *Chaos, Fractals and Noise. Stochastic Aspects of Dynam-ics.* Springer-Verlag, second edition, 1994.

[39] F. Lekien and J. Marsden. Tricubic interpolation in three dimensions. *International Journal for Numerical Methods in Engineering*, 63:455–471, 2005.

[40] F. Lekien and S. D. Ross. The computation of finite-time Lyapunov exponents on unstructured meshes and for non-euclidean manifolds. *Chaos: An Interdisciplinary Journal of Nonlinear Science*, 20:017505, 2000.

[41] F. Lekien, S. C. Shadden, and J. Marsden. Lagrangian coherent structures in n-dimensional systems. *Journal of Mathematical Physics*, 48:065404, 2007.

[42] Z. Li and G. Drazer. Separation of suspended particles by arrays of obstacles in microfluidic devices. *Physical Review Letters*, 98:050602, 2007.

[43] A. Majda. *Introduction to PDEs and waves for the atmosphere and ocean.* Courant Institute of Mathematical Sciences, New York University, New York, New York, first edition, 2003.

[44] S. L. Maldonado-Ramirez, D. G. Schmale, E. J. Shields, and G. C. Bergstrom. The relative abundance of viable spores of *Gibberella zeae* in the planetary boundary layer suggests the role of long- distance transport in regional epidemics of *Fusarium* head blight. *Agricultural and Forest Meteorology*, 132:20–27, 2005.

[45] M. R. Maxey and J. J. Riley. Equation of motion of a small rigid sphere in a nonuniform flow. *Physics of fluids*, 23:883–889, 1983.

[46] T. Nishikawa, Z. Toroczkai, and C. Grebogi. Advective coalescence in chaotic flows. *Physical Review Letters*, 87(3):038301, 2001.

[47] J. R. Parrington, W. H. Zoller, and N. K. Aras. Asian dust: Seasonal transport to the hawaiian islands. *Science*, 220:195–197, 1983.

[48] M. R. Paul, M. C. Cross, P. F. Fischer, and H. S. Greenside. Power-Law behavior of power spectra in low Prandtl number Rayleigh-Bénard convection. *Physical Review Letters*, 87(15):154501, 2001.

[49] M. R. Paul, M. I. Einarsson, M. C. Cross, and P. F. Fischer. Extensive chaos in Rayleigh-Bénard convection. *Physical Review E*, 75(4):045203, 2007.

[50] M. R. Paul and T. Himanshu. Private communication, 2010.

[51] Y. Pesin and L. Barreira. *Encyclopedia of Mathematics and its applications 115, Non uniform hyperbolicity.* Cambridge University Press, first edition, 2007.

[52] S. J. Piketh, R. J. Swap, W. Maenhaut, H. J. Annergarn, and P. Formenti. Chemical evidence of long-range atmospheric transport over southern Africa. *Journal of Geophysical Research*, 107:4817, 2002.

[53] M. Reed and B. Simon. *Functional Analysis, Volume 1.* Academic Press, revised second edition, 1981.

[54] C. A. Rogers and E. Levetin. Evidence of long-distance transport of mountain cedar pollen into tulsa, oklahoma. *International Journal of Biometeorology*, 42:65–72, 1998.

[55] H. Royden. *Real Analysis.* Prentice Hall, third edition, 1988.

[56] W. Rudin. *Real and Complex Analysis.* McGraw-Hill, third edition, 1986.

[57] D. G. Schmale. Private communications, 2009.

[58] D. G. Schmale. Unpublished observations, 2009.

[59] D. G. Schmale, Q. A. Arntsen, and G. C. Bergstrom. The forcible discharge distance of ascospores of *Gibberella zeae. Canadian Journal of Plant Pathology*, 27:376–382, 2005.

[60] D. G. Schmale and G. C. Bergstrom. Spore deposition of the ear rot pathogen, *Gibberella zeae*, inside corn canopies. *Canadian Journal of Plant Pathology*, 26:591–595, 2004.

[61] D. G. Schmale, B. R. Dingus, and C. Reinholtz. Development and application of an autonomous unmanned aerial vehicle for precise aerobiological sampling above agricultural fields. *Journal of Field Robotics*, 25:133–147, 2008.

[62] D. G. Schmale, T. Fetters, S. D. Ross, P. Tallapragada, and B. Dingus. Isolates of *Fusarium graminearum* collected 40 to 300 meters above ground level cause *Fusarium*

head blight ad produce trichothecene mycotoxins. *2010 Potomac Division of Meeting of the American Phytopathological Society*, 2010.

[63] D. G. Schmale, E. J. Shields, and G. C. Bergstrom. Night-time spore deposition of the *Fusarium* head blight pathogen, *Gibberella zeae*, in rotational wheat fields. *Canadian Journal of Plant Pathology*, 28:1–9, 2006.

[64] G. Segre and A. Silberberg. Radial particle displacements in poiseuille flow of suspensions. *Nature*, 189:209 – 210, 2007.

[65] S. C. Shadden, F. Lekien, and J. Marsden. Definition and properties of lagrangian coherent structures from finite-time lyapunov exponents in two-dimensional aperiodic flows. *Physica D*, 212:271–304, 2005.

[66] T. Shinbrot, M. M. Alvarez, J. M. Zalc, and F. J. Muzzio. Attraction of minute particles to invariant regions of volume preserving flows by transients. *Physical Review Letters*, 87:1207–1210, 2001.

[67] E. A. Shinn, D. W. Griffin, and D. B. Seba. Atmospheric transport of mold spores in clouds of desert dust. *Archives of Environmental Health*, 58(8):498–504, 2003.

[68] M. Stremler, S. D. Ross, P. Grover, and P. Kumar. Almost invariant sets as ghost rods for fluid stirring. *Preprint*, 2010.

[69] A. B. Strook, S. K. W. Dertinger, A. Ajdari, I. Mezic, H. A. Stone, and G. M. Whitesides. Chaotic mixer for microchannels. *Science*, 295:647–651, 2002.

[70] A. P. Sudarsan and V. M. Ugaz. Multivortex micromixing. *Proceedings of the National Academy of Sciences of the United States of America*, 103(19):7228–7233, 2006.

[71] P. Tallapragada and S. D. Ross. Particle segregation by Stokes number for small neutrally buoyant spheres in a fluid. *Physical Review E*, 78, 2008.

[72] A. D. Taylor. Conformal map transformations for meteorological modelers. *Computers and Geosciences*, 23:63 – 75, 1997.

[73] A. D. Taylor. Conformal map transformations for meterological modelers, 1997. `http://www.arl.noaa.gov/documents/reports/cmapf.pdf`.

[74] L. Techy, D. G. Schmale, and C. A. Woolsey. Coordinated aerobiological sampling of a plant pathogen in the lower atmosphere using two autonomous aerial vehicles. *Journal of Field Robotics*, 27:335–343, 2010.

[75] M. Tirumkudulu, A. Tripathi, and A. Acrivos. Particle segregation in mono disperse sheared suspensions. *Physics of Fluids*, 11:507–509, 1999.

[76] P. C. Du Toit. *Transport and separatrices in time dependent flows*. PhD thesis, California Institute of Technology, 2010.

[77] S. M. Ulam and Von Neumann. On combination of stochastic and deterministic processes : Preliminary report. *Bulletins of American Mathematical Society*, (53):1120, 1947.

[78] S. Wiggins. *Chaotic transport in dynamical systems, Interdisciplinary Applied Mathematics*. Springer, first edition, 1993.

[79] S. Wiggins. *Introduction to Applied Nonlinear Dynamical Systems and Chaos, Texts in Applied Mathematics*. Springer, second edition, 2003.

[80] A. Wolf, J. B. Swift, H. L. Swinney, and J. A. Vastano. Determining Lyapunov exponents from a time series. *Physica D*, 16:285–317, 1985.

[81] C. L. Wolfe and R. M. Samelson. An efficient method for recovering lyapunov vectors from singular vectors. *Tellus Seires A - Dynamic meteorology and oceanography*, 59:355–356, 2007.

[82] W. Zdunkowski and A. Bott. *Dynamics of the atmosphere, A course in theoretical meteorology.* Cambridge University Press, first edition, 2003.